

ELECTROSPINNING OF NANOFIBERS FOR FILTRATION MEDIA

By

HYOUNGJUN PARK

A DISSERTATION PRESENTED TO THE GRADUATE SCHOOL
OF THE UNIVERSITY OF FLORIDA IN PARTIAL FULFILLMENT
OF THE REQUIREMENTS FOR THE DEGREE OF
DOCTOR OF PHILOSOPHY

UNIVERSITY OF FLORIDA

2010

© 2010 Hyoungjun Park

To Jin

ACKNOWLEDGMENTS

I thank to Dr. Sigmund, my officemates, friends and family for the support.

TABLE OF CONTENTS

	<u>page</u>
ACKNOWLEDGMENTS.....	4
LIST OF TABLES.....	8
LIST OF FIGURES.....	9
LIST OF ABBREVIATIONS.....	13
ABSTRACT.....	16
CHAPTER	
1 INTRODUCTION.....	19
Ceramic Fibermats as Filtration Media.....	19
Objectives and Hypothesis.....	20
Approach to Hypothesis.....	21
2 BACKGROUND.....	24
Filtration.....	24
Sol-gel Chemistry of Ti alkoxide.....	26
Hydrolysis and Condensation.....	26
Acid and Base Catalysts.....	27
Electrospinning.....	28
Principle.....	28
Advantage of Electrospinning over Other Fiber Fabrication Methods for Filters.....	31
3 FABRICATION OF FIBERMATS.....	37
Electrospinning PAN and Filtration Test.....	37
Polyacrylonitrile.....	37
Polymer Solution Preparation and Electrospinning.....	37
Set-up for Filtration Test.....	38
TiO ₂	38
Property.....	38
Sol Preparation.....	39
Electrospinning and Heat Treatment.....	39
TiO ₂ -SiO ₂ from Aqueous Sol.....	40
Reasoning of Adopting Aqueous Sol.....	40
Sol Preparation.....	41
Electrospinning and Heat Treatment.....	41

4	EXPERIMENTAL METHODS	45
	Fiber Diameter	45
	Scanning Electron Microscopy	45
	Image Analysis	45
	Filtration Test	46
	Sol-gel Chemistry of Aqueous Sol	47
	Nuclear Magnetic Resonance	47
	Chemical Shift	49
	Sample Preparation.....	50
	Reproduction of Spectrum.....	51
	Microstructure	51
	X-ray Diffraction.....	51
	Principle	51
	Sample Preparation and Operation.....	53
	Transmission Electron Microscopy	53
	Principle	53
	Sample Preparation	54
5	RESULT AND DISCUSSION.....	58
	Fiber Diameter	58
	Results and Discussion	58
	Fiber Diameter and Coefficient of Variation	58
	Conclusion.....	63
	Filtration Test	64
	Results and Discussion	64
	Conclusion.....	65
	Chemistry of Aqueous Sol	66
	Results and Discussion	66
	Hydrolysis Reaction	66
	Condensation Reaction.....	69
	Conclusion.....	71
	Microstructure of Electrospun Ceramic Fibers	71
	Results and Discussion	71
	TiO ₂	71
	TiO ₂ -SiO ₂ from Aqueous Sol.....	74
	Conclusion.....	77
	Discussions.....	77
6	CONCLUSIONS AND FUTURE WORK	108
	Conclusions	108
	Future Work	110
	LIST OF REFERENCES	114

BIOGRAPHICAL SKETCH..... 12121

LIST OF TABLES

<u>Table</u>	<u>page</u>
2-1 Partial charge distribution within the Ti oxo-polymer shown in Figure 2-4 ¹⁸	33
4-1 Reference of the chemical shift for ¹³ C- and ¹ H-NMR.	55
5-1 Result of analysis on fiber diameter of PAN and TiO ₂	81
5-2 Result of analysis on fiber diameter of TiO ₂ -SiO ₂	81
5-3 Results of filtration tests ^{36, 51} . PAN (a)x(b) means (b) layers of PAN fibermat fabricated by (a)-minute deposition via electrospinning. If (b) is unspecified, it's a single layer sample.	81
5-4 Values of electronegativity of atomic species in GPTMS ⁵³	81
5-5 Integration of block A, B and C (Figure 5-21, Figure 5-22, Figure 5-23 and Figure 5-24).	82
5-6 Calculated [MeOH] and [H ₂ O] based on values in Table 5-5, and experimental errors of [MeOH]+[H ₂ O].	82
5-7 Time required for gelation of sol of [0.005N HNO ₃]:[GPTMS]:[metal alkoxide]=2:1:x before gelation or precipitation. Precipitated sols are indicated as (p).	82
5-8 Grain size of different TiO ₂ phases calculated by Scherrer's equation on spectra shown in Figure 5-32. N/A means that the peaks were too weak to be analyzed.	82

LIST OF FIGURES

<u>Figure</u>	<u>page</u>
2-1 Filtration mechanisms of particulates in the aerosol by a fiber, (A) interception, (B) impaction, (C) diffusion ¹⁰ . Reprinted by permission from Hinds, William C. 1999. Aerosol technology (Page 192, Figure 9. 5., Page 193, Figure 9. 6. Page 194, Figure 9. 7.). John Wiley and Sons, Inc., New York.	34
2-2 A) Hydrolysis, B) alcoxolation, C) oxolation of Ti alkoxide. R means the alkyl group.	35
2-3 Hydrolysis in (A) acidic condition and (B) basic condition	35
2-4 Different Ti sites in Ti oxo-polymers.	36
2-5 (A) Schematic set-up of electrospinning, (B) forces applied to the liquidic sol or solution at the syringe tip.	36
3-1 Chemical structure of polyacrylonitrile.....	42
3-2 Electrospun PAN fiber mat sandwiched by two ACF mats.....	42
3-3 Crystal structure of anatase phase of TiO ₂ ^{43, 46} . Gray spheres (or brighter spheres in the black/white print) are Ti atoms while red spheres (or darker spheres in the black/white print) are O atoms. Reprinted by permission from Pyrgiotakis, Georgios. 2006. Titania Carbon Nanotube Composites for Enhanced Photocatalysis (Page 7, Figure 2-1). University of Florida, FL.....	43
3-4 Preparation procedure of the aqueous sol.	44
4-1 Experimental set-up for the filtration test ³⁶ . Reprinted by permission from Zhang, Qi et al. 2010. Improvement in Nanofiber Filtration by Multiple Thin Layers of Nanofiber Mats (Page 3, Figure 1). Elsevier.	55
4-2 (A) Nuclear spinning moment, (B) Discrete nuclear spin states of nuclei with different spinning momentum.	55
4-3 Diffraction of X-ray with θ of the incident angle by a crystal with the spacing d between diffraction planes.	56
4-4 Design of X-ray spectrometer, top view.	57
5-1 An SEM image of electrospun PAN fibers from PAN 6% w/v DMF.	83
5-2 Fiber diameter distribution of electrospun PAN fibers.	83
5-3 (A) Thermogravimetric analysis of poly vinyl pyrrolidone degradation, and (B) its first derivative to locate the peak. Dried air was flown to the TGA chamber at	

0.04 LPM in 20 psi. Temperature was increased from the room temperature to 1000°C at 10°C/min.....	84
5-4 SEM images of electrospun TiO ₂ fibers from (A) PVP 4% and (B) 16% w/v EtOH after heat treatment. Scale bars are (A) 2 μm and (B) 5 μm.....	84
5-5 Fiber diameter distribution of electrospun TiO ₂ fibers from PVP 4% w/v EtOH.....	85
5-6 Fiber diameter distribution of electrospun TiO ₂ fibers from PVP 16% w/v EtOH.....	85
5-7 (A) d _f and, (B) C _v of as-spun PAN fiber, heat-treated TiO ₂ fibers with different polymer concentration, heat-treated SiC fibers, fibers that compose Millipore HEPA and LydAir HEPA.....	86
5-8 SEM images of as-spun TiO ₂ -SiO ₂ composite fibers from aqueous sol with PVP concentration of (A) 0.25%, (B) 0.5%, (C) 1%, (D) 2% w/v sol. Scale bars are 20 μm.	87
5-9 Dependence of fiber diameter for electrospun fibers of PVP 1% and 2% w/v sol on heat treatment. Connecting lines are for guidance of the eye only.	88
5-10 Electrospun TiO ₂ -SiO ₂ composite fiber from full aqueous sol. d _f is 243 nm.	89
5-11 Fiber diameter distribution of electrospun TiO ₂ -SiO ₂ composite fibers from PVP 1% w/v sol, depending on different heat treatment profile.....	90
5-12 Fiber diameter distribution of electrospun TiO ₂ -SiO ₂ composite fibers from PVP 2% w/v sol, depending on different heat treatment profile.....	91
5-13 SEM images of (A) Millipore HEPA (CAT. NO.: AP1504700, Millipore, MA, USA), (B) LydAir HEPA (LydAir [®] High Alpha HEPA air filtration media-HEPA Lydair grade 4450H, Lydall Filtration, CT). Scale bars are 5 μm.	91
5-14 Quality factor (q _F) of filters with standard deviation calculated by data from Table 5-3.	92
5-15 Chemical structure of GPTMS. Chemically different (A) carbon atoms and, (B) hydrogen atoms are noted by different alphabet subscripts.	92
5-16 ¹³ C-NMR spectra of (from bottom to top) GPTMS, mixture of 0.005N HNO ₃ and GPTMS at molar ratio of 1:1, 2:1, 4:1, 8:1, 16:1 and methanol. The wedges show the peaks from transition states. Peaks are assigned to carbons of GPTMS molecule in Figure 5-15 (A) ⁶⁹	93
5-17 Proposed hydrolysis reaction of GPTMS in aqueous HNO ₃ . Chemically different atoms are noted by different alphabetical subscripts.....	93

5-18 ^1H -NMR spectrum with peaks assigned to hydrogen atoms of GPTMS molecule in Figure 5-15 (B).	94
5-19 ^1H -NMR spectra of (from bottom to top) GPTMS, 0.005N HNO_3 and GPTMS at molar ratio of 1:1, 2:1, 4:1, 8:1, 0.005N HNO_3 and methanol. (A) Peaks of hydrogen atoms of hydroxyl group and, (B) overlapped peaks of water and hydrogen atom of hydroxyl group of methanol.	95
5-20 ^1H -NMR spectra of (from bottom to top) GPTMS, 0.005N HNO_3 and GPTMS at molar ratio of 1:1, 2:1, 4:1, 8:1, 0.005N HNO_3 and methanol. (A) Overlapped regime of hydrogen of water and hydroxyl group of methanol (Figure 5-19 (B)), (B) overlapped regime of hydrogen that is bonded to carbon of methanol and H_e (Figure 5-15 (B)), (C) regime of H_g (Figure 5-15 (B)) as the reference for the integration.....	95
5-21 ^1H -NMR spectra of 0.005N HNO_3 and GPTMS at molar ratio of 1:1 with partial integration of block A, B and C from left to right.	96
5-22 ^1H -NMR spectra of 0.005N HNO_3 and GPTMS at molar ratio of 2:1 with partial integration of block A, B and C from left to right.	96
5-23 ^1H -NMR spectra of 0.005N HNO_3 and GPTMS at molar ratio of 4:1 with partial integration of block A, B and C from left to right.	97
5-24 ^1H -NMR spectra of 0.005N HNO_3 and GPTMS at molar ratio of 8:1 with partial integration of block A, B and C from left to right.	97
5-25 Enlarged ^1H -NMR spectra of Figure 5-19 (A).....	98
5-26 Transition state of GPTMS in the proposed hydrolysis reaction (Figure 5-17). (A) One methoxy group is hydrolyzed, (B) two methoxy groups are hydrolyzed and, (C) fully hydrolyzed GPTHS.	98
5-27 Enlarged ^1H -NMR spectrum of 0.005N HNO_3 and GPTMS at molar ratio of 2:1 in Figure 5-19 (A).....	99
5-28 ^{13}C -NMR spectra of (from bottom to top) [0.005N HNO_3]:[GPTMS]=2:1, TB, [0.005N HNO_3]:[GPTMS]:[TB]=2:1:1 and 1-butanol. The wedges indicate the peaks of 1-butanol. Notations in peak assignment for TB and [0.005N HNO_3]:[GPTMS]=2:1 are based on Figure 5-29 and Figure 5-15 (A), respectively.....	100
5-29 Chemical structure of TB. Chemically different carbon atoms are noted by different alphabet subscripts.....	100
5-30 Proposed condensation reaction between {GPTMS+ HNO_3 } and TB. Chemically different atoms are noted by different alphabetical subscripts.	101

5-31 ^{13}C -NMR spectra of (from bottom to top) $[0.005\text{N HNO}_3]:[\text{GPTMS}]=2:1$ and $[0.005\text{N HNO}_3]:[\text{GPTMS}]:[\text{TB}]=2:1:1$. The wedge indicates the peak of methanol.....	102
5-32 X-ray diffraction pattern of electrospun TiO_2 fibers heat-treated at various temperatures for 3 hours. Peaks notated as A and R indicate anatase and rutile phase, respectively.	103
5-33 TEM images of electrospun TiO_2 fibers heat-treated at (A) 500°C , (B) 600°C , (C) 700°C , (D) 800°C , and (E) 900°C for 3 hours.....	104
5-34 X-ray diffraction pattern of electrospun $\text{TiO}_2\text{-SiO}_2$ composite fibers heat-treated at various temperatures. Peaks marked with wedges indicate anatase phase of TiO_2	105
5-35 TEM images of electrospun $\text{TiO}_2\text{-SiO}_2$ composite fibers from aqueous sol heat-treated at (A) 500°C , (B) 800°C , and (C) 1100°C for 3 hours.....	106
5-36 SEM images of 1100°C -heat-treated electrospun $\text{TiO}_2\text{-SiO}_2$ fibers from sol A. $[\text{TiO}_2]:[\text{SiO}_2]=1:1$. Images are from same batch of sample that show different morphologies, i.e. (A) rough surfaces of fiber and (B) spikes from the fiber.	107
5-37 XRD result of electrospun $\text{TiO}_2\text{-SiO}_2$ composite fibers before and after heat treatment at 1100°C for 3 hours.	107
6-1 (A) Fractured anatase TiO_2 fibermats composed of fibers of $d_f=149\text{ nm}$, (B) A $\text{TiO}_2\text{-SiO}_2$ composite fibermat composed of fibers of $d_f=243\text{ nm}$ from full aqueous sol after heat treatment.	113

LIST OF ABBREVIATIONS

ACF	activated carbon fiber
B	magnetic field
B_p	full-width-at-half-maximum of the peak
BuOH	1-butanol
C_c	gas slip correction factor
$CDCl_3$	deuterated chloroform
$CHCl_3$	chloroform
C_v	coefficient of variation, (standard deviation)/mean
d	spacing between diffraction planes
d_f	mean fiber diameter
d_p	diameter of particles
DI water	deionized water
DMF	N, N-dimethylformamide
DMSO	dimethyl sulfoxide
DMSO- d_6	deuterated dimethyl sulfoxide
E	collection efficiency, applied electric field
E_R	collection efficiency for interception
EtOH	ethyl alcohol, ethanol
F_D	drag force
GPTHS	3- glycidoxypropyltrihydroxysilane
GPTMS	3- glycidoxypropyltrimethoxysilane
HEPA	high efficiency particulate air
h	jet diameter
h_t	terminal jet radius in electrospinning

I	electric current
K	electric conductivity
Ku	Kuwabara hydrodynamic factor
LPM	liter per minute
MeOH	methyl alcohol, methanol
M_w	weight average molecular weight
N	neutron number, number of neutrons
n	number, number of data, number of measurements
NMR	nuclear magnetic resonance
P	particle penetration
PAN	polyacrylonitrile
ppm	part per million
PSL	polystyrene latex
PVP	polyvinylpyrrolidone
Q	flow rate, infuse rate
q_F	quality factor
R	radius of curvature
SEM	scanning electron microscopy
SMPS	scanning mobility particle sizer
SSA	specific surface area
t	size of crystals
TB	titanium (V) n-butoxide
TEM	transmission electron microscopy
TiPP	titanium isopropoxide
TMS	tetramethylsilane

U	face velocity of air
V	air velocity
w/v	weight per volume, g/ml
XRD	X-ray diffraction
Z	atomic number, number of protons
ZP	zirconium n-propoxide
ZB	zirconium n-butoxide
α	porosity of the filter
Δp	pressure drop
γ	magnetogyric ratio, surface tension, gamma
δ	chemical shift, delta
$\delta(A)$	partial charge of A
ϵ	strain, dielectric permittivity, epsilon
η	viscosity of air
θ_B	average of lower and upper limits of the peak in radian
λ	mean free path of air, wavelength, lambda
μ	air viscosity
ν	frequency, nu
ρ_p	particle density
σ	stress, shielding constant, sigma
χ	dimensionless wavelength of the instability in electrospinning, chi
ω	angular frequency, omega
[A]	number of moles of A chemical
{A+B}	mixture of A and B

Abstract of Dissertation Presented to the Graduate School
of the University of Florida in Partial Fulfillment of the
Requirements for the Degree of Doctor of Philosophy

ELECTROSPINNING OF NANOFIBERS FOR FILTRATION MEDIA

By

Hyoungjun Park

May 2010

Chair: Wolfgang M. Sigmund
Major: Materials Science and Engineering

Since particulate impurity is regarded as the primary cause of lung diseases, purification of air has been a crucial issue. Filtration is the most conventional method to obtain clean air, whereby particulate matter is collected on a fibrous media. The use of fibrous filters is prevalent because of their high filtration efficiency and low pressure drop.

Fibrous filters were fabricated via the electrospinning process which can be used to produce continuous submicron-diameter sized fibers. Polyacrylonitrile (PAN) nanofibers with a mean fiber diameter of 224 nm were electrospun to form fibermats. Filtration tests on fibermats of PAN were conducted to confirm that filters of thinner fibers result in higher collection efficiencies and lower pressure drops than that of thicker fibers as predicted by the theoretical filtration mechanism. Results showed that electrospun PAN nanofibermats had a superior quality factor of 0.067 ± 0 compared to 0.031 ± 0.001 by the current state-of-the-art microfiber-based high particulate air (HEPA) filtration media. The verified theory implies that nanofibermats of other types of materials could also be considered as promising filtration media since filtration performance is independent of the material used.

As materials for advanced next-generation filtration media, ceramics are favored over polymeric materials due to their robustness against environmental factors such as ultraviolet rays, abrasive particles, and high temperature all of which degrade and damage the fibrous structure. Amongst various ceramic materials, the anatase phase of TiO_2 was selected due to its mechanical property and versatility as a photocatalyst and microwave-absorbing material.

Anatase TiO_2 fibers were fabricated by electrospinning followed by heat treatment at 500°C for 3 hours. However, early precipitation or gelation of the organic solvent-based TiO_2 sol posed a practical challenge in the sample preparation. In order to enhance stability of the precursor sol, a novel aqueous sol with titanium alkoxide was developed. As the result, the time taken for gelation or precipitation was elongated from 4 hours for the organic solvent-based sol to 4 months with the novel aqueous sol. In seeking the proper chemical composition to attain electrospinnability and maximize the period for storage before gelation, the reaction paths of hydrolysis and condensation for one of the components of the aqueous sol were investigated by nuclear magnetic resonance (NMR) spectroscopy. After hydrolysis and condensation reactions, Si-O-Ti bonds were validated to be formed by the reaction mechanism. TiO_2 - SiO_2 composite fibers were successfully electrospun from the aqueous sol system by addition of a spinning agent followed by heat treatment. In contrast to TiO_2 fibers in which anatase phase was observed after heat treatment at 500°C , anatase phase was formed at 1100°C in TiO_2 - SiO_2 composite fibers. The formation of Ti-O-Ti bonds was retarded due to the formation of Si-O-Ti bonds, as evidenced by the NMR results.

In regard to the microstructure of TiO_2 fibers and $\text{TiO}_2\text{-SiO}_2$ composite fibers with anatase phases, the $\text{TiO}_2\text{-SiO}_2$ composite fibers were observed to have no voids or cleavages on the surface than TiO_2 fibers which have coarse structures created upon crystallization at magnification of x330,000 by transmission electron microscopy. The coarse structure of TiO_2 fibers characterized as having cleavages at exposed surface grain boundaries is anticipated to adversely affect the mechanical stability by enhancing crack formation and propagation which will lead to failure of the fiber. In contrast, amorphous SiO_2 fills in the spaces that have been created by the development of anatase phase for $\text{TiO}_2\text{-SiO}_2$ composite fibers. Smoother surfaces were observed as well in contrast with TiO_2 fibers due to the amorphous SiO_2 in the continuous phase of the composite material. Based on the observations, $\text{TiO}_2\text{-SiO}_2$ composite fibers are expected to have better mechanical stability by reducing the possibility of crack formation and blockage of crack propagation.

The mean fiber diameter of $\text{TiO}_2\text{-SiO}_2$ composite fibers achieved was 243 nm, which is 8% thicker than the PAN fibers achieved and 54% thinner than fibers of the HEPA filter. Hence, the quality factor of the $\text{TiO}_2\text{-SiO}_2$ composite fibers is predicted to be between those of PAN fibermats and the HEPA filter by filtration theory; however it would be closer to that of PAN fibers. Moreover based on transmission electron microscopy (TEM) observation, the mechanical stability was improved as well by achieving denser structures in the fiber than in pure TiO_2 fibers.

CHAPTER 1 INTRODUCTION

Ceramic Fibermats as Filtration Media

In 2002, over 27 million people were estimated to be suffering from respiratory diseases such as asthma, bronchitis, emphysema in the United States ¹ and over 10 million people are killed by lung diseases each year globally ². Particulate matters has been considered as one of the major pathogens of lung diseases ³, which embraces pollens, soils, industrial pollutants, vehicle exhausts. Smaller particles with diameter less than 2.5 μm trigger cardiovascular issues as well. Besides the harm to the human health, accumulation of dust may cause malfunction of electronic devices and mechanical equipment. Hence, removal of these particles has been of great concern especially for the indoor humane facilities—i.e. house, hospital, school, vehicle—where the particles are inclined to be concentrated in the air. Filtration is one of the most commonly applied methods to remove the exterior contaminants for the air purification. Among numerous different types of air filtration systems, fibrous filters that consist of a mat or mats of fine fibers facing perpendicular to the direction of air flow are the most adopted one because of their large surface area to collect the particles, the low pressure drop, and light weight from the high porosity.

In this dissertation, fibrous filtration media were fabricated via the electrospinning process because it is the only processing method that could produce continuous fibers with submicron diameter. Polyacrylonitrile nanofibers were electrospun to verify the filtration theory that shows filters made of thinner fibers have a lower drag force and a higher collection efficiency than those made of thicker fibers. For the wider spectrum of

applications as filtration media in the future, however, ceramic materials are preferred to polymeric materials because of;

- Hardness that could prevent damage by abrasive particles.
- Durability to the chemical reaction that could be induced by harsh environment such as high temperature, high energy ultraviolet rays.

These advantages are sometimes critical especially to habitats with limited resources—e.g. the shelters during warfare, inhabited facilities on the lunar surface also known as the lunar outpost. The regeneration by the microwave irradiation, the photocatalytic behavior could be regarded as auxiliary benefits from certain species of the ceramics. In light of that, TiO₂-based materials were selected based on their mechanical property and additional functionality in the microwave absorption and the photocatalytic activity. Nevertheless, like most of other metal alkoxides⁴, the titanium alkoxide is highly reactive with water molecules in the air to induce the precipitation or the gelation via hydrolysis and condensation reactions. Inhomogeneity and viscosity change caused by the precipitation or the gelation would result in discontinuity in the process, the mechanical failure of fibers and fibermats. In seeking stability of sol without the precipitation or the gelation, the novel aqueous sol towards the TiO₂-SiO₂ composite material was developed to achieve nanofibers via the electrospinning method.

Objectives and Hypothesis

Electrospinning of polymeric materials has been studied while electrospun ceramic nanofibers have been rarely reported until recent years. Since early 2000, various ceramic materials, including TiO₂ by Li et al.⁵, have been successfully electrospun, e.g. CeO₂⁶, ZrO₂⁷, Al₂O₃⁸, BaTiO₃⁹. However, reported achievements are from the sol based on organic solvents that does not hinder the high reactivity of ceramic precursors

towards the precipitation ⁴. To the best of the author's knowledge, the water-based metal alkoxide sol with extended period for gelation compared to the organic solvent-based sol hasn't been published yet to date. And electrospun TiO₂ fibers haven't been fabricated in a macro-scale for a practical use most probably due the mechanical weakness of nanofibers induced by their coarse microstructure ⁵. Therefore, the objectives of this research are;

- To fabricate nanofibermats and measure their quality factors.
- To understand the chemistry to achieve the stable aqueous sol.
- To fabricate anatase TiO₂-based filtration media from the novel aqueous sol.

In order to accomplish the objectives, it was hypothesized that;

- Nanofiber-based filtration media have the higher quality factor from the high collection efficiency and the low pressure drop than microfiber-based filtration media.
- In preparation of the aqueous sol, the hydrolysis of 3-glycidoxypropyltrimethoxysilane (GPTMS) followed by the condensation reaction with titanium (IV) n-butoxide (TB) occurs at the site of methoxy groups of GPTMS. The sol is stabilized in the condition that water molecules were consumed in the hydrolysis reaction with GPTMS.
- A denser microstructure of fibers is accomplished by incorporation of the amorphous SiO₂ phase with the anatase TiO₂ phase from the aqueous sol than the anatase TiO₂ fiber from the organic solvent-based sol.

Approach to Hypothesis

According to Hinds ¹⁰, the good filtration media is one with a high quality factor (equation 1-1) achieved by a high collection efficiency and a low pressure drop. He also showed that the filtration media comprised of thinner fibers have a higher collection efficiency as well as a lower drag force. The drag force is the resistance against the airflow induced by the fiber which causes the pressure drop. It is theoretically shown that the drag force can be exponentially decreased when the fiber diameter is reduced

¹⁰⁻¹². On the other hand, since collecting particulates on the fiber is a very complex process that involves multiple filtration mechanisms at once, the relationship between the fiber diameter and the collection efficiency induced by all filtration mechanisms has not been established yet. Theoretically, however, the smaller fiber diameter tends to increase the collection efficiency in regard with each filtration mechanism. Therefore, the smaller fiber diameter induces not only a weaker drag force that leads to a lower pressure drop, but also the increased collection efficiency which result in the higher quality factor. Polyacrylonitrile nanofibermats and commercially available microfiber-based high-efficiency particulate air (HEPA) filters will be evaluated and compared in respect to the quality factor of filtration. For various functionalities on top of the filtration, the TiO₂-based filtration media are desired in the future. In order to stabilize the sol from which fibermats are composed via the electrospinning, the novel aqueous sol system was developed. The chemistry of the novel aqueous sol will be studied for the first time to seek the proper chemical composition for the fabrication of nanofibers. Based on the sol-gel chemistry of inorganic materials, hydrolysis and condensation reactions are predicted to be triggered at the methoxy groups of GPTMS. The reaction will be validated by analyzing the resultants and the byproducts by the nuclear magnetic resonance (NMR) method. The shelf lives of the sols with different molar ratios will be timed by observation on the chemical with the mechanical stirring. The microstructures of electrospun TiO₂-based fibers will be analyzed by the X-ray diffraction (XRD) and the transmission electron microscopy (TEM) study. By comparing results of TiO₂ and TiO₂-SiO₂ composite fibers, it will be clarified how insertion of SiO₂ affects TiO₂ system in regard with the crystallization behavior and the microstructure.

$$q_F = -\frac{\ln(1-E)}{\Delta p}$$

$$(1 - 1)^{10}$$

CHAPTER 2 BACKGROUND

Filtration

Filtration is the common method to capture the aerosol particles. The two most important parameters in filtration are the collection efficiency, E , and the pressure drop, Δp . The collection efficiency is defined as the portion of particles that were caught by the media while the pressure drop is the pressure difference between before and after the filtration media. By definition, E is equal to $1-P$ where P is the particle penetration. In regard with the quality of filters with different pressure drops and collection efficiencies, it is often inconvenient to evaluate filters with them because some filters have high E and high Δp while others have low E and low Δp . Hence, the parameter called as the quality factor, q_F , was introduced to embrace both of Δp and E as expressed in equation 1-1¹⁰. Better filters with higher E and lower Δp results in the greater q_F value.

Collection of particulates is the purpose of using filtration media. There are largely three mechanisms by which the fibers in the filtration media could collect particulates in the aerosol—the interception, the inertial impaction and the diffusion. In each mechanism, it was assumed that the collection efficiency is for a single fiber and the particles are captured by van der Waals force between the particle and the fiber. The interception occurs when the particle follows the streamline of the airflow that approaches the fiber within a distance of the radius of the particle (Figure 2-1 (A)). The collection efficiency of a single fiber by the interception is expressed as equation 2-1, where E_R is the efficiency for interception, α is the porosity of the filter, d_p is the diameter of particles, d_f is the fiber diameter, K_u is the Kuwabara hydrodynamic factor that can be expressed as equation 2-2. E_R is roughly proportional to an inverse of

square of the mean fiber diameter, i.e. d_f^{-2} ¹³. When the path of the particle is diverted from the airflow because of its inertia, the particle moves across the streamline and hits the fiber as depicted in Figure 2-1 (B). It's called as the inertial impaction and the collection efficiency of a single fiber by the inertial impaction (E_t) is expressed in equation 2-3, where ρ_p is the particle density, C_c is the gas slip correction factor as described in equation 2-4, U is the face velocity of air flow, η is the viscosity of air. E_t is roughly proportional to an inverse of the mean fiber diameter to the three, i.e. d_f^{-3} ¹⁴. Equation 2-5 is for the condition of $d_p/d_f < 0.4$ while there's no simple equation set up for $d_p/d_f > 0.4$. And the particles that were on the streamline that goes around the fiber can be captured by particles because particles can diffuse out of the streamline in the irregular paths, i.e. the Brownian motion (Figure 2-1 (C)). The collection efficiency of a single fiber by the diffusion (E_D) is expressed in equation 2-5, where D is the particle diffusion coefficient. E_D is proportional to the inverse two-thirds of the mean fiber diameter, $d_f^{-2/3}$ ¹⁵. By all three major filtration mechanisms for aerosol particulates, thinner fibers are favored for the filtration media towards the higher collection efficiency.

The pressure drop is caused by resistance of airflow, or the drag force, by the filtration media. The drag force can be decreased by using thinner fibers for filtration based on the Stoke's law as given in equation 2-6. Here F_D is the drag force, μ is the air viscosity, V is the air velocity and C_c is the gas slip correction factor¹⁰. The gas slip correction factor is a function of the fiber diameter and the mean free path of air, λ , which is 66 nm at the standard temperature and pressure, as expressed in equation 2-4

11-12 .

In the experimental set-up to measure E and Δp , a filtration system can be designed in different ways—i.e. number and kinds of fibermat, fibermat support, filter holder, etc. E of each element of the filtration system can be calculated from the penetration, P , by the equation 2-7¹⁶. The subscript s stands for the filter holder and other structures, e.g. tubing, while a, b, \dots means different kinds of fibermats as many as m, n, \dots . Δp of each element of the filtration system can be calculated by the Darcy's law as described in equation 2-8¹⁷. Subscripts and symbols mean same to those in equation 2-7.

For further reading, Hinds¹⁰ discussed the filtration theory in detail.

$$E_R = \frac{(1-\alpha)d_p^2}{Ku(d_f^2 + d_p \cdot d_f)} \quad (2-1)^{13}$$

$$Ku = -\frac{\ln \alpha}{2} - \frac{3}{4} + \alpha - \frac{\alpha^2}{4} \quad (2-2)^{10}$$

$$E_t = \frac{\rho_p d_p c_c U}{36\eta Ku^2 d_f} \left\{ (29.6 - 28\alpha^{0.62}) \left(\frac{d_p}{d_f}\right)^2 - 27.5 \left(\frac{d_p}{d_f}\right)^{2.8} \right\} \quad (2-3)^{14}$$

$$C_c = 1 + \frac{\lambda}{d_f} \left[2.34 + 1.05 \exp\left(-0.39 \frac{d_f}{\lambda}\right) \right] \quad (2-4)^{11-12}$$

$$E_D = 2 \cdot \left(\frac{D}{d_f U}\right)^{\frac{2}{3}} \quad (2-5)^{15}$$

$$F_D = \frac{3\pi\mu V d_f}{C_c} \quad (2-6)^{10}$$

$$P_{total} = P_s \cdot P_a^m \cdot P_b^n \cdot \dots \quad (2-7)^{16}$$

$$\Delta p_{total} = \Delta p_s + m\Delta p_a + n\Delta p_b + \dots \quad (2-8)^{17}$$

Sol-gel Chemistry of Ti Alkoxide

Hydrolysis and Condensation

TiO₂ can be formulated via the hydrolysis and the condensation reactions that involve water molecules and Ti alkoxides as the precursor. In the absence of the

catalyst, both of them occur by the nucleophilic substitution, or the S_N2 mechanism, where S, N, 2 mean the substitution, nucleophilic, and the bimolecular reaction, respectively, as depicted in Figure 2-2. Because of the strong electronegativity of the alkyl groups (-OR) of the Ti alkoxide, the Ti atom becomes a favorite target to be attacked by nucleophiles.

In the hydrolysis reaction (Figure 2-2 (A)), the nucleophile—i.e. the oxygen atom in the water molecule—attacks the Ti atom in the alkoxide from the back. As the -OR group leaves, it takes one of hydrogen atoms in the water molecule to complete the reaction to form Ti with a hydroxyl group (HO-Ti) and an alcohol (R-OH).

There are two different paths to the condensation, which are the alkoxolation and the oxolation as shown in Figure 2-2 (B) and (C), respectively. The alkoxolation is also a kind of the oxolation in that it forms an oxo bridge (-O-) but differentiated from the usual oxolation by the byproduct, an alcohol. In condensation reactions, the nucleophile is the oxygen atom in the hydroxyl group (-OH) of the hydrolyzed Ti. Upon the attack of the nucleophile on the other Ti atom from the back, the alkoxy group in the alkoxolation and the hydroxyl group in the oxolation leave and take the hydrogen atom that was bonded to the nucleophile. As the resultant, a Ti-O-Ti bond, and an alcohol molecule in the alkoxolation or a water molecule in the oxolation are formed.

Acid and Base Catalysts

The molecular structure of TiO₂ can be controlled by the addition of the acid or the base catalysts. In the acidic condition, the leaving group of the Ti alkoxide readily leaves upon the attack of the nucleophile on the Ti atom as shown in Figure 2-3 (A). The hydrolysis is accelerated because the -OR group doesn't need the additional proton transferred from the nucleophile to leave. In the basic condition, the Ti alkoxide gets

deprotonated by the base catalyst (Figure 2-3 (B)). Due to the protonated alkyl group, the electrophilicity of the Ti atom gets weakened, and being less attacked by the nucleophile. Thus, the condensation becomes relatively fast compared to the retarded hydrolysis reaction.

The structure of the resultant TiO_2 depends on the favorite sites for the reaction in the oxo-polymer in different conditions. There are three kinds of sites in the Ti oxo-polymer for the hydrolysis and the condensation reactions as shown in Figure 2-4, and partial charges of each case are listed in Table 2-1¹⁸. In the acidic condition, the leaving group can be easily protonated (Figure 2-3 (A)) in the order of C, B, A from the most negative to the most positive partial charge on the $-\text{OR}$ group. Because the hydrolysis and the condensation reactions occur more often at the site C which is the end of the oxo-polymer than the site A and B, the resultant would be the linear oligomeric TiO_2 . The sol containing the linear TiO_2 is observed as clear homogeneous liquid. In the basic condition, the site A with the most positive partial charge on the $-\text{OR}$ group is the preferred site to attract the OH^- for the deprotonation as described in Figure 2-3 (B). The order of preference of the reaction in the basic condition is A, B, C. Because there are more than 2 sites available for reaction in the site A and B, the Ti oxo-polymer expands via formation of the three-dimensional network to result in precipitations and the inhomogeneous sol.

Electrospinning

Principle

Electrospinning is an electrohydrodynamic phenomenon of liquids observed in the high electric field to form the fibrous morphology. In contrast to the conventional spinning methods that push out the fibers from the material source by the mechanical

force, in electrospinning, difference of electric potential across the space between the source and the collector drives the material to carry electric charges from the source to the collector. In the process, the morphology of the material varies from beads to fibers depending on the concentration of the spinning aid which is commonly polymers dissolved in the spinning solution or sol. The components of the experimental set-up are high voltage supplies, a syringe pump, a syringe with a tip that has electrically conductive surface, the sol or the solution, and a conductive collector as shown in Figure 2-5 (A). The collector may be connected to the voltage supply of opposite charge or grounded depending on the experimental condition. The number of the syringe pump and the syringe may vary as well depending on the experimental set-up. As the syringe pump infuses the sol and the electric field is applied in the system, forces that pull out the sol and forces that resist against them compete as depicted in Figure 2-5 (B). The former group is the normal electric stress, the tangential electric stress, the electric polarization stress, and the gravity while the latter group is the surface tension and the viscosity. When the applied electric field reaches certain strength, the forces that pull the sol out of the syringe tip overcome the forces that resist against ejection. At the moment, the droplet at the tip forms a conical shape. It is named as Taylor cone after the researcher who reported it for the first time ¹⁹. At the apex of the Taylor cone, a jet is spouted and breaks down to charged droplets that are sprayed out when the sol doesn't contain any spinning aid. It named the phenomenon as electrospaying. The breakdown of the jet into small droplets is due to the effect of surface charges that tend to create larger surfaces to decrease the charge density over a larger area while the surface tension tends to keep the droplet large to reduce the specific surface area. At the higher

electric field, the effect of the surface charge is more favored over the effect of the surface tension, which leads to smaller droplets with the larger specific surface area. By adding the polymeric spinning, the viscosity of the sol is increased to retard the formation of droplets by the chain entanglement of the polymer. When the effect of the surface tension and the viscosity at the higher concentration overcomes the breakdown by the surface charge, the jet maintained its fibrous morphology. As the electric field is increased, the effect of the surface charge gets stronger to result in thinner fibers with the larger specific surface area.

After a short flight from the ejection, the behavior of ejected fibers gets unstable which can be described by three different instability modes—i.e. the Rayleigh instability, the axisymmetric instability and the non-axisymmetric instability. In an occasion when the system is highly electrically charged as the electrospinning condition, behavior of the jet is governed by the non-axisymmetric instability in which the jet flies in a random whipping motion at a high frequency. The whipping instability is of crucial importance in the electrospinning process because the fiber gets elongated during the whipping motion that consequently results in the fiber thinning as well. Rutledge and coworkers estimated the fiber diameter from equation 2-6 that was formulated by calculation for the solution with the conductivity of lower than $1 \mu\text{S}/\text{cm}$ ²⁰⁻²², where h_t is the terminal jet radius, γ is the surface tension, ϵ is the dielectric permittivity of the medium which is air, Q is the flow rate, l is the electric conductivity, χ is the dimensionless wavelength of the instability that is an approximation of R/h . R is the radius of curvature and h is the jet diameter. Equation 2-6, however, couldn't be applied to ceramic sols with the higher conductivity. Therefore, Sigmund et al.⁹ developed equation 2-7 based on equation 2-6

for sols with the higher conductivity than a few $\mu\text{S}/\text{cm}$, where E is the applied electric field, K is the electric conductivity, c is an empirical constant. The electrospinning phenomenon is so dynamic in the nano-scale with many experimental parameters that it's difficult to observe and study the behavior in-situ. Hence the relationship between the fiber diameter and experimental parameters has not been clearly elucidated yet. For example, the viscosity was not mentioned in the equations as a parameter affecting the fiber diameter while it was reported as one of the key parameters on the fiber diameter control by other researchers^{5, 23-27}. Thus the equations cannot be applied to all solution systems but gives us a guideline to see the impact on the fiber diameter by the parameters. The experimental parameters that are commonly used to control the fiber diameter are as following;

- High viscosity of the sol decelerates the elongation of fibers in the whipping instability, which tends to result in thick fibers.
- Strong electric field requires a larger surface area to decrease the charge density, which tends to result in thinner fibers with larger specific surface area.
- Slow infusion means less amount of material, which tends to result in thinner fibers.

$$h_t = \left\{ \gamma \varepsilon \frac{Q^2}{I^2} \frac{2}{\pi(2 \ln \chi - 3)} \right\}^{\frac{1}{3}} \quad (2 - 6)^{20}$$

$$\varepsilon \pi \gamma = 2 \pi^2 h^3 \left(\frac{1 - \pi E K h^2}{2 Q} \right)^2 \times \left(2 \ln \left(\frac{c}{h^3 \sqrt{1 - \pi E K h^2}} \right) - 3 \right) \quad (2 - 7)^9$$

Advantage of Electrospinning over Other Fiber Fabrication Methods for Filters

Electrospinning has advantages over the traditional fabrication method of glass fibers, such as the melt-blow spinning, in the controllability of the fiber diameter, the large variety of applicable materials from polymers to ceramics^{9, 28} as well as the theoretically anticipated nano-sized fiber diameter by equation 2-6²⁰ and equation 2-7⁹.

It has also been reported that electrospun fibers of the different polymeric materials had C_v s of lower than 0.30²⁹⁻³⁰. Tsai et al.³¹ reported that, in a strictly controlled experimental condition, melt-blown fibers achieved C_v of as low as 0.02. However, d_f of the corresponding fibers was 13.3 μm . Melt-blown fibers with the submicron range of d_f along with C_v data haven't been published at the best of author's knowledge at the moment.

Table 2-1. Partial charge distribution within the Ti oxo-polymer shown in Figure 2-4 ¹⁸.

Site	$\delta(\text{OR})$	$\delta(\text{Ti})$
A	+0.22	+0.76
B	+0.04	+0.71
C	-0.08	+0.68

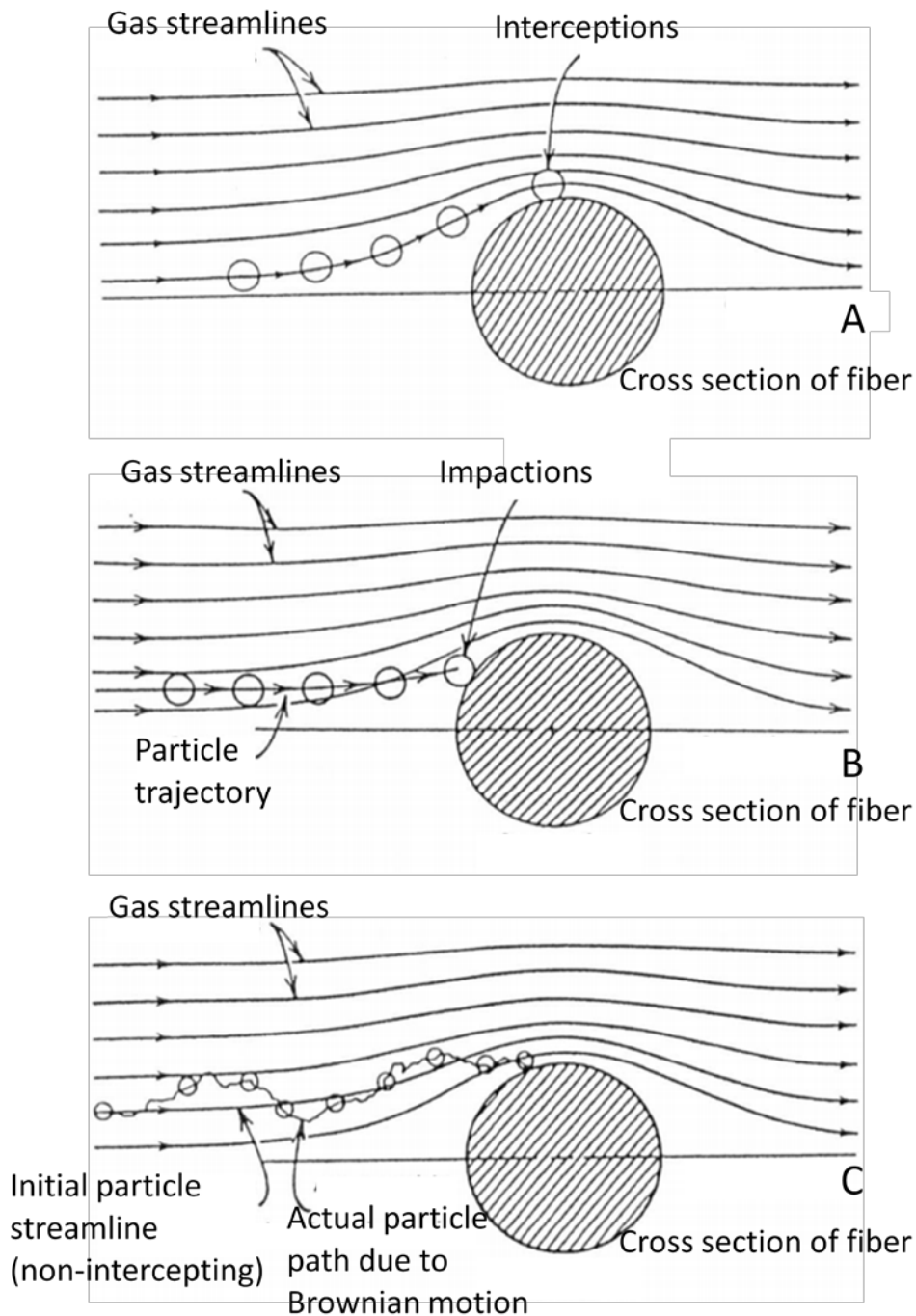


Figure 2-1. Filtration mechanisms of particulates in the aerosol by a fiber, (A) interception, (B) impaction, (C) diffusion¹⁰. Reprinted by permission from Hinds, William C. 1999. Aerosol technology (Page 192, Figure 9. 5., Page 193, Figure 9. 6. Page 194, Figure 9. 7.). John Wiley and Sons, Inc., New York.

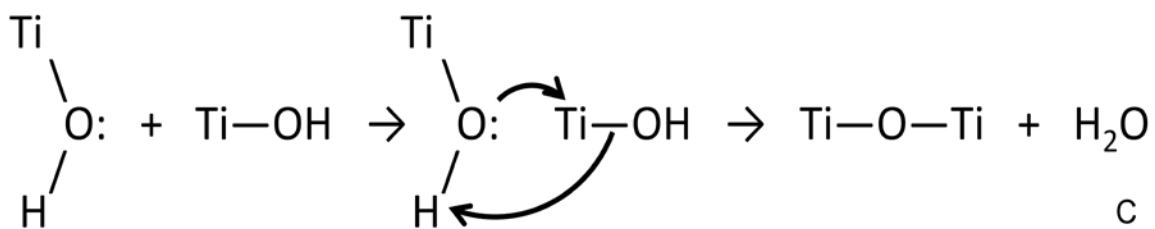
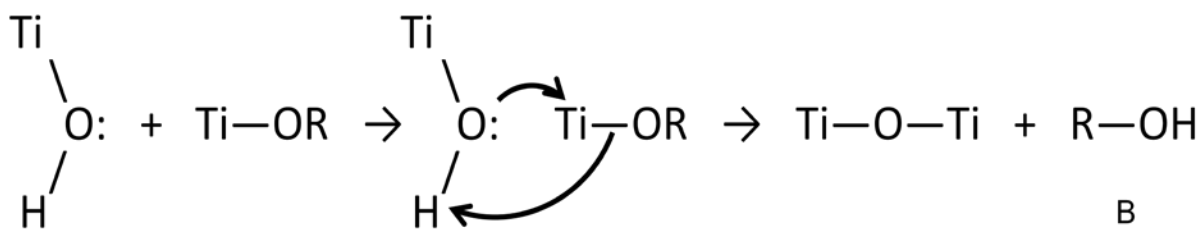
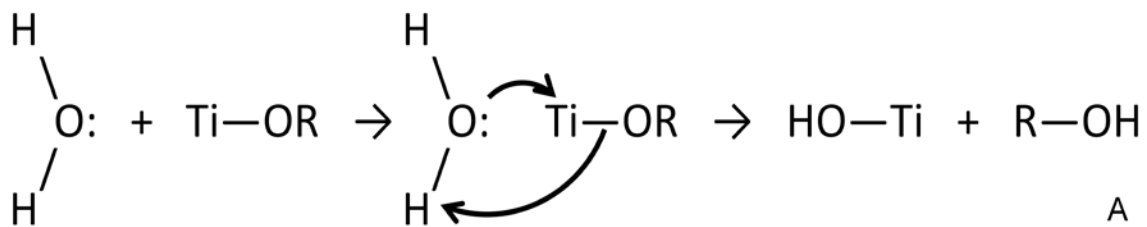


Figure 2-2. A) Hydrolysis, B) alcoxylation, C) oxolation of Ti alkoxide. R means the alkyl group.

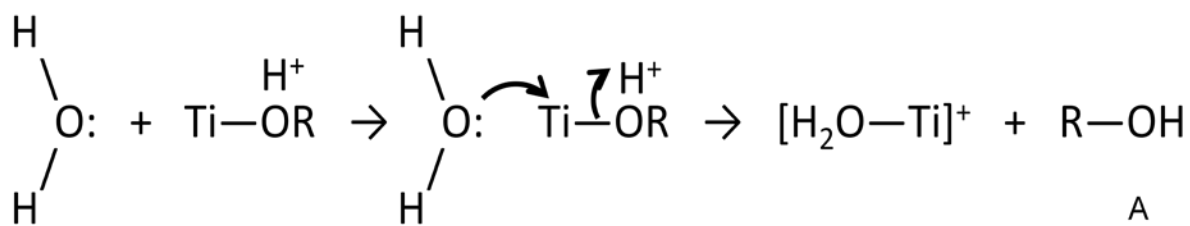


Figure 2-3. Hydrolysis in (A) acidic condition and (B) basic condition

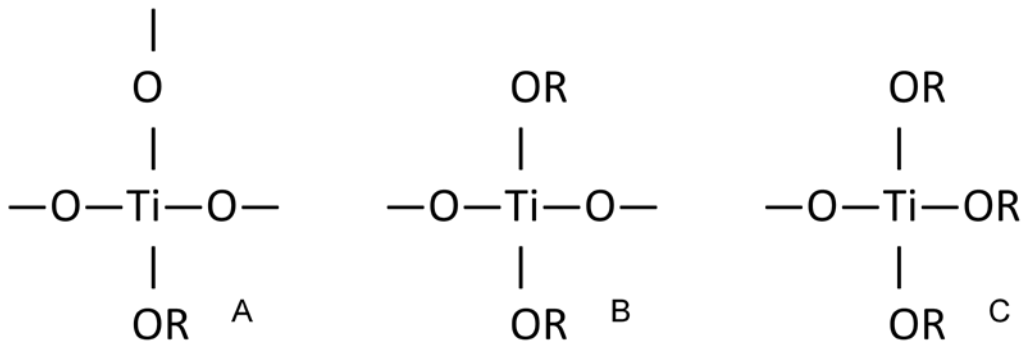


Figure 2-4. Different Ti sites in Ti oxo-polymers.

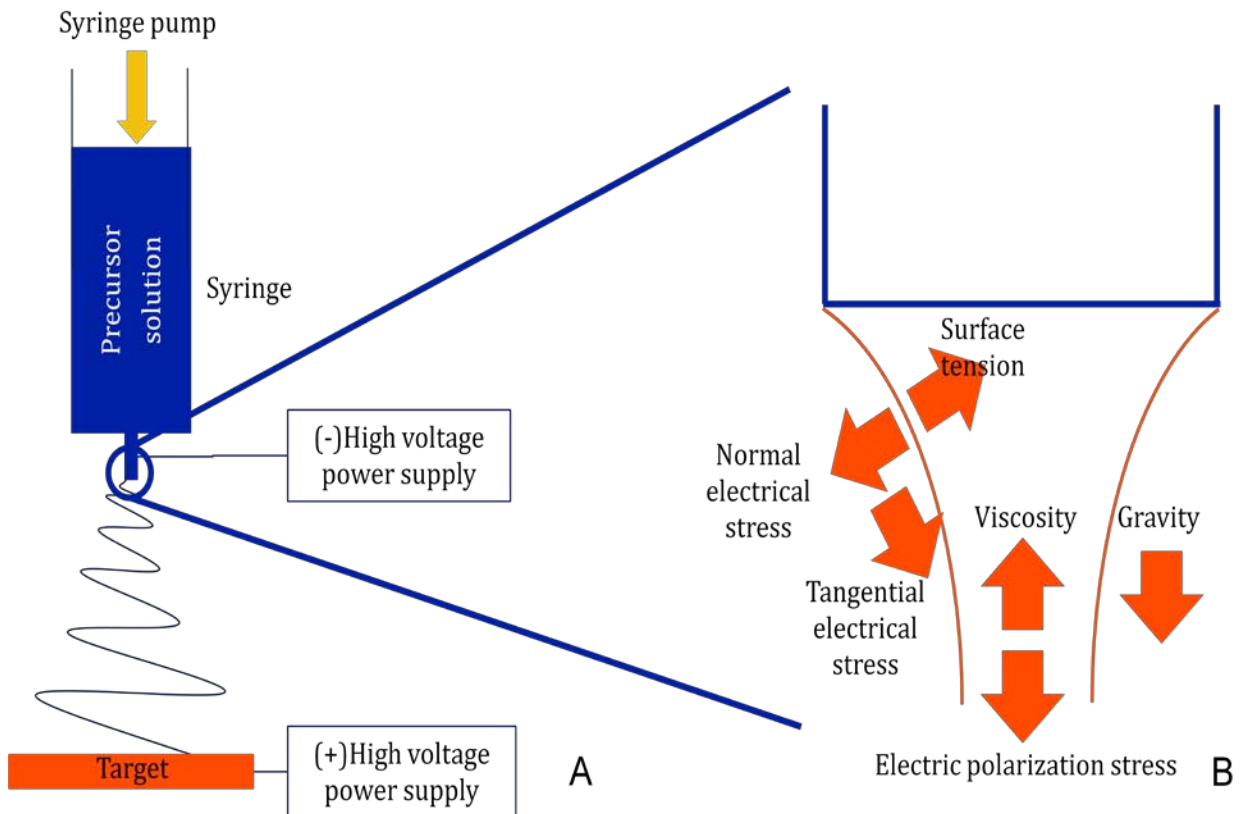


Figure 2-5. (A) Schematic set-up of electrospinning, (B) forces applied to the liquidic sol or solution at the syringe tip.

CHAPTER 3 FABRICATION OF FIBERMATS

Electrospinning PAN and Filtration Test

Polyacrylonitrile

Polyacrylonitrile, or PAN, is a polymer that has acrylonitrile as the repeating unit (Figure 3-1). As carbon-based materials—e.g. carbon fiber, graphite, etc—get more and more attention due to their exceptional mechanical and electrical properties, so does PAN as a precursor towards carbon materials³²⁻³⁵. Electrospinning of PAN has been reported³⁴ as well as the convertibility to carbon material.

Polymer Solution Preparation and Electrospinning

PAN (M_w 150,000, Pfaltz & Bauer, CT) 6% weight per volume (w/v, g/ml) in N,N-dimethylformamide (DMF, 99.8%, Sigma-Aldrich, MO) solution was prepared after the mechanical stirring at 80°C for an hour. The solution was loaded in a plastic syringe (5 ml, Luer-Lok, Becton, Dickinson and Company, NJ) with a gauge-15 needle tip (inner diameter 1.499 mm, outer diameter 1.829 mm, stock No. JG15-1.5X, Jensen Global Inc. CA) attached. The syringe was fixed on the syringe pump (PHD2000, Harvard Apparatus, MA) with the needle tip connected to the high negative voltage power supply (ES30N-5W, Gamma High Voltage, FL). The circular collector of 5 cm in diameter was covered by a sheet of aluminum foil (Fisher Scientific, NH) and connected to the high positive voltage power supply (ES30P-5W, Gamma High Voltage, FL). Nanofibers were electrospun when the needle tip and the collector were charged by 0.75 kV/cm of the electric field over 20 cm of the tip-to-collector distance at 1 ml/hr of the infusion rate. The electrospinning process was continued to form a fibermat for the intended time. After the electrospinning was completed, the fibermats were heated at 160°C in the box

furnace (controlled by model No. F47925-80, Barnstead International, IA) for an hour to evaporate the solvent, DMF ³⁶.

Set-up for Filtration Test

Activated carbon fibermats (ACF, article No. ACC-507-15, American Kynol, Inc.) were used to sandwich each electrospun PAN fibermat because electrospun fibermats were not mechanically strong enough to be practically handled due to its thickness of less than 100 μm . ACF mats were adopted because they were known to have a low collection efficiency, a low pressure drop and have enough mechanical strength to support electrospun fibers for filtration tests. When the multi-layered PAN fibermats were tested, ACF mats were placed between each PAN fibermat—e.g. ACF/PAN/ACF/PAN/ACF/... as shown in Figure 3-2.

In regard to the aerosol, the HEPA standard measures the collection efficiency against particles of 300 nm in diameter. Therefore, 300 nm-monodispersed polystyrene latex (PSL, Cat. No. 5030, geometric standard deviation~1.05, Thermal Scientific, CA) particles were dispersed in the deionized (DI) water at the concentration of 2 g/l followed by addition of the same volume of ethanol (EtOH) in order to ensure the dispersion of PSL particles and reduce the surface tension for better nebulization ³⁶.

TiO₂

Property

TiO₂ has 8 different crystalline phases in principle ³⁷ among which the anatase, the rutile and the brookite are the stable phases while other 5 phases are formed only by high pressure processing ³⁸⁻⁴⁰. Among them, the anatase phase is the most versatile. Anatase TiO₂ can be readily heated up by electromagnetic wave in the range of microwave due to its high dielectric permittivity ⁴¹ while it has been the most promising

photocatalytic material⁴²⁻⁴³ because of the large bandgap of 3.2 eV and slower recombination rate of the hole and the electron compared to the rutile phase. Moreover, the anatase phase boasts the superb mechanical property —e.g. 88 GPa of the elastic modulus⁴⁴ and 4 GPa of the hardness⁴⁵ by the nano-indentation method. The elastic modulus was measured on the 80 nm-thick anatase film while the hardness was measured on the 600 nm-thick anatase film. The crystal structure of the anatase phase is tetragonal with $a=b=3.784 \text{ \AA}$ and $c=9.515 \text{ \AA}$ ⁴⁶ as depicted in Figure 3-3.

Sol Preparation

1 mole of titanium (IV) n-butoxide (TB, 99%, Acros Organics) was added to the mixture of 4 moles of acetic acid (AA, glacial, Fisher Chemical) and 2 moles of ethanol (EtOH, 99.5%, anhydrous, 200 proof, Acros Organics) followed by the mechanical stirring for 10 minutes in a capped bottle. This sol was added to 18 moles of EtOH containing polyvinylpyrrolidone (PVP, M_w 1,300,000, Acros Organics) followed by the vigorous stir for an hour in a capped bottle. The overall molar ratio of chemicals in the sol was [TB]:[AA]:[EtOH]=1:4:20 while PVP concentrations were 4% and 16% w/v EtOH each for different sols.

Electrospinning and Heat Treatment

After the stirring for an hour, the sol was fed to the plastic syringe with a gauge-15 syringe tip attached immediately to avoid the precipitation due to the high reactivity of TB to humidity in the air. The syringe tip was connected to the negative voltage supply while the collector was connected to the positively voltage supply. The overall electrospinning set-up was same to that of PAN fibers. The electric field applied was 1kV/cm over 20cm tip-to-collector distance at 0.5ml/hr of infuse rate by the syringe pump. Collected fibers were heat-treated at various temperatures from 500°C to 900°C

for 3 hours in air by the same box furnace in the fume hood used for PAN fibers. The furnace was heated from the room temperature to the intended temperature at 10°C/min and left to be cooled down with samples inside after the 3-hour-treatment. In consequence, the specimen that was heat-treated at higher temperature was exposed to heat for a longer period.

TiO₂-SiO₂ from Aqueous Sol

Reasoning of Adopting Aqueous Sol

It has been observed that preparation of ethanol-based TiO₂ sol was failed by the precipitation of TiO₂ due to high reactivity of titanium alkoxides to humidity in air. The failure ratio reaches up to 50% that wastes time and resources. Even after the successful sol preparation, the precipitation has been observed in the syringe during electrospinning to fabricate fibermats. Hence, novel aqueous sol towards TiO₂-SiO₂ composite material with outstretched the time taken for gelation of 4 months was developed as a consequence of the pursuit of stability in the sol without precipitation or gelation. The time for completion of gelation is determined when the sol does not flow in the glass vial located upside down. Moreover, the electrospun TiO₂ fibermat was reported to have a coarse microstructure inside the fiber with cleavages on the rough surface⁵ by crystallization from the amorphous to the anatase phase. The microstructure is speculated to deteriorate the mechanical stability of the fiber because cracks would be generated at the tip of the cleavage by focused stress and propagate through the fiber to result in failure of the fiber. On the other hand, TiO₂-SiO₂ composite material is expected to develop a dense microstructure of fibers due to the amorphous SiO₂ phase that would constitute the continuous phase in the composite. When the composite material is heat-treated at 500°C for crystallization of the anatase of TiO₂^{5, 47-}

⁴⁹, SiO₂ that has the crystallization temperature of 1500°C ⁵⁰ to the α-quartz phase keeps its amorphous phase. At the elevated temperature, SiO₂ is expected to be transported to fill in the spaces created by polymorphic TiO₂ phases, which brings the dense structure.

Sol Preparation

1 mole of 0.005N HNO₃ in the deionized water and 0.5 mole of 3-glycidoxypropyltrimethoxysilane (GPTMS, 97%, Acros Organics) were mixed followed by addition of 0.5 mole of TB in 10 minutes and mechanically stirred for 1 hour to form the sol A. 22 moles of 0.005N HNO₃ in the deionized water with PVP and 0.5 mole of GPTMS were mixed followed by addition of 0.2 mole of tetraethyl orthosilicate (TEOS, 98%, Acros Organics) in 2 hours and mechanically stirred for 2 hours to form the sol B. The sol A with PVP 12% w/v sol was prepared for electrospinning along with the full aqueous sol. The concentration of PVP, which was adopted as the spinning aid, was varied as 0.25%, 0.5%, 1% and 2% w/v full aqueous sol to control the electrospinnability of the sol. The sol A and B were mixed followed by the vigorous stirring for 1 hour to achieve the homogeneous aqueous sol. The overall molar ratio of chemicals in the complete aqueous sol is [0.005N HNO₃]:[GPTMS]:[TB]:[TEOS]= 23:1:0.5:0.2. The procedure of sol preparation is depicted in Figure 3-4 as well.

Electrospinning and Heat Treatment

The electrospinning procedure and the heat treatment process for TiO₂-SiO₂ composite fiber is same to that for TiO₂ fibers aforementioned. The electric field applied was 1 kV/cm over 20 cm distance between the tip and the circular collector covered by the aluminum foil. The infuse rate was 0.6 ml/hr. Electrospun samples were heat-treated

at 500, 800 and 1100°C. After the heat treatment, fibers from sol A and the full aqueous sol have the molar composition of TiO₂-SiO₂ at 50%-50% and 29%-71%, respectively.

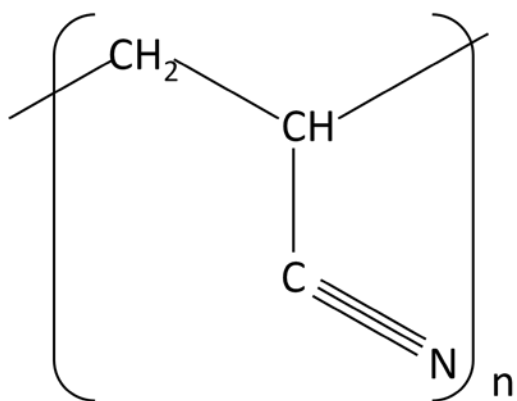


Figure 3-1. Chemical structure of polyacrylonitrile.



Figure 3-2. Electrospun PAN fiber mat sandwiched by two ACF mats.

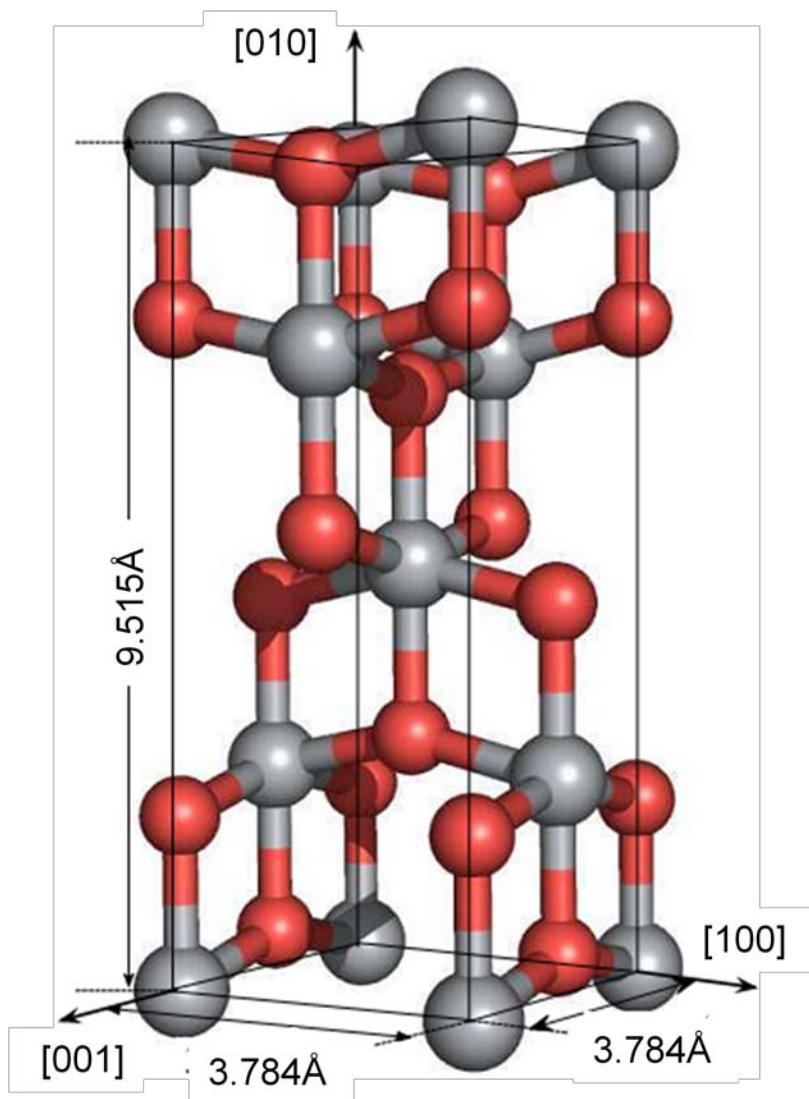


Figure 3-3. Crystal structure of anatase phase of TiO_2 ^{43, 46}. Gray spheres (or brighter spheres in the black/white print) are Ti atoms while red spheres (or darker spheres in the black/white print) are O atoms. Reprinted by permission from Pyrgiotakis, Georgios. 2006. Titania Carbon Nanotube Composites for Enhanced Photocatalysis (Page 7, Figure 2-1). University of Florida, FL.

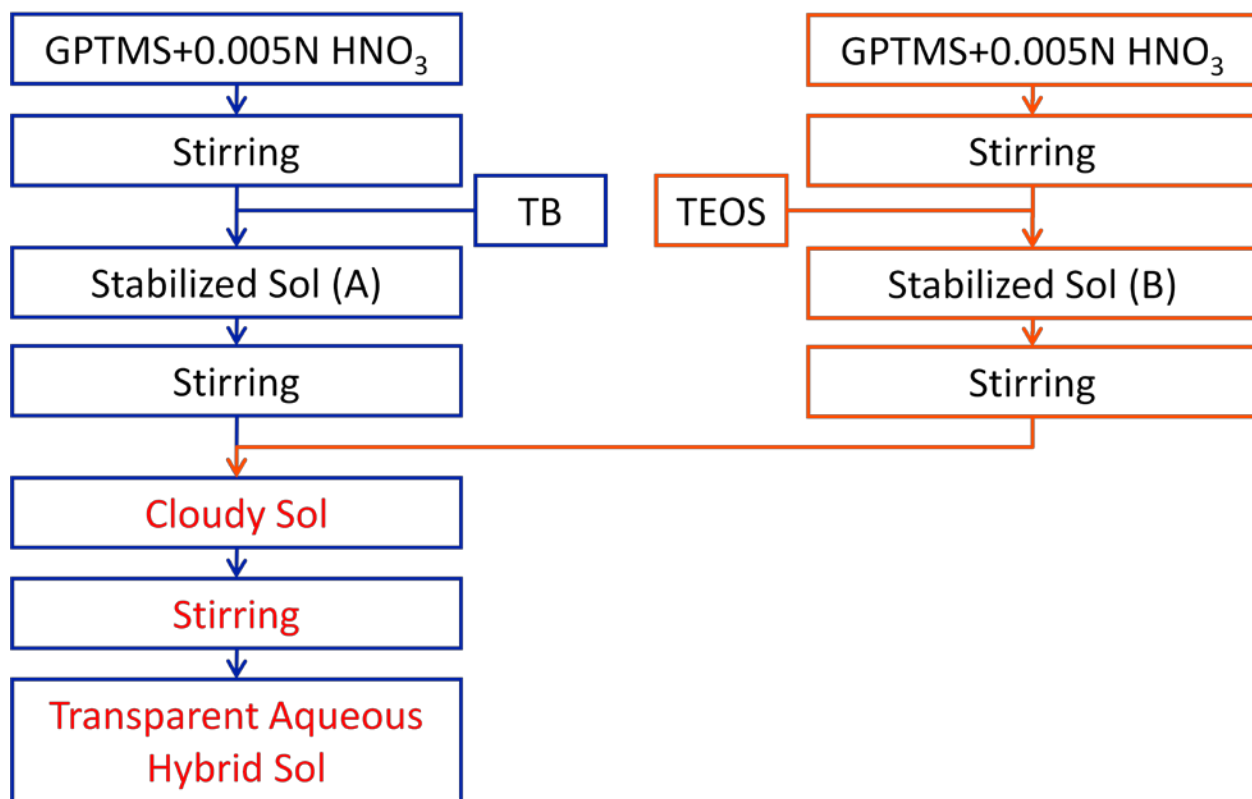


Figure 3-4. Preparation procedure of the aqueous sol.

CHAPTER 4 EXPERIMENTAL METHODS

Fiber Diameter

Scanning Electron Microscopy

Scanning electron microscopy (SEM, JSM 6400, JEOL) is a characterization method to observe the surface morphology of objects. Magnification ranges over 6 orders of the magnitude from $\times 10$ to $\times 500,000$ depending on the equipment.

Magnification of $\times 50,000$ was the highest for the current SEM that was used to take discernible images of nano-sized fiber samples.

When the beam of electrons from the electron gun hits the sample, among other signals, secondary electrons are generated as a result of the interaction between the electrons and the atoms at or near the surface of the sample. Based on the detected signal of the secondary electrons in a raster scan pattern, the image of the sample is constructed. The surface of the sample must be electrically conductive and grounded in order to avoid the charge accumulation on the surface. When the electronic charge is accumulated at the surface of the sample, electrons are deviated from the path and the interaction between the electrons and the atoms at the surface gets distorted that results in a damaged image—e.g. blur. Since electrospun PAN fibers or TiO_2 -based fibers were not conductive enough to avoid the issue, all the samples observed in this dissertation by SEM were coated with carbon by the coater (Ion Equipment Corporation) at 5×10^{-5} mmHg for 1 minute.

Image Analysis

Fiber diameters from the SEM images were measured by ImageJ, the image analysis software (<http://rsb.info.nih.gov/ij>, National Institutes of Health, USA). Before

any measurement on each image, the number of pixels over the scale bar must be calibrated by the given length of the scale bar in the corresponding image. Then the length across the fiber in perpendicular to the fiber axis was measured manually for each fiber. Fiber diameters of all the fibers that were shown in the image were measured. Each single fiber was measured once, and the spot in a fiber for measurement was randomly selected. Because the areal density of fiber deposition varies by samples, the number of images taken by SEM per each sample varied from 5 to 20 in order to get images of about 100 fibers at least. Total number of measurements (n) on one sample ranged from 100 to 250 and measured data were saved and analyzed to calculate d_f and C_v .

Filtration Test

The experiments on filtration were carried out by colleagues at the Aerosol and Particulate Research Laboratory by Dr. Chang-Yu Wu in Department of Environmental Engineering Sciences, University of Florida. The collection efficiency, E , and the pressure drop, Δp were measured and the quality factor, q_F , for filters were calculated based on measured data of E and Δp . The experimental set-up is shown in Figure 4-1. The clean and dry air was flowed out from the gas cylinder and split into two ways—one way to the six-jet collision nebulizer (Model CN25, BGI Inc., MA) at the flow rate of 5.5 liter per minute (LPM) to generate the aerosol and the other way at 11 LPM to completely dry the aerosol in the dilution dryer. Afterwards the aerosol was lead to pass through filtration media with the Magnehelic differential pressure gauge (Model 2010, Dwyer Instruments, IN) before and after filtration to measure the pressure drop. The face velocity of the air was controlled at 5.3 cm/s for circular filters with the diameter of 47 mm. 5.3 cm/s is the minimum face velocity required to test HEPA filters according to

the military HEPA standard, MIL-F-51079D⁵¹. The effective diameter of the filter was 40.5 mm due to the filter holder structure. The collection efficiency was measured by analyzing number and size distribution of particles from the aerosol before and after filtration using scanning mobility particle sizer (SMPS, Model 3936, TSI Inc., MN). There's a split air path to control the flow distribution and pressure over the whole system by a valve.

Sol-gel Chemistry of Aqueous Sol

In order to understand the reason of the extended time taken for gelation in the aqueous sol system, the chemistry of the aqueous sol-gel system was investigated using the nuclear magnetic resonance (NMR, Mercury 300 BB) spectroscopy. The goal is to get a detailed picture of the reaction path for the aqueous sol-gel system.

Nuclear Magnetic Resonance

An atom consists of nucleus surrounded by negatively charged electrons. The atomic nucleus contains neutrons and positively charged protons. The numbers of protons and neutrons in the atomic nucleus are called as the proton number (Z) and the neutron number (N), respectively. Atoms that have even Z and odd N , odd Z and even N , or odd Z and odd N have spinning angular momentum that gives the magnetic moment with the magnetic dipole in the magnetic field, B_0 (Figure 4-2 (A)). The angular frequency of the precession ω_0 , induced by B_0 , is linearly proportional to B_0 with the ratio γ , called as the magnetogyric ratio which is the characteristic constant for different nuclei. The relationship between these parameters is described in equation 4-1, where ω is the angular frequency, ν is the precession frequency. Nuclei like ^1H or ^{13}C have two discrete nuclear spin states developed by B_0 . Upon absorption of the electromagnetic wave that has ΔE with the frequency ν_0 , spins in the lower energy state flip into the upper energy

state. Those excited spins return to the lower energy state when the electromagnetic wave stops being applied. This phenomenon is called as the nuclear magnetic resonance. For the proton at a field strength of 1.4 T and room temperature, spins in the lower energy state is more than spins in the upper energy state as many as 0.001%⁵² when calculated by equation 4-2. n_{upper} is the number of spins in the upper state, n_{lower} is the number of spins in the lower state, ΔE is the energy difference between the lower and the upper state, k is the Boltzmann constant, T is temperature, h is the Planck constant. Due to the small amount of spins that generate signals, induced NMR signals have been too weak to be detected or analyzed for a long time. Another obstacle that NMR spectroscopy had was scarcity of ^{13}C in the nature. Carbon is very important in the field of organic or organometallic chemistry. However, ^{12}C cannot create the NMR signal because of its even Z and A , hence, no magnetic moment. Alternative target was ^{13}C ; however, only 1.1%⁵² of carbon atoms in the nature exist as ^{13}C isotope. That also induces the problem of the weak signal intensity. Recent technological advancement like enhanced sensitivity and the Fourier transformation method makes the NMR spectroscopy a viable and rather preferred option for study on the structure and the reaction in the organic and the organometallic chemistry. Adoption of the Fourier transformation dramatically increased the number of measurements in a given time to amplify the signal.

$$\omega_0 = 2\pi\nu_0 = \gamma B_0 \quad (4 - 1)$$

$$\frac{n_{upper}}{n_{lower}} = \exp\left(-\frac{\Delta E}{kT}\right) = \exp\left(-\frac{h\nu_0}{kT}\right) = \exp\left(-\frac{h\gamma B_0}{2\pi kT}\right) \quad (4 - 2)^{52}$$

Chemical Shift

When the external magnetic field, B_0 , is applied, the atom with the electron cloud rotates according to the left-hand rule. At the same time, the rotation of the electron cloud that surrounds the atom in the same direction induces magnetic field B' in the opposite direction of B_0 by the right-hand rule. Then net applied field strength, B , is weaker than B_0 because it is 'shielded' by B' as expressed in equation 4-3, where σ is the shielding constant. The lower electron density around a nucleus means less shielding which results in higher B and the precession frequency, ν_i . Then, this nucleus interacts with the electromagnetic wave with the higher frequency. However, if the location of the signal is presented in the precession frequency in the spectrum, it would cause confusion because the frequency is dependent on B , and B is dependent on B_0 (equation 4-3) which is not a constant value but an arbitrary experimental parameter. Therefore, the peak location needs to be calibrated by a reference material, e.g. tetramethylsilane (TMS, $(\text{CH}_3)_4\text{Si}$) for ^1H and ^{13}C -NMR. TMS is regarded as one of the most shielding material for its hydrogen and carbon atoms because of the low electronegativity of Si, 1.7⁵³. The calibrated unit for peak location is called as the chemical shift, δ , which is expressed in equation 4-4. The chemical shift is dimensionless but often expressed as ppm as consequence of the factor of 10^6 . In the spectrum, the chemical shift on x-axis decreases from the left to the right. The lower chemical shift area is called as the upfield or the high field while the higher chemical shift area is called as the downfield or the low field. For example, when a proton is close to an atom with a high electronegativity in ^1H -NMR, the electron density around the proton would be low because electrons are attracted by the adjacent atom with the high electronegativity. Then this proton does not shield B_0 much which leads to large $\Delta\nu$,

large δ and consequently positioning of the corresponding peak in the downfield. On the contrary, when the proton is far from an atom with the high electronegativity, its electron density is high so that the induced magnetic field by the electron cloud shields B_0 much. Then B becomes small with small $\Delta\nu$, small δ and consequently positioning of the corresponding peak in the upfield.

Given that δ depends on the environment of the corresponding nucleus, nuclei in the same environment should have identical δ . The condition for the same environment here is the chemical equivalence which is satisfied when the nuclei have either of the symmetry operation, i.e. an n-fold axis or plane symmetry, or the conformation, i.e. the free rotation. For example, protons of ethylene (C_2H_4) have both of the rotation and the plane symmetry. Protons of the methyl group in toluene do not have any symmetry due to the phenyl group but they are chemically equivalent because of free rotation by the bond between the carbon in the methyl group and the carbon in the phenyl group. Further discussion of the theoretical aspects of NMR may be obtained from the books by Gunther⁵², Breitmaier et al.⁵⁴ and Freeman⁵⁵.

$$B = B_0 - B' = B_0(1 - \sigma) = \frac{2\pi\nu_i}{\gamma} \quad (4 - 3)$$

$$\delta = \frac{\nu_i - \nu_{ref} (Hz)}{\nu_{ref} (MHz)} = \frac{(\nu_i - \nu_{ref})(Hz)}{\nu_{ref} (MHz)} \times \frac{MHz}{10^6 Hz} \quad (4 - 4)$$

Sample Preparation

725 μ l of the desired sample was loaded to the disposable grade NMR sample tubes (Cat. No. 897193-0000, Kimble Chase Kontes, NJ). For analysis on the hydrolysis reaction, mixtures with the molar chemical ratio of $[0.005N HNO_3]:[GPTMS]=0:1, 1:1, 2:1, 4:1, 8:1, 16:1$ were prepared. For analysis on the condensation reaction, a mixture

with the molar chemical ratio of $[0.005\text{N HNO}_3]:[\text{GPTMS}]:[\text{TB}]=2:1:1$ was prepared. Different solvents were selected and added to the tube according to the sample to avoid any chemical reaction or immiscibility with the sample and mixed by vortex mixer. For ^{13}C -NMR, deuterated dimethyl sulfoxide (DMSO- d_6) was used as solvent for most samples except for TB with which was immiscible. For ^1H -NMR, mixture of DMSO- d_6 and dimethyl sulfoxide (DMSO) was used as the solvent. For TB, deuterated chloroform (CDCl_3) and the mixture of CDCl_3 and chloroform were used as solvents for ^{13}C -NMR and ^1H -NMR, respectively. DMSO and CHCl_3 were added as the reference for the calibration of NMR peaks.

Reproduction of Spectrum

Raw data were converted to the spectrum and analyzed by KnowItAll[®] Informatics System (ver. 8.0, Bio-Rad Laboratories, Inc., NJ). All spectra were calibrated by the location of the carbon peak in deuterized solvents and the hydrogen peak in same chemicals to deuterized solvents for ^{13}C -NMR and ^1H -NMR, respectively, by the reference ⁵⁶ as shown in Table 4-1.

Microstructure

X-ray Diffraction

Principle

X-ray diffraction (XRD, Philips APD 3720) is a useful tool to characterize the crystalline phases and the grain size of the corresponding phase of any material that has long-range order in atomic level.

When the incident beam 1 and 2 hit atoms at θ of the incident angle, beams interact with atoms and are scattered. Because they're scattered in all directions, the scattered beams annul one another—i.e. the destructive interference—in most cases.

However, scattered beams would be completely in phase and reinforce the amplitude each other—i.e. the constructive interference—when certain conditions are satisfied (Figure 4-3);

- Atoms are arranged with the long-range order.
- The path difference, ABC, is equal to a whole number n of wavelength λ as expressed in equation 4-5, which called as the Bragg's law, where λ is the wavelength of the beam and d is the spacing between diffraction planes.

When $n=1$, the path differences between all adjacent diffraction planes are λ , those between every second diffraction planes are 2λ , those between every third diffraction planes are 3λ , and so on. The number of scattered beams in phase that strengthen the amplitude each other depends on the degree of the long-range order which is also called as the crystallinity. In a well-developed crystal, the scattering is strong and is called as the diffraction. Depending on the value of λ and d , there could be $\theta_1, \theta_2, \theta_3, \dots$ that satisfies Bragg's law with $n=2, 3, \dots$. By analyzing the locations of peaks at $\theta_1, \theta_2, \theta_3, \dots$, the crystalline phase can be determined because every crystalline phase has different crystal structures and spacings d , hence, intrinsic peak locations. Usually peak locations are expressed as 2θ because the detector is designed to have 2θ to the incident X-ray beam in usual XRD instruments as shown in Figure 4-4.

The grain size was calculated from XRD result by the Scherrer's formula (equation 4-6), where t is the size of crystals, B_p is the full-width-at-half-maximum of the peak, θ_B is the average of lower and upper limits of the peak in radian. Details of the theoretical and experimental aspects of XRD may be obtained from the literatures⁵⁷⁻⁵⁸.

$$n\lambda = 2d \sin \theta \quad (4 - 5)$$

$$t = \frac{0.9\lambda}{B_p \cos \theta_B} \quad (4 - 6)$$

Sample Preparation and Operation

The fiber mat sample was ground to powder by a mortar and a pestle. Sample powder was attached to a glass slide (No. 13-0800, petrographic slides, Ward's Natural Science Establishment, Inc., NY) by the double sided tape. It was scanned continuously in the desired range of 2θ at the scan speed of $0.02^\circ 2\theta/s$. The wavelength λ of X-ray was 0.15404 nm from $K\alpha_1$ of the copper source.

Transmission Electron Microscopy

The transmission electron microscopy (TEM, TEM 200CX, JEOL) was used to observe the structure and the size of the grains in TiO_2 fibers. By observing the microstructure, macroscopic properties of material—e.g. mechanical property—can be predicted. The grain sizes calculated from XRD results would be compared with grains in the image as well.

Principle

TEM is a microscopic technique of observing samples from the interaction between electrons and the specimen. After the electrons are accelerated from the gun, they're focused by the condenser lens on the specimen. The electrons interact with, pass through the sample and are detected by the fluorescent screen or the CCD camera. The magnification of TEM images reaches up to several million times which is higher than SEM images because of the quality of the detected signal. In SEM, the detected signals to build images are weaker because they are randomly-scattered secondary electrons from the sample surface by the incident electron beam. Since detected signals are original incident beams after interaction with the sample in TEM, the signals has higher intensity with less noise compared to SEM, which leads to the higher resolution and magnification. Hence, the thickness of specimen against the

incident electron beam has to be less than a micron in order to let the electron beams transmit the sample and reach the detector.

Sample Preparation

The sample were immersed in EtOH (99.5%, anhydrous, 200 proof, Acros Organics) and sonicated to be shattered into pieces by ultrasonicator (S3000, Misonix Inc., NY) for 10 minutes. Pieces of the sample were collected on the TEM grid (Cat. No. 01814-F Ted Pella, Inc., CA) by scooping the sample in EtOH with the grid. The specimen was properly deposited on the grid by evaporation of EtOH for an hour in ambient air.

Table 4-1. Reference of the chemical shift for ^{13}C - and ^1H -NMR.

	Solvent	Atom	δ (ppm)
^{13}C -NMR	DMSO- d_6	C of DMSO- d_6	39.51
	CDCl_3	C of CDCl_3	77.16
^1H -NMR	DMSO- d_6	H of DMSO	2.54
	CDCl_3	H of CHCl_3	7.26

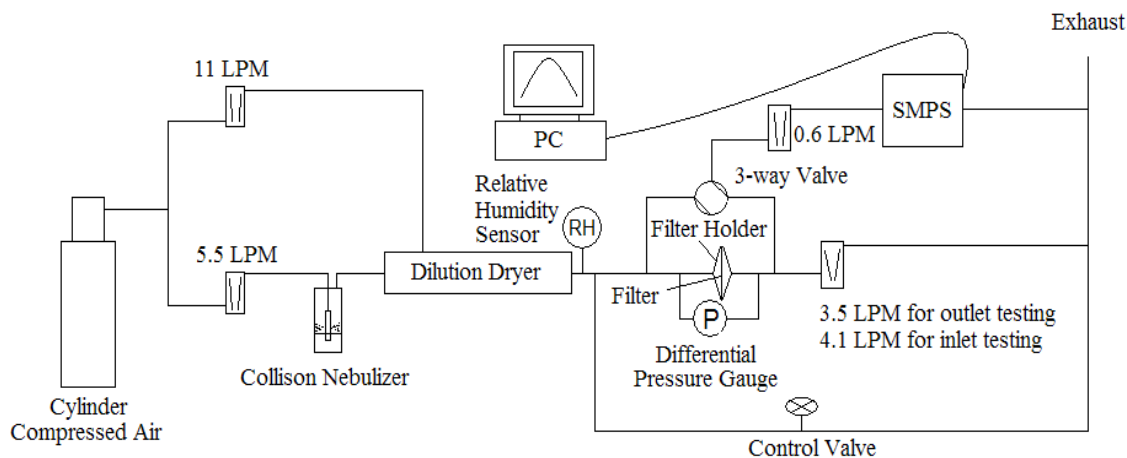


Figure 4-1. Experimental set-up for the filtration test³⁶. Reprinted by permission from Zhang, Qi et al. 2010. Improvement in Nanofiber Filtration by Multiple Thin Layers of Nanofiber Mats (Page 3, Figure 1). Elsevier.

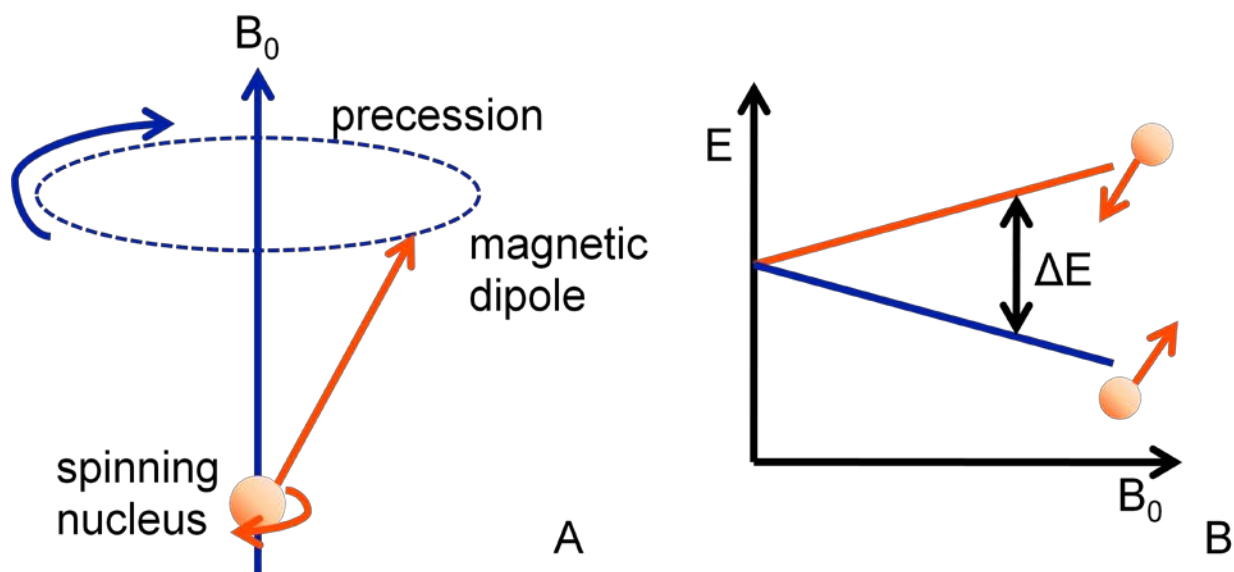


Figure 4-2. (A) Nuclear spinning moment, (B) Discrete nuclear spin states of nuclei with different spinning momentum.

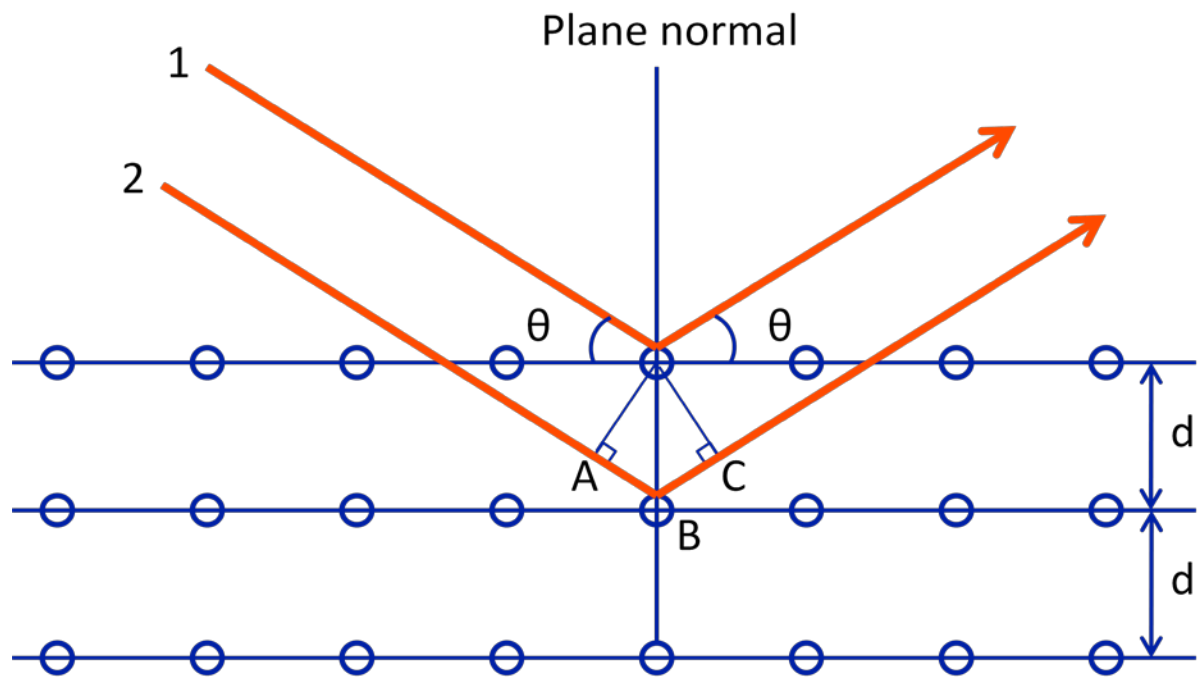


Figure 4-3. Diffraction of X-ray with θ of the incident angle by a crystal with the spacing d between diffraction planes.

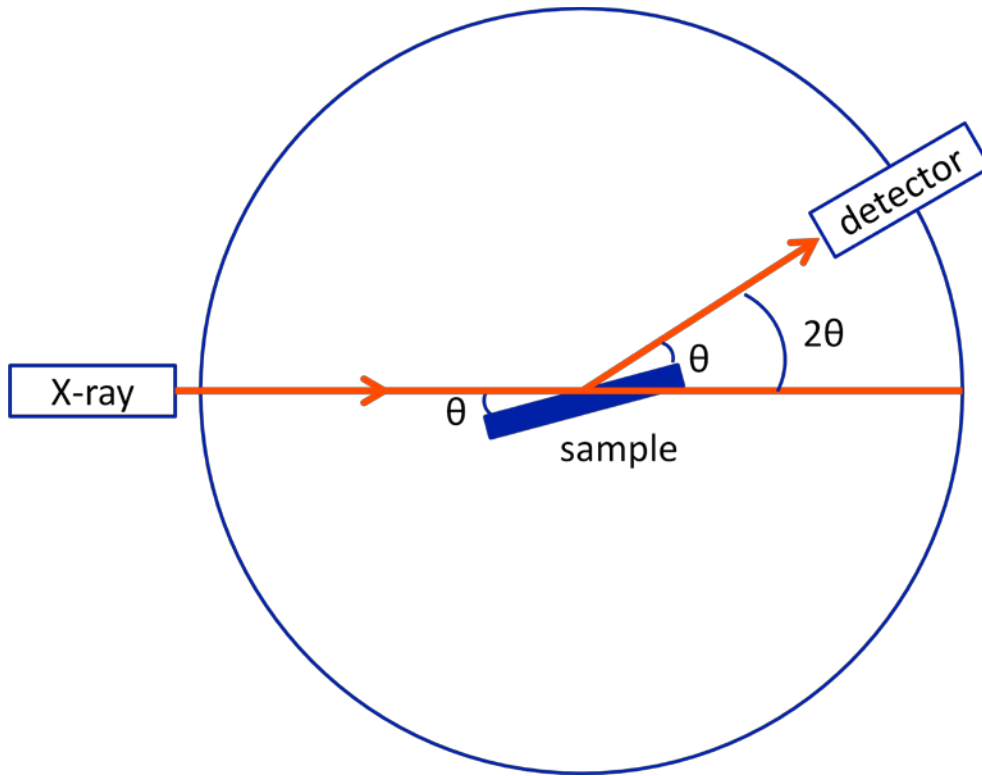


Figure 4-4. Design of X-ray spectrometer, top view.

CHAPTER 5 RESULTS AND DISCUSSION

Fiber Diameter

Results and Discussion

Electrospun samples of PAN, TiO₂, and TiO₂-SiO₂ composite fibers were observed under SEM and analyzed in regard with the fiber diameter. Images taken by SEM were analyzed by the image analysis software. The number of measurements (n) for each sample was 100 at least.

Fiber Diameter and Coefficient of Variation

Electrospun PAN fibers for the filtration test have the mean fiber diameter (d_f) of 224 nm and the coefficient of variation (C_v) of 0.25. They have smooth continuous morphology and stacked on each other as shown in Figure 5-1. Result of analysis on fiber diameter is shown in Figure 5-2. The number of measurement (n) was 189. The fiber diameter has the uni-modal distribution with the center at d_f that implies a stable electrospinning of fibers throughout the process. The measured fiber diameter matches the reported result on the same condition of the solution and electrospinning⁵⁹.

Electrospun TiO₂ fibers from sols with different concentrations of the polymer spinning aid, i.e. PVP, were analyzed and compared after the heat treatment at 500°C for the degradation of PVP and the phase transformation of TiO₂ to the anatase phase. PVP is reported to be thermally degraded at around 420°C⁶⁰⁻⁶². Temperature for the thermal degradation of PVP was experimentally shown in result of thermogravimetric analysis (TGA, Mettler Toledo TGA/SDTA 851e, Figure 5-3 (A)). The dried air was flown to the TGA chamber at 0.04 LPM in 20 psi. The temperature was increased from the room temperature to 1000°C at the ramp rate of 10°C/min to mimic the experimental

condition of the heat treatment for TiO₂-based fiber fabrication. Result of 1st derivative of the TG (Figure 5-3 (B)) locates the thermal degradation temperature of PVP at 433°C which is 13°C higher than the literatures. However, since it is still 67°C lower than the lowest holding temperature for the heat treatment for TiO₂-based fibers, the error of 13°C is not expected to affect the crystallization behavior of TiO₂. The phase transformation behavior upon the heat treatment is discussed in the XRD study in one of the following chapters. TiO₂ from PVP 4% w/v EtOH has d_f of 149 nm and C_v of 0.24 (n=166) while TiO₂ from PVP 16% w/v EtOH sol has d_f of 1110 nm and C_v of 0.20 (n=127) as compared in Figure 5-4. The analysis result on the fiber diameter is presented in Figure 5-5 and Figure 5-6. d_f of electrospun TiO₂ fiber is increased remarkably mainly due to the increased viscosity by the higher polymer concentration from 4% to 16% w/v EtOH and the infuse rate from 0.5 ml/hr to 2 ml/hr as predicted by equation 2-6 and the reported result by other researchers^{5, 23, 63}. d_f of the electrospun TiO₂ fiber from 4% w/v EtOH is 149 nm which is about 50% larger than that of about 100 nm from same sol reported by Li et al.⁵. It could be attributed by the higher infuse rate of 0.5 ml/hr compared to 0.2 ml/hr in the literature in order to avoid the blockage at the tip. The effect of infuse rate on fiber diameter is shown in equation 2-6. Due to the high reactivity of TB to water molecules—i.e. humidity in air—there grows the white cluster, which is presumed to be the composite of the amorphous TiO₂ and PVP, from the syringe tip during electrospinning of the TiO₂ precursor sol in a minute from the beginning of the processing. When the infuse rate is not high enough to overcome the rates of the hydrolysis and condensation reactions of TB, the tip is completely blocked and the sol is irregularly spit out from the tip because the syringe pump still keeps

pushing the sol out. For Li et al.⁵ who needed about 100 measurements for the research on d_f , one-minute-electrospinning would produce 100 nm-diameter-fibers as long as 3 km which would provide enough number of measurements in SEM images. Length of the fiber was calculated based on the assumption that the fibers had the monodisperse fiber diameter at 100 nm with the cross section of perfect circle, the density of the anatase phase is 3.89 g/cm^3 ⁶⁴ and the conversion ratio of TB to TiO_2 is 100%. For the fabrication of fibermats, the sol needed to be electrospun rather continuously because the deposition time towards filtration media ranged from 5 minutes to several hours. 0.5 ml/hr was the lowest infuse rate that was found in the current experimental set-up to achieve continuous electrospinning without blockage.

The result of measurements on the fiber diameters for both of PVP 4% and 16% w/v EtOH samples show the bi-modal distribution (Figure 5-5, Figure 5-6) which purports instability in electrospinning. However, it didn't critically damage the consistency in the fiber diameter because C_v s of 0.24 and 0.20, respectively, are smaller than that of electrospun PAN fibers with the uni-modal fiber diameter distribution as shown in Figure 5-7 and Figure 5-2.

Figure 5-8 shows as-spun fibers for TiO_2 - SiO_2 composite fibers from the aqueous sol imaged with SEM. The sols contain PVP at the concentrations of 1% and 2% w/v sol. The sols were electrospinnable and formed fibers with submicron diameters stacked on top of each other in a random mesh. Lowering PVP concentration to 0.25% w/v sol caused the formation of droplets and beads. This may be interpreted as lacking chain entanglement of the polymer. For the higher concentration of PVP 0.5% w/v sol, fibers appeared that evidenced PVP chains began to be entangled to induce formation

of continuous fibers while the beads were still dominant. By increasing the PVP concentration to 1% and 2% w/v sol, beads became rare and smooth fibers were prevalently observed.

The here reported observations in morphologic changes of electrospun material based on polymer concentrations was also reported by other researchers with various polymers^{5, 28, 63, 65}. With existence of none of or small amount of polymer, electrospun material readily forms spherical droplets to reduce the specific surface area. On the contrary, charges on the surface of droplets tend to be distributed over larger area of the surface and drive the electrospun material towards small droplets or thin fibers. By adding more polymers, higher viscosity and more entangled chains retard the breakdown of electrospun jet to droplets. When the effect of the chain entanglement and the viscosity overcomes that of the surface tension, the electrospun jet retains its fibrous morphology and deposited on the collector⁶⁶.

Upon the heat treatment, the fiber diameter from PVP 2% and 1% w/v sol was decreased by 62% and 48%, respectively, as shown in Figure 5-9. The shrinkage in fiber diameter is accounted for by degradation of PVP and mass transport of TiO₂ to fill in pores which were created by degradation of PVP^{5, 49, 63, 67}. Mass transport of the material to fill in pores created by removal of binder is commonly observed in the conventional metal oxide sintering. With pores inside, the total surface energy of the material would be high because of the large area of the interface between the material and pores. In order to reduce the total surface energy, the surface area should be decreased and it is accomplished by filling in pores by mass transport⁶⁷⁻⁶⁸. When the one-dimensional fiber diameter shrinkage ratios are powered by three to be converted

to three-dimensional PVP volume, the volume shrinkage ratio of fibers from PVP 2% to PVP 1% w/v sol is 2.08 that matches well to the PVP concentration ratio. The fiber diameters were increased by 10% and 11% for PVP 1% and 2% w/v sol samples, respectively, after the heat treatment at 1100°C compared to 800°C-heat-treated samples. There is not a significant difference in percentage of fiber diameter thickening between the two because they are composed of chemically same material after PVP is degraded at 433°C. This is attributed by the phase separation of TiO₂ from TiO₂-SiO₂ network. The lowest mean fiber diameter of composite fibers achieved with anatase TiO₂ is 243 nm (Figure 5-10) from PVP 1% w/v sol after heat treatment of 1100°C. The crystallization and the phase development of the composite fiber is discussed in the XRD study in one of the following chapters.

Electrospun fibers from PVP 1% w/v sol keep the uni-modal distribution in the fiber diameter through the heat treatment while as-spun fibers from PVP 2% w/v sol have the bi- or multi-modal distribution in the fiber diameter (Figure 5-11, Figure 5-12). Through the heat treatment process, however, the fiber diameter distribution from PVP 2% w/v sol shaped to the uni-modal distribution probably because the 50 nm-bin is too large to distinguish the drastically reduced fiber diameter in detail for the original bi-modal distribution to be observed. It would be difficult to reduce the fiber diameter further down from 243 nm only by varying the concentration of PVP with dominantly smooth fiber morphology. The difference between the lowest PVP concentration for smooth fibers and the highest concentration that has beads as majority in morphology was 0.5%. Varying the concentration of PVP in this small range hardly affects the property of the whole sol. Other options that would help attain thinner fibers are addition of surface

agents for the lower surface tension, addition of electrolytes for the higher electric conductivity of the sol or modification of the composition of chemicals—i.e. [005N HNO₃]:[GPTMS]:[TB]:[TEOS]—to reset all parameters to completely different range which have much more subjects to investigate.

Summarized data of d_f and C_v of electrospun fibers and commercial HEPA filters are presented in Figure 5-7. Electrospun fibers of PAN, TiO₂, and TiO₂-SiO₂ composite material were compared with two conventional HEPA filters— Millipore HEPA (CAT. NO.: AP1504700, Millipore, MA, USA) and LydAir HEPA (LydAir[®] High Alpha HEPA air filtration media-HEPA Lydair grade 4450H, product that is equipped by U.S. Army, Lydall Filtration, CT). Figure 5-13 showed the SEM images of the HEPA filters. The analysis results show the electrospinning can fabricate more consistent fibers over from hundred nanometers to a few micrometer in fiber diameter with different materials than HEPA filters, given that the fiber fabrication process for HEPA filters was optimized to produce thinnest and the most uniform fibers in fiber diameter as possible. The enhanced uniformity in fiber diameter leads better quality control towards the intended fiber diameter processing.

Conclusion

Fiber diameters of electrospun fibers from the various sols were analyzed and the summarized result is presented in Table 5-1 and Table 5-2. d_f of PAN fibers for the filtration test was 224 nm. The fiber diameter of TiO₂ fibers from the organic sol was significantly increased from 149 nm to 1110 nm after the heat treatment by increasing the concentration of PVP from 4% to 16% w/v EtOH. TiO₂-SiO₂ composite fibers from the aqueous sol were successfully electrospun and the morphology was changed from sprayed beads to smoothly spun fibers by increasing PVP concentration. The lowest d_f

achieved for TiO₂-SiO₂ fiber with the anatase phase is 243 nm. Electrospun fibers demonstrated excellent consistency in the fiber diameter with C_vs less than 0.3 regardless of the material and the fiber diameter, compared to microfibers from commercial HEPA filters with C_vs over 0.7.

Filtration Test

Results and Discussion

The penetration, P, and the pressure drop, Δp, of different layered PAN fibermats with ACF mats were measured and substituted into equation 2-6 and equation 2-8, respectively, to calculate P and Δp of PAN fibermats only. When Darcy's law was applied, PAN fibermats and ACF mats were assumed to act independently as filtration media. The exponential regression for P and the linear regression for Δp are shown below;

$$P_{\text{total}}=1.02 \times 0.931^n, \text{ or } \ln P_{\text{total}}=-0.0719n+0.0195, R^2=0.935$$

$$\Delta p_{\text{total}}=10.6n+4.17 \text{ (Pa)}, R^2=0.999$$

P and Δp of the single ACF mat are found to be 0.931 and 10.6Pa, respectively. Based on this result, net effect of different number of ACF mats on P and Δp could be calculated. For example, when two ACF mats sandwiched a PAN fibermat, effect of P and Δp are 0.871 and 21.2Pa, respectively. The result of the filtration test were recalculated for calibration accordingly and shown in Table 5-3 and Figure 5-14. q_Fs of all the PAN fibermats tested are higher than the military standard while q_Fs of two samples composed of PAN 5 (PAN fibermats that were formed by 5-minute deposition of electrospun PAN fibers) fibermats exceeds that of LydAir HEPA filter that is currently used U.S. Army. PAN 5x3 (3-layered PAN fibermats that were formed by 5-minute deposition of electrospun PAN fibers) sample shows superior q_F of 0.067±0 to q_F of

0.023±0.002 of PAN 15 in spite of the same amount of PAN fiber deposition. It is due to the inconsistency of deposition over the sample. In the electrospinning process, the fibers are supposed to be randomly deposited which practically does not happen. Therefore, in a single fiber mat, there are regimes with lower areal fiber densities and regime with higher areal fiber densities. When the single fiber mat is used as the filtration media, the particulates in the air pass through the low-fiber-density regime to result in low E. At the same time, Δp is not decreased accordingly because the air stream still hits the high-fiber-density regime and caused turbulence before it is finally directed to the low-fiber-density regime. By forming the multi-layered fiber mat system, this issue could be resolved by overlapping multiple layers of fiber mats for the compensation in the fiber density or thickness of the fiber mat. The effect of multi-layered fiber mats is clearly shown when filtration data of PAN 5x3 and PAN 15 in Table 5-3 are compared. PAN 5x3 has lower P, i.e. higher E, and lower Δp which leads to higher q_F than PAN 15. q_F of PAN 15 is lower than not only PAN 5 that has same d_f , but also LydAir HEPA of which d_f value is higher than twice. It could be accounted for by the further inconsistency as the deposition time gets longer.

Conclusion

It was hypothesized that the nanofiber-based filtration media has higher q_F than the microfiber-based filtration media as predicted by equation 2-6, equation 2-4 and Hinds¹⁰. The hypothesis was confirmed by comparing q_F values of the uniformly coated PAN nanofiber mat, PAN 5x3, with HEPA filters. In addition to that, it was found that the multi-layered fiber mats achieved higher q_F than a single layer fiber mat with the same total amount of fiber deposition by enhance the uniformity of the fiber deposition over the media. Since the fiber diameter is the factor that affects filtration parameters

according to equation 2-6 and Hinds¹⁰ but type of material is not, the drag force that induces the pressure drop was increased by 13% when 243 nm-diameter TiO₂-SiO₂ composite fibers instead of 224 nm-diameter PAN fibers based on equation 2-6 and equation 2-4. The increment by TiO₂-SiO₂ composite fibers could be regarded to be slight compared to that by LydAir HEPA. F_D of LydAir HEPA with d_f of 527 nm is calculated to be 221% higher than the PAN fiber mat.

Chemistry of Aqueous Sol

Results and Discussion

Hydrolysis Reaction

The mixture of GPTMS and HNO₃ has been investigated by ¹³C-NMR. Peaks of GPTMS were assigned based on the literature⁶⁹. When HNO₃ was added, new peaks were appeared near the peaks of carbons *a*, *b*, *c*, and *d* (Figure 5-15). These carbons were affected much compared to carbon *e*, *f* and *g* by the hydrolysis because they are either the carbon of the methoxy group that was hydrolyzed or the carbons that are adjacent to the methoxy group. Therefore, those new peaks could be assigned to the carbons *a*, *b*, *c*, *d* of partially hydrolyzed GPTMS in the transition state and fully hydrolyzed GPTMS which is GPTHS. The wedges in Figure 5-16 show the carbons in the transition state. As more HNO₃ was added from the bottom to the top, GPTMS became more hydrolyzed. At the ratio of [0.005N HNO₃]:[GPTMS]=4:1 or higher, peaks from the transition states were not clearly observed which implied full hydrolysis. Shifted peaks of carbon *b*, *c* and *d* could be regarded as corresponding carbons of GPTHS. The peak of carbon *a* in Figure 5-15 (A) shifted to the downfield to form a peak for the methanol which was assumed to be the byproduct of the reaction in Figure 5-17.

For the quantitative analysis on chemicals and, especially, water molecules, ^1H -NMR was used on the same mixture in order to confirm the hypothesized reaction in Figure 5-17. ^1H -NMR peak assignment of GPTMS was preceded further experiments because it hasn't been reported yet for the moment. Peaks were assigned to each chemically different hydrogen atom by comparing its relative integration with the number of chemically equivalent hydrogen atoms and the chemical shift of each peak based on the electronegativity of adjacent atoms to hydrogen atoms (Table 5-4, Figure 5-15 (B), Figure 5-18). The peak of hydrogen *a* was clearly recognized by the relative integration of 9. There are three peaks with integration of around 2 at 0.6 ppm, 1.6 ppm and 3.4 ppm. These were assigned to hydrogen *b*, *c* and *d*, respectively, in the order of the distance from oxygen that has the relatively high electronegativity in the molecule. Hydrogen *d* which shields the applied magnetic field the least and has lowest δ among them had its corresponding peak located in the most downfield while the peak of hydrogen *b* was located in the upfield due to the opposite reason to hydrogen *d*. The integrities of the rest of the peaks near which new peaks were not developed didn't change either. Accordingly, they were not involved in any of the hydrolysis and condensation reactions. The peaks at 3.65 ppm, 3.25 ppm were assigned to two hydrogen *e* atoms and peaks at 3.1 ppm were assigned to hydrogen *f* based on the same rational process applied to the peak assignment of hydrogen *b*, *c*, *d*. The peak at 2.54 ppm is for the hydrogen in DMSO as the reference but it is also overlapped with hydrogen either of *g* or *h* while one of them was on the peak at 2.7 ppm. Although hydrogen *g* and *h* are bonded to the same carbon atom—carbon *g* in Figure 5-15 (A), they are not chemically equivalent because there is no plane symmetry between them.

The epoxy ring of GPTMS restrains the free rotation of bonds of carbon *g* to carbon *f* and oxygen atom. In the viewpoint of the plane of epoxy ring, one of hydrogen *g* or *h* is at the same side to hydrogen *f* while the other one is at the same side with the rest of the GPTMS molecule.

When HNO₃ was added to GPTMS, new peaks appeared at around 6 ppm and 4.3 ppm (Figure 5-19) and they were analyzed assuming that those chemicals react as hypothesized in Figure 5-17. In regard to peaks at around 4.3 ppm, the regime of new peaks was close to hydrogens of water and, especially, splitting of peaks from the sols of [0.005N HNO₃]:[GPTMS]=1:1, 2:1 look same to that from the hydrogen of the hydroxyl group in methanol. Also, the shape and the integration of the peak at 3.15 ppm that represents hydrogen bonded to carbon atom in methanol was changed as more 0.005N HNO₃ is added. For those reasons, it is assumed that;

- 4-4.5 ppm: the overlapped regime of hydrogen atoms of water and the hydroxyl group in methanol. Figure 5-20 (A). Integration of $A=2x[H_2O]+1x[MeOH]$.
- 3.15 ppm: the overlapped regime of one of H_e in GPTMS and hydrogen bonded to carbon atom in methanol. Figure 5-20 (B). Integration of $B=3x[MeOH]+1x[GPTMS]$.
- 2.65 ppm: the reference peak of H_g in GPTMS for the integration analysis of overlapped peaks listed above. Figure 5-20 (C). Integration of $C=1x[GPTMS]$.

The integrations of regime A, B and C in Figure 5-20 from each sol was measured as shown in Figure 5-21, Figure 5-22, Figure 5-23 and Figure 5-24 followed by the calculation to get sums of [MeOH] and [H₂O] for each sol which is supposed to be same to added [0.005N HNO₃]. Based on the integration of each regime presented in Table 5-5, sums of [MeOH] and [H₂O] were calculated for each sol and compared with theoretical values (Table 5-6). The error varies from 1% to 10% which are in the

acceptable range for these overlapped peaks⁷⁰⁻⁷¹. Therefore, the assumption of peak overlap indicated in Figure 5-20 was confirmed.

In regard to the peaks at around 6 ppm, the integrations of peaks from sol of [0.005N HNO₃]:[H₂O]=1:1 and 2:1 were same in the acceptable error range⁷⁰⁻⁷¹ to the integrations of the hydrogen peak of the hydroxyl group in methanol (Figure 5-25). Based on results of Table 5-6, it could be assumed that the peaks at 4.1 ppm are not related to water, but only to methanol. When GPTMS and water molecules react as hypothesized in Figure 5-17, same moles of methanol and the hydroxyl group bonded to the Si atom in GPTMS are formed. Thus, these peaks could be regarded as hydrogen peaks from the silanol (Si-OH) group in different environments. Three dominant peaks from left to right were assigned to GPTHS and two transition states from GPTMS to GPTHS. Chemical structures of each species are depicted as C, B and A in Figure 5-26, respectively. The peaks with low intensities between these dominant peaks could be assigned to hydrogen atoms of the silanol groups in the different condensed environment based on the electronegativity of adjacent atoms (Figure 5-27). Comparison of the integration was not useful for these peaks because neither amount of partially and fully hydrolyzed GPTMS nor amount of each hydrolyzed GPTMS involved in the condensation reaction was not discernable by characterization methods used. Although these peaks existed, they were hardly distinguished at the higher molar ratio of [0.005N HNO₃]:[GPTMS] due to their relatively low intensity compared to the dominant peak at 3.2 ppm in Figure 5-20 (B).

Condensation Reaction

Condensation reaction with the addition of TB to sol of [0.005N HNO₃]:[GPTMS]=2:1 were studied by ¹³C-NMR. When TB was added to mixture of

[0.005N HNO₃]:[GPTMS]=4:1, TiO₂ particles were precipitated immediately by the hydrolysis and condensation reactions between TB and water molecules that were left over after hydrolysis reaction. When sol of [0.005N HNO₃]:[GPTMS]=1:1 was used to achieve sol A, the attempt to electrospin fibers from sol A was not successful because of its high viscosity from lack of water. TB was added at the same molar ratio to form sol A with molar ratio of [0.005N HNO₃]:[GPTMS]:[TB]=2:1:1. According to the observation on the time taken for gelation of TB in varying molar ratio (Table 5-7), sol A attains the longest time for gelation when [TB] is twice of [GPTMS]. However, probably due to the excessive amount of TB in sol A, full aqueous sol system became unstable and TiO₂ particles precipitated when sol B was added. Stable full aqueous sol was success accomplished when sol B was added to sol A with molar ratio of [0.005N HNO₃]:[GPTMS]:[TB]=2:1:1, which has the second longest time for gelation of around 4 weeks before gelation at which the sol didn't flow down when the capped glass vial was put upside down. In Figure 5-28, sol of the third spectrum from the bottom is from the mixture of two below it. Chemical structure of TB along with subscripts for chemically different carbon atoms is presented in Figure 5-29. Wedges in Figure 5-28 indicate the formation of 1-butanol which is the byproduct of hypothesized reaction in Figure 5-30. The enlarged spectrum of [0.005N HNO₃]:[GPTMS]:[TB]=2:1:1 sol in Figure 5-31 confirmed the existence of carbons from GPTMS and methanol indicated by a wedge as well. Integration of peak does not necessarily match the number of moles of corresponding atom in ¹³C-NMR ⁵².

¹H-NMR was not used for this mixture of sol because there were too many peaks in the spectrum that overlapped each other to identify.

Shift of peaks to low field was observed when HNO_3 was added to the sol for both of ^{13}C - and ^1H -NMR. It is accounted for by the formation of hydrogen bonding between the corresponding atom and the water molecule because hydrogen bond is regarded as being electron-attractive^{52, 54-55}. This phenomenon is clearly found for the peaks of carbon e and g in Figure 5-16 and regime A in Figure 5-19.

Conclusion

The hypothesized chemical reactions described in Figure 5-17 and Figure 5-30 were confirmed by analysis on NMR results. TB is not readily hydrolyzed even with the significant amount of water because water was consumed to hydrolyze GPTMS before TB was added. At a longer time scale, TB reacts with hydrolyzed GPTMS to form the Si-O-Ti bond via the condensation reaction, which explains the higher temperature for formation of the anatase phase in TiO_2 - SiO_2 composite material⁷² than that of pure TiO_2 in the result of following XRD study, and formation of 1-butanol as a byproduct. The sol gels at a much slower rate than the gelation of the organic solvent-based sols towards TiO_2 ⁵ probably due to the steric hindrance of the 3-glycidoxypropyl group of hydrolyzed GPTMS⁷³.

Microstructure of Electrospun Ceramic Fibers

Results and Discussion

TiO_2

The behavior of the phase transformation of electrospun TiO_2 fibers was studied by XRD and TEM. The results are presented in Figure 5-32 and Figure 5-33.

In the XRD spectra, peaks noted as A and R are assigned to the anatase and the rutile phase, respectively. TiO_2 samples that were heat-treated at 500°C and 600°C were found out to be mainly the anatase phase without any rutile peaks observed. The

rutile phase appeared in TiO₂ heat-treated at 700°C along with the anatase and both phase coexisted in TiO₂ heat-treated at 800°C. After heat treatment at 900°C, the rutile became the dominant phase while peaks of the anatase were barely observed. The phase transformation of TiO₂ by the heat treatment temperature is as reported by researchers^{5, 48-49, 67, 74}. The grain size for both of the anatase and the rutile phase was calculated by equation 4-6 based on peaks in Figure 5-32 and the result is shown in Table 5-8. Two peaks with the highest intensity were selected to be analyzed for both phases, which are peaks at 25° and 48° of 2θ for the anatase and peaks at 27° and 54° of 2θ for the rutile phase. 25° and 48° of 2θ are (101) and (200) planes of the anatase while 27° and 54° of 2θ are (110) and (211) planes for the rutile, respectively. Grains kept growing as the heat treatment temperature increases as long as peaks of the phase could be observed as reported by Avci et al.⁴⁷. It is thermodynamically preferred because, with the grain size increased, the total surface energy decreases due to the smaller specific area of the grain boundary. At the higher temperature, it could be achieved easier with the higher mobility of atoms that results in the grain growth.

TEM images in Figure 5-33 show the morphology of grains of electrospun TiO₂ fibers after the heat treatment for 3 hours at 500, 600, 700, 800, 900°C from (A) to (E). When compared to XRD results, grains of the 500, 600°C-heat-treated samples shown in Figure 5-33 (A) and (B), respectively, are the anatase while the rutile phase was developed in the 700°C-heat-treated sample. The grain size of the rutile phase increases with the higher heat treatment temperature and the morphology changes as well from the roughly spherical shape to the columnar shape. For the rutile fibers in Figure 5-33 (E), the fibers are formed by the link of single grains. Thickness fringes are

also observed in some crystallites due to the gradual thinning of the grain in the direction of the incidental beam towards the grain boundary ⁷⁵. The grain size of the anatase observed as around 20 to 30 nm is comparable to data presented in Table 5-8 while the grain sizes of the rutile phase don't match well. The calculated grain size for the rutile phase by the Scherrer's equation (equation 4-6) is 43 nm for the 900°C-heat-treated sample instead of diameters around 100 nm and lengths of up to around 250 nm that the columnar shaped-grains have in the Figure 5-33 (E). In spite that the number of observation is small to be statistically meaningful, the gap between the calculation and observation is 133% at least which could be regarded as a large error. The error could be ascribed to the limitation of the Scherrer's equation that is dependable in calculation of smaller spherical crystallites than 100 nm in diameter ^{57-58, 76}. In regard with the fiber morphology, cleavages between the grains of the anatase phase and coarse structure formed by grains was observed in the 500, 600°C-heat-treated samples. When fibers with these morphologies are loaded with external stress, it is focused on the apex of the cleavage to initiate cracks while the coarse structure would ease the propagation of the crack. The fiber structure became significantly denser with the development of the larger grains of the rutile phases which allowed less space between grains. The fiber diameter should be reduced as the heat treatment temperature increases because of formation of the denser structure in the fiber as well as the higher density of the rutile than that of the anatase phase, 4.13 and 3.79, respectively ⁷⁷. Nonetheless, fiber diameters were not observed to be decreased drastically probably because the number of observation was not many enough to be statistically meaningful to exhibit the differences.

TiO₂-SiO₂ from Aqueous Sol

In the XRD diagram in Figure 5-34, 500°C-heat-treated sample showed a broad peak over early 20° of 2θ while the 800°C-heat-treated sample and the 1100°C-heat-treated sample showed weak peaks and well-defined peaks, respectively, with the slight increase in the intensity of the broad peak compared to the baseline. If TiO₂ was being separated as the amorphous phase in SiO₂ matrix at the 500°C-heat-treated sample, the intensity of the broad peak over 25° of 2θ should be decreased significantly as TiO₂ got crystallized because of;

- Overlapped peak position of amorphous TiO₂ broadly at around 25° and 30° of 2θ⁷⁸ with amorphous SiO₂⁷⁹⁻⁸¹.
- The indicative amount of TiO₂ to SiO₂ in molar ratio of 5:12 according to the recipe of the sol described in sol preparation of TiO₂-SiO₂ from aqueous sol.

The precursor of Ti was TB while those of Si were GPTMS and TEOS. Therefore, based on the characteristics of XRD peaks with varying temperatures of heat treatments, it is hypothesized that Ti atoms were dispersed in the SiO₂-dominant matrix to form Si-O-Ti bonds for the 500°C-heat-treated sample and separated to be crystallized to the anatase phase at the higher temperature, 1100°C as indicated by wedges. The intensity increment of the amorphous SiO₂ peak from 800°C- to 1100°C-heat-treated samples is accredited to the newly formed SiO₂ phase by Si atoms that were incorporated in Si-O-Ti structure in the 500°C-heat-treated sample. It is also found that the crystallization temperature for the anatase TiO₂ is between 800 and 1100°C which is higher than 500°C, usual temperature for the formation of the anatase phase from TiO₂ precursor sol without SiO₂ precursor^{5, 47-49}. The increase of the crystallization temperature of TiO₂ has been observed in TiO₂-SiO₂ system before^{79, 82} and is reported that the Si-O-Ti bond hinders the formation of the TiO₂ phase while the Ti-O-Ti bonds

and the Si-O-Si bonds become more stable at the higher temperature that leads the phase separation of TiO_2 and SiO_2 ^{72, 83}, which explains the XRD result as well. The formation of the Si-O-Ti bond was as hypothesized in Figure 5-30 and evaluated in the NMR study in the previous chapter. The grain size of the anatase TiO_2 phase in the 1100°C-heat-treated sample was calculated to be 10 nm by equation 4-6. Two peaks with strongest intensity at 25° and 48° of 2 θ were selected to be analyzed for calculation of the grain size by the Scherrer's equation. Peaks at 25° and 48° of 2 θ represent (101) and (200) planes of the anatase phase, respectively.

TEM images of electrospun TiO_2 - SiO_2 composite fibers after the heat treatment at 500, 800, 1100°C for 3 hours are presented in Figure 5-35 (A, B, C), respectively. It was observed that the phase development of TiO_2 in the fiber through the different heat treatment temperature was in an agreement with the result of XRD analysis. When the fiber was heat-treated at 500°C, it was homogeneously amorphous with smooth surface, no grains or crystalline plane observed (Figure 5-35 (A)). After the heat treatment at 800°C, dots estimated to be about 2~3 nm in diameter were appeared in Figure 5-35 (B). These are regarded as grains of TiO_2 by XRD result showing small hump at 25° and 48° of 2 θ (Figure 5-34). When the fractured end of the fiber was observed, it was found to be the cross-section of the fiber because of the contrast gradation. The grains of TiO_2 were observed over the whole regime of graded contrast which means anatase crystallites were developed not only on the surface but well dispersed through the fiber. And TiO_2 phases observed as dark spheres, which are the anatase phase according to the XRD result, are clearly developed after the heat treatment at 1100°C. In comparison with the TEM image of the anatase fibers (Figure 5-

33 (A, B)), TiO_2 - SiO_2 composite fibers with the anatase TiO_2 have a dense structure without any pores regardless of the heat treatment temperature, as reported⁸³, probably because the amorphous SiO_2 with the high mobility at the elevated temperature was transported to fill up the space created by the grain growth. The grain size is estimated to be around 10 nm. It also corresponds well to 10 nm, which is calculated by the Scherrer's equation from the XRD result.

Electrospun TiO_2 - SiO_2 fibers from the half sol A have been characterized by SEM and XRD. The half sol was attempted to electrospin the composite fiber with higher TiO_2 loading to SiO_2 at 50%-50% compared to 29%-71% of the full aqueous sol. Fibers made of the composite material with the anatase TiO_2 were successfully electrospun as observed in Figure 5-36 and Figure 5-37. Nonetheless, the high viscosity due to the higher TB ratio retards the thinning of fibers in the electrospinning process that leads to the formation of microfibers. However, when compared to TiO_2 29%- SiO_2 71% fibers (Figure 5-10, Figure 5-35 (C)), the crystallization growth of the anatase on the surface of TiO_2 50%- SiO_2 50% fibers along with the unique needle-like crystal growth were clearly distinguishable at lower magnification of SEM (Figure 5-36). It is attributed to the relative abundance of TiO_2 that contributes the grain growth. The needle-like crystal growth of the anatase TiO_2 from the fiber was observed in about 5% of images taken on randomly selected area over the sample by SEM. The grain size calculated by the Scherrer's equation on peaks at 25° and 48° of 2θ in Figure 5-37 was 18 nm. Although the measured crystallite size was not confirmed by high-resolution TEM images, bright grains observed on the surface of the fiber in Figure 5-36 (A) have diameter of roughly 25 nm. Provided that it was estimated based on a low-resolution SEM image, the 7 nm-

difference is ignorable. Based on the observation, the reason that needle-like large crystallites grown from fibers didn't affect the XRD result is attributed to their limited amount with that morphology.

Conclusion

Behavior of phase transformation and crystallization was investigated on TiO_2 and TiO_2 - SiO_2 composite fibers. In regard with TiO_2 from the EtOH-based sol, the pure anatase phase was developed via the heat treatment at 500°C for 3 hours. As the heat treatment temperature increases, the rutile phase was developed and prevailed via the heat treatment at 900°C for 3 hours. In regard with TiO_2 - SiO_2 composite fibers, the anatase was formed after the heat treatment for 3 hours at the temperature higher than 800°C which is at least 300°C higher than crystallization temperature for the anatase from TiO_2 of the EtOH-based sol. When Ti atoms were incorporated in the SiO_2 matrix, the Si-O-Ti bond is preferably formed so that the formation of the Ti-O-Ti bond gets hindered at 500°C . At higher temperature—i.e. 1100°C — TiO_2 phase is separated to form the anatase phase from the SiO_2 phase because the Ti-O-Ti bonds and the Si-O-Si bonds become more stable. TiO_2 - SiO_2 fibers established the denser microstructure than pure TiO_2 fibers because of the amorphous SiO_2 phase to form the continuous phase in the composite material.

Discussions

In the electrospinning process, the fiber diameter could be controlled by varying concentration of polymers that promotes spinning of continuous fibers by the chain entanglement. More importantly, C_v s of all electrospun fibers of PAN, TiO_2 and TiO_2 - SiO_2 composite material were suppressed below 0.3 which is less than half of fibers that compose the commercial HEPA filters (Figure 5-7 (B)). C_v of fibers is a substantial

factor in the quality control on the fabrication because fibers with the larger fiber distribution, i.e. larger C_v , have the smaller specific surface area than those with smaller C_v . Material system with the smaller specific surface area discourages all the surface-driven functionality including the filtration, the photocatalytic activity, the microwave absorption, etc. Furthermore, when the fibers have larger C_v , the pressure drop will increase because the drag force is exponentially proportional to the fiber diameter as shown in equation 2-6, equation 2-4. Therefore, in order to fabricate filtration media with a high quality factor, accomplishing low C_v in the fiber diameter of filtration media is of paramount importance.

Electrospun PAN nanofibermats with d_f of 224 nm showed promising results in the filtration tests as enhanced filtration media. PAN fibermats achieved the quality factor over twice higher than LydAir HEPA filters that are currently used by U.S. Army, and over three times higher than the criteria by the Department of Defense⁵¹. If the electrospun $\text{TiO}_2\text{-SiO}_2$ composite fiber with the anatase phase was used instead of the PAN fiber, 13% increase in the drag force is anticipated based on the calculation with equation 2-6 and equation 2-4. Compared to 221% increase in the drag force that is expected with LydAir HEPA with d_f of 527 nm, it could be considered as a slight increase. Since the relationship between the pressure drop and the drag force heavily depends on empirical conditions, it cannot be concluded that the pressure drop will increase 13% and 221% for $\text{TiO}_2\text{-SiO}_2$ composite fibers and HEPA filter fibers. However, because it is obvious that a weak drag force causes a low pressure drop, $\text{TiO}_2\text{-SiO}_2$ composite fibers will have a lower pressure drop than HEPA filter fibers.

Also for the additional functionality as a microwave-absorbing material or a photocatalytic material, electrospun TiO_2 , especially anatase-based nanofibers have advantages. As the fiber diameter decreases,

- Distance of diffusion for excited electrons by photons becomes shorter to reduce the probability of recombination with holes.
- The specific surface area increases to induce more contact with reactant chemicals or electromagnetic wave.

Towards the TiO_2 -based materials via the sol-gel method, due to the high reactivity to water molecules, it has been presumed to be very difficult to handle transition metal alkoxides without strict control of moisture in order to achieve homogeneous sols or gels⁴. As the result, enormous amount of organic chemicals has been disposed after processing. For the first time at the best knowledge, control on the reaction rate of metal alkoxides and water molecules was demonstrated by adopting GPTMS as the control agent. With dominant amount of water, i.e. 93% in molar ratio, TB and TEOS were stabilized to keep the transparent homogeneous sol. Adopting the aqueous sol to produce metal oxide materials is expected to decrease the harm to environment as well as the cost in disposal of toxic organic chemicals. In order to acquire the homogeneous aqueous sol with other transition metal alkoxides, the mechanism between chemicals should be discerned. In this dissertation, the chemical reaction mechanism of half sol A was explained by analyzing results from ^1H - and ^{13}C -NMR. Although there are more to explore to fully understand the aqueous sol system, the result presented here would be the least clue to navigate the direction in the design of experiments.

In terms of the microstructure of anatase TiO_2 - SiO_2 composite fiber, smooth fibers with the dense structure were achieved in TiO_2 - SiO_2 fiber compared to anatase TiO_2

fiber that has cleavages at exposed grain boundaries on the surface. These cleavages are where the cracks are formed by concentrated stress to result in failure of the fiber. When the external stress is applied on the smoother surface of the fiber, the stress is more evenly distributed and the threshold value of the stress to initiate a crack becomes higher which results in mechanically stable fibers. The continuous phase of amorphous SiO_2 could also block the propagation of the crack from inside of the anatase grains. Furthermore, in the SEM observation, TiO_2 - SiO_2 composite fibers were bonded to each other to form the network due to the low vapor pressure of the solvent, i.e. water in the aqueous sol. The fused network would enhance the mechanical stability of fibers as well because the external force would be distributed over the network while the force is concentrated onto the limited number of fibers to result in failure of those fibers. Consequently, better mechanical stability is anticipated for TiO_2 - SiO_2 composite fibers than TiO_2 fibers. Among TiO_2 - SiO_2 composite fibers, the 1100°C-heat-treated fiber had the roughest surface due to the anatase crystallites formed on the surface compared to other fibers heat-treated at lower temperature which kept the amorphous phase or smaller grains. In spite of the rough surface that would induce the inferior mechanical stability, however, fibers of anatase TiO_2 - SiO_2 phase are still preferred because of versatility of the anatase, e.g. the microwave absorption, the photocatalytic effect. These functionalities could be of utmost importance in future applications, e.g. the regeneration of filtration media by the microwave absorption, chemically active filtration media with the photocatalytic effect.

Table 5-1. Result of analysis on fiber diameter of PAN and TiO₂.

Material	PAN	TiO ₂	
Polymer concentration w/v DMF/EtOH	6%	PVP 4%	PVP 16%
Heat treatment	N/A	500°C	500°C
d _f	224	149	1110
C _v	0.25	0.24	0.20

Table 5-2. Result of analysis on fiber diameter of TiO₂-SiO₂.

Material	TiO ₂ -SiO ₂							
Polymer concentration w/v sol	PVP 1%				PVP 2%			
Heat treatment	as-spun	500°C	800°C	1100°C	as-spun	500°C	800°C	1100°C
d _f	444	228	221	243	953	361	336	375
C _v	0.29	0.27	0.25	0.29	0.22	0.18	0.20	0.23

Table 5-3. Results of filtration tests^{36, 51}. PAN (a)×(b) means (b) layers of PAN fiber mat fabricated by (a)-minute deposition via electrospinning. If (b) is unspecified, it's a single layer sample.

Filter	P	Δp (Pa)
ACF×2	8.66±0.37×10 ⁻¹	21
Millipore HEPA	7.94±3.71×10 ⁻⁴	1171
LydAir HEPA	1.35±4.35×10 ⁻⁴	284
PAN 5	3.67±0.07×10 ⁻¹	18
PAN 15	1.03±0.19×10 ⁻¹	98
PAN 5×3	6.54±0.16×10 ⁻²	41
PAN 15×2	2.25±0.78×10 ⁻²	152
Military standard	3×10 ⁻⁴	400

Table 5-4. Values of electronegativity of atomic species in GPTMS⁵³.

Atom	Electronegativity
H	2.2
C	2.5
O	3.5
Si	1.7

Table 5-5. Integration of block A, B and C (Figure 5-21, Figure 5-22, Figure 5-23 and Figure 5-24).

[0.005N HNO ₃]:[GPTMS]	A	B	C
1:1	0.97	4.00	1.00
2:1	2.03	7.16	1.00
4:1	5.68	10.37	1.00
8:1	12.88	10.85	1.00

Table 5-6. Calculated [MeOH] and [H₂O] based on values in Table 5-5, and experimental errors of [MeOH]+[H₂O].

[0.005N HNO ₃]:[GPTMS]	[MeOH]	[H ₂ O]	[MeOH]+[H ₂ O]		Error
			Experiment	Theory	
1:1	1.00	-0.02	0.98	1	2%
2:1	2.05	-0.01	2.04	2	2%
4:1	3.13	1.27	4.40	4	10%
8:1	3.28	4.80	8.08	8	1%

Table 5-7. Time required for gelation of sol of [0.005N HNO₃]:[GPTMS]:[metal alkoxide]=2:1:x before gelation or precipitation. Precipitated sols are indicated as (p).

[Metal alkoxide] X	Time taken before Gelation/Precipitation			
	TB	TiPP	ZP	ZB
0.125	6-24 hours	6-24 hours	24 hours	2-18 hours
0.25	<4 hours	6-24 hours	2-18 hours	2-18 hours
0.5	16-20 hours	<3 hours	2-18 hours	<1 hour
1	4 weeks	4 days	<1 hour	2-18 hours
2	4 months	5 months	3 days	3 days
4	3.5 months	3 days (p)	10 days	20 hours (p)

Table 5-8. Grain size of different TiO₂ phases calculated by Scherrer's equation on spectra shown in Figure 5-32. N/A means that the peaks were too weak to be analyzed.

	Heat treatment temperature (°C) for 3 hours				
	500	600	700	800	900
anatase (nm)	16	22	28	34	N/A
rutile (nm)	N/A	N/A	35	40	43

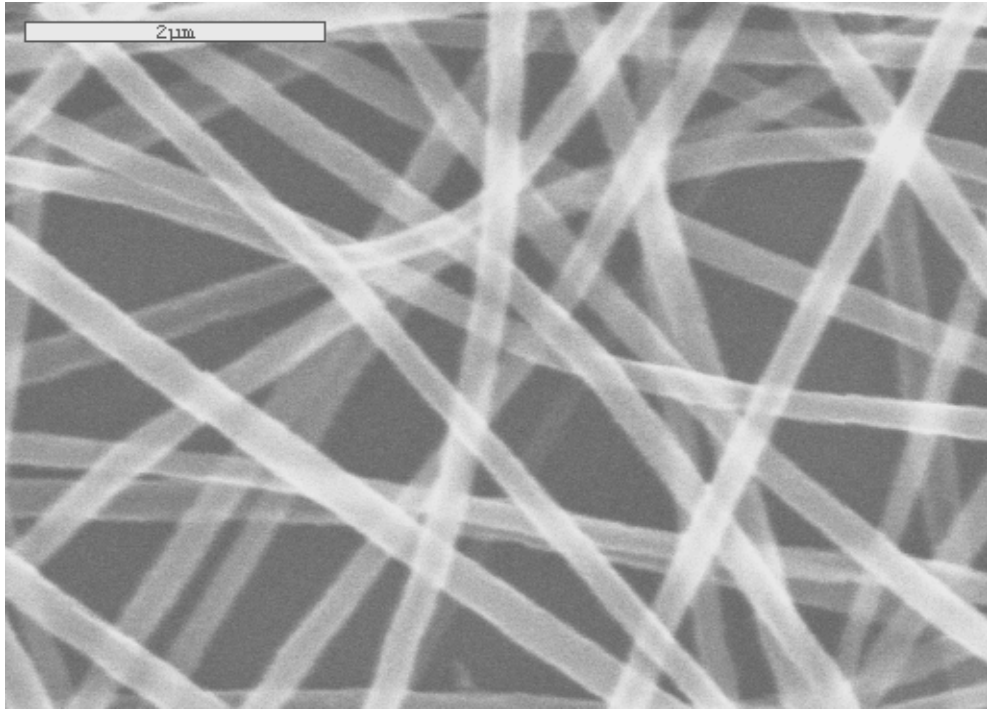


Figure 5-1. An SEM image of electrospun PAN fibers from PAN 6% w/v DMF.

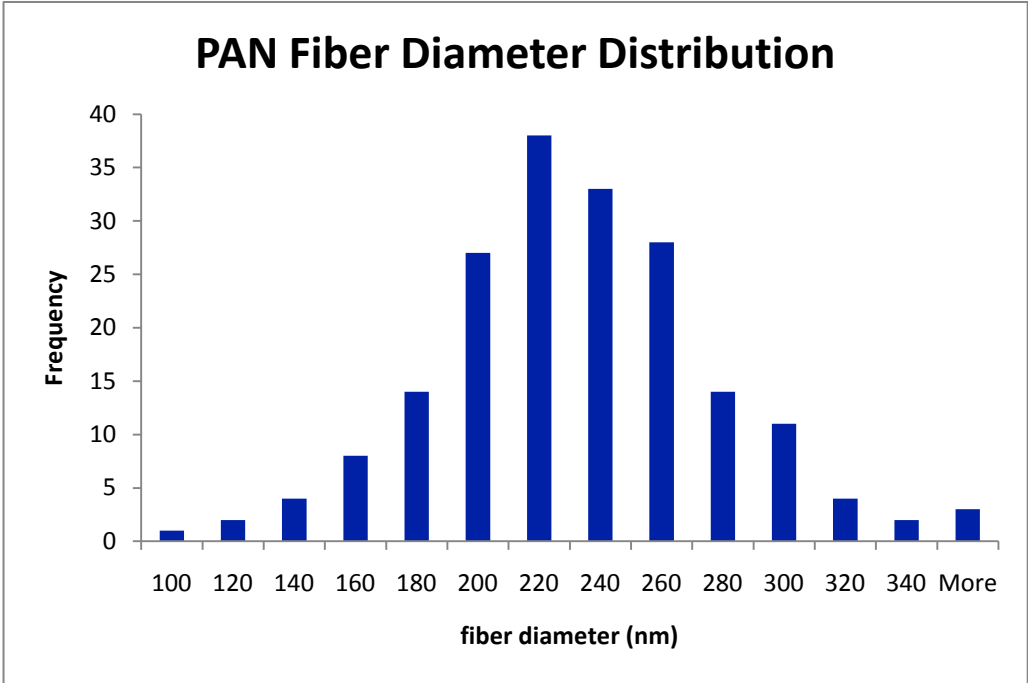


Figure 5-2. Fiber diameter distribution of electrospun PAN fibers.

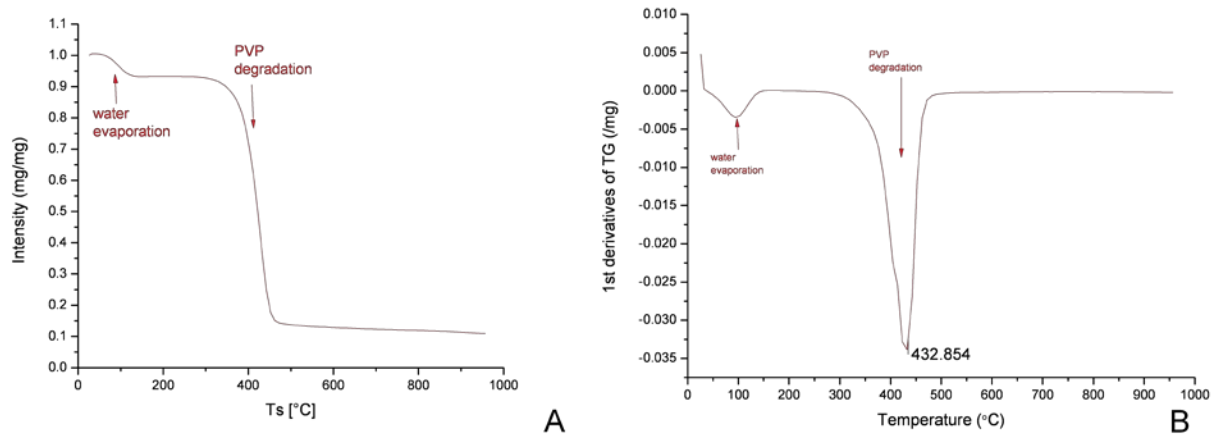


Figure 5-3. (A) Thermogravimetric analysis of poly vinyl pyrrolidone degradation, and (B) its first derivative to locate the peak. Dried air was flown to the TGA chamber at 0.04 LPM in 20 psi. Temperature was increased from the room temperature to 1000°C at 10°C/min.

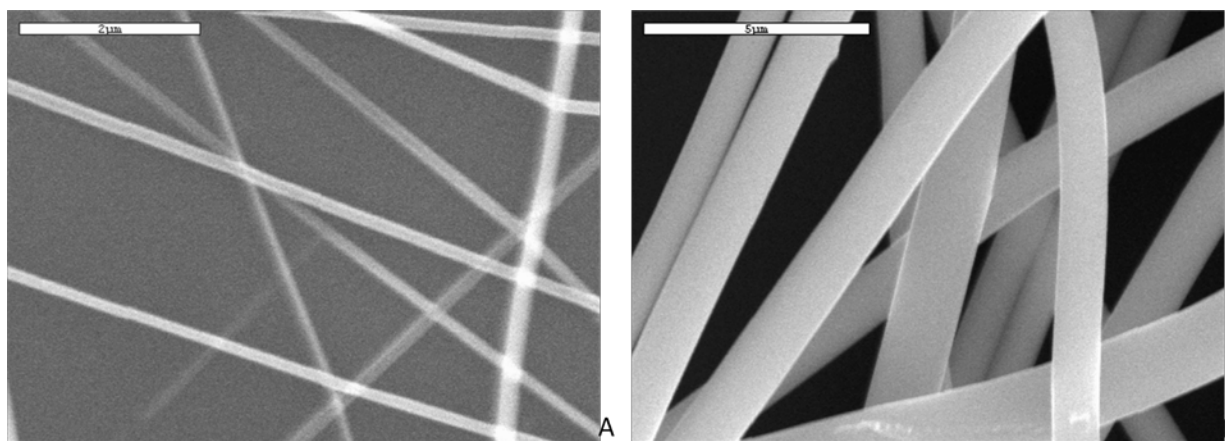


Figure 5-4. SEM images of electrospun TiO_2 fibers from (A) PVP 4% and (B) 16% w/v EtOH after heat treatment. Scale bars are (A) 2 μm and (B) 5 μm .

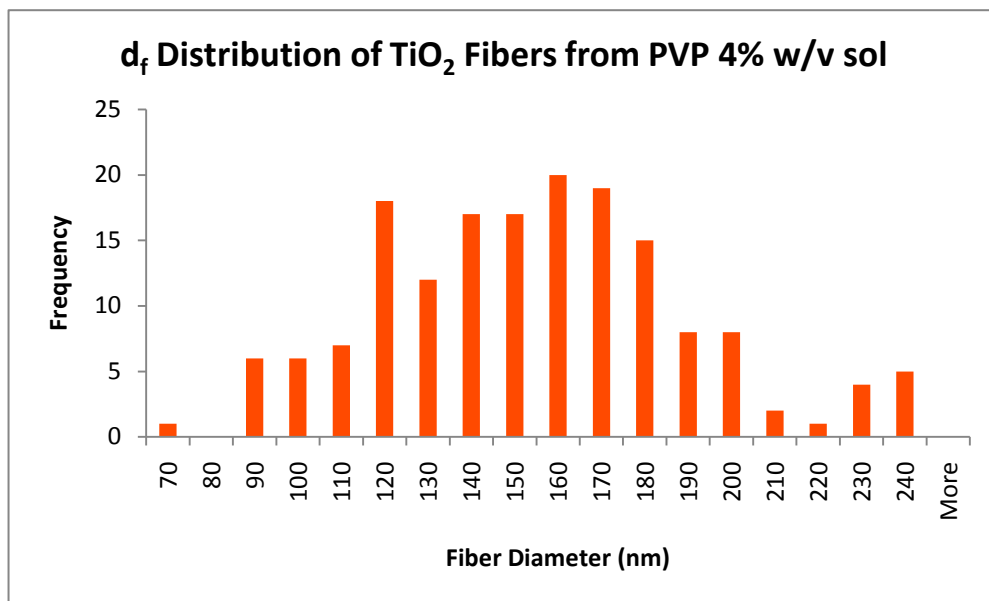


Figure 5-5. Fiber diameter distribution of electrospun TiO₂ fibers from PVP 4% w/v EtOH.

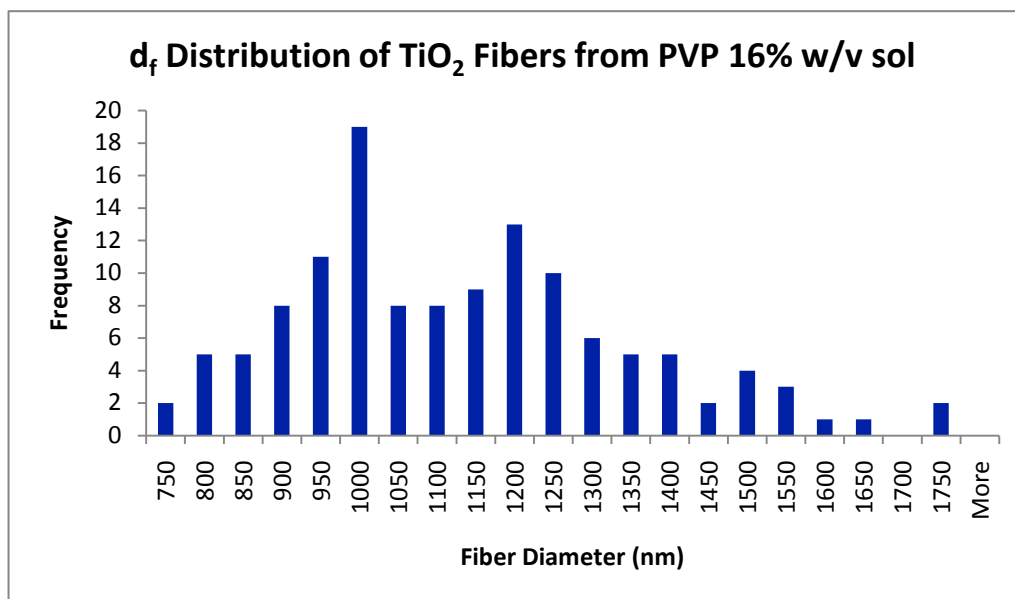


Figure 5-6. Fiber diameter distribution of electrospun TiO₂ fibers from PVP 16% w/v EtOH.

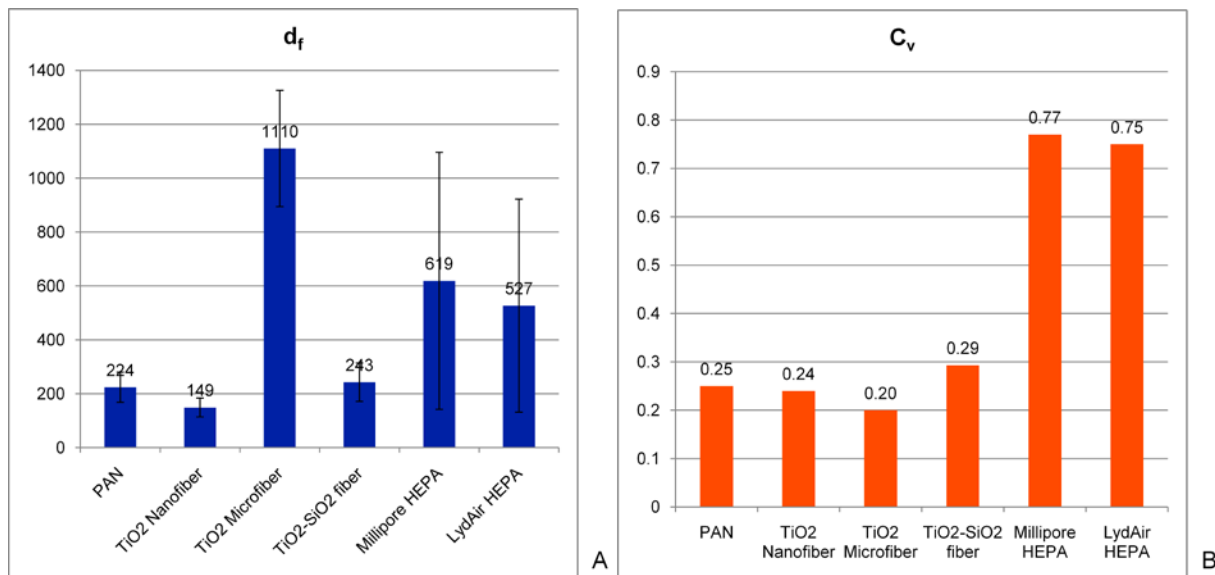


Figure 5-7. (A) d_f and, (B) C_v of as-spun PAN fiber, heat-treated TiO₂ fibers with different polymer concentration, heat-treated SiC fibers, fibers that compose Millipore HEPA and LydAir HEPA.

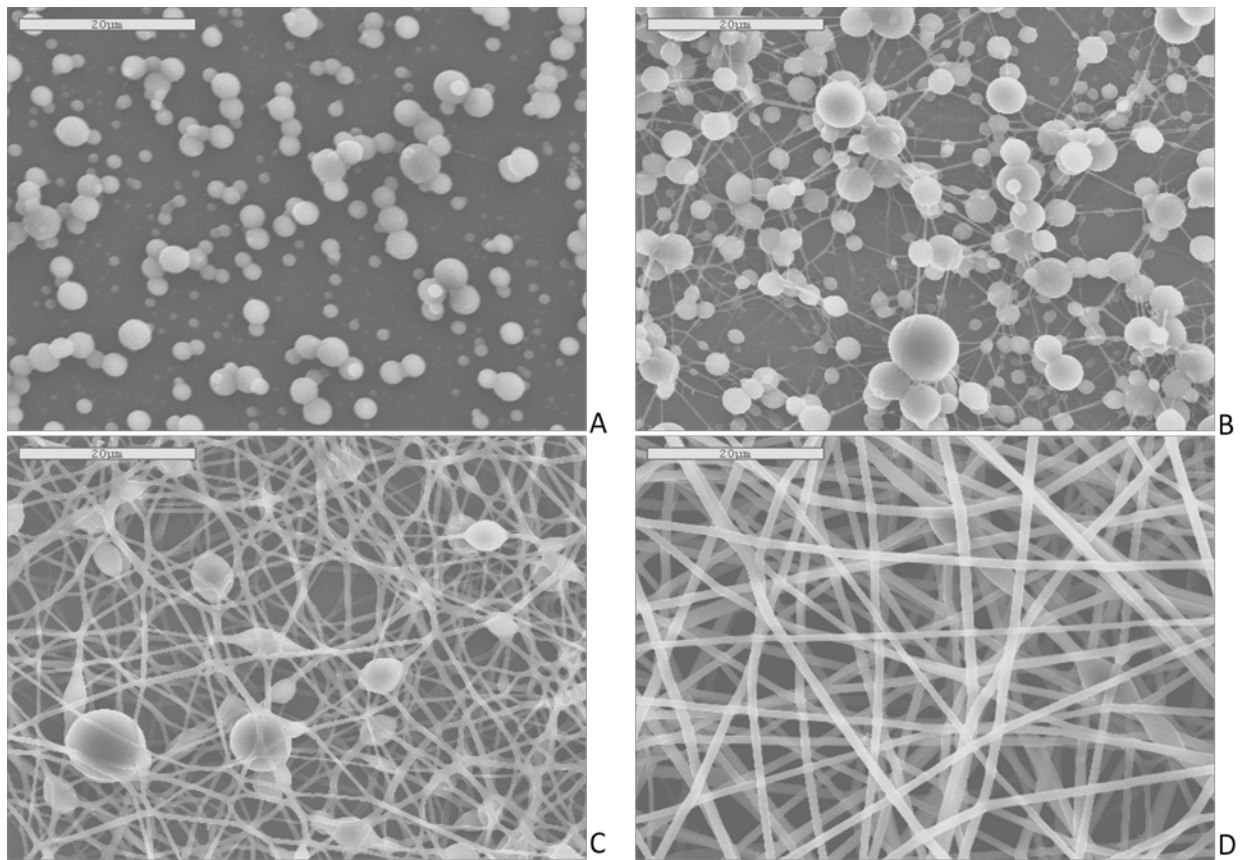


Figure 5-8. SEM images of as-spun TiO₂-SiO₂ composite fibers from aqueous sol with PVP concentration of (A) 0.25%, (B) 0.5%, (C) 1%, (D) 2% w/v sol. Scale bars are 20 μm.

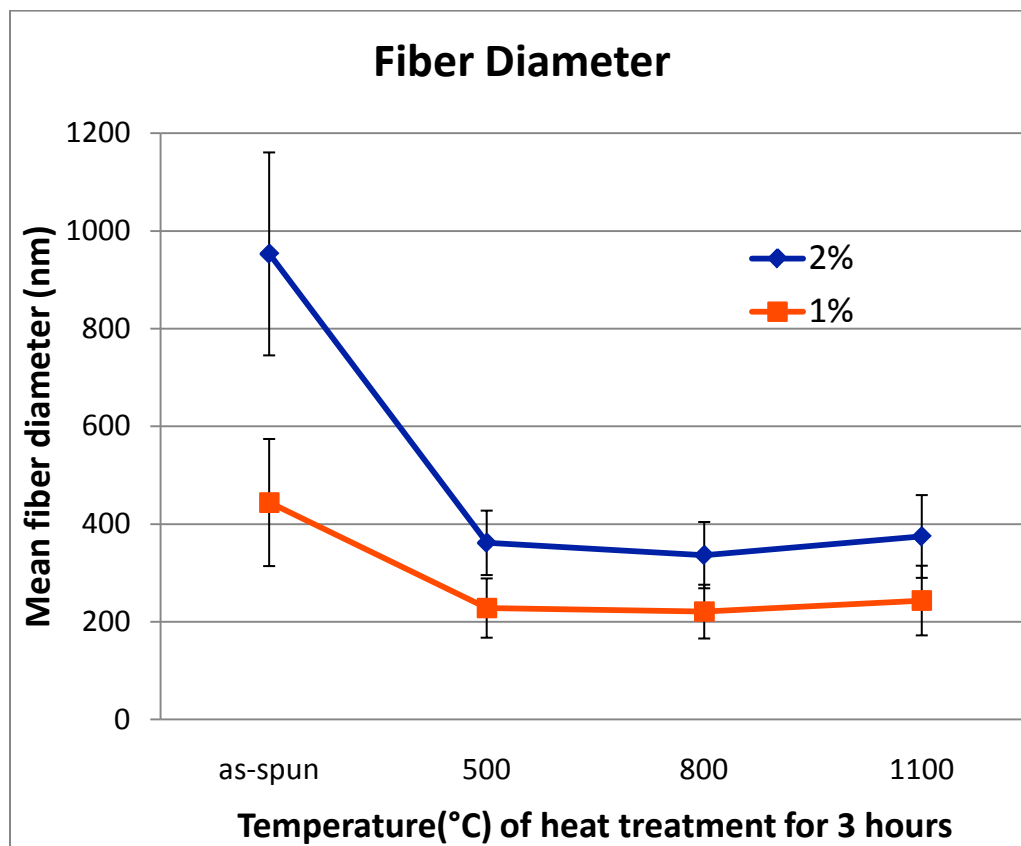


Figure 5-9. Dependence of fiber diameter for electrospun fibers of PVP 1% and 2% w/v sol on heat treatment. Connecting lines are for guidance of the eye only.

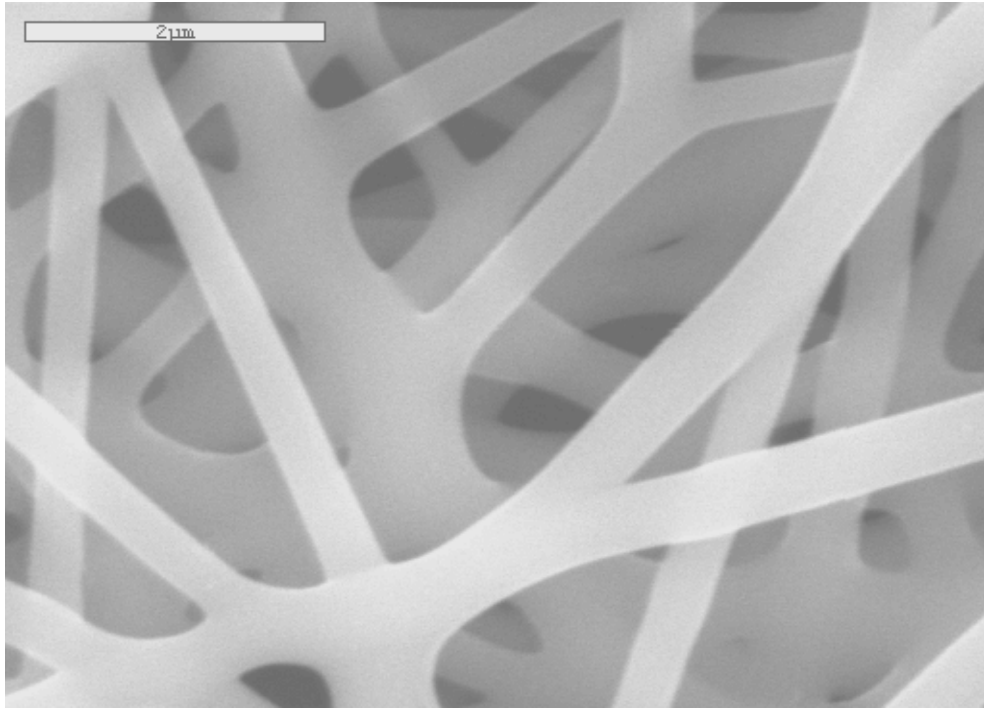


Figure 5-10. Electrospun $\text{TiO}_2\text{-SiO}_2$ composite fiber from full aqueous sol. d_f is 243 nm.

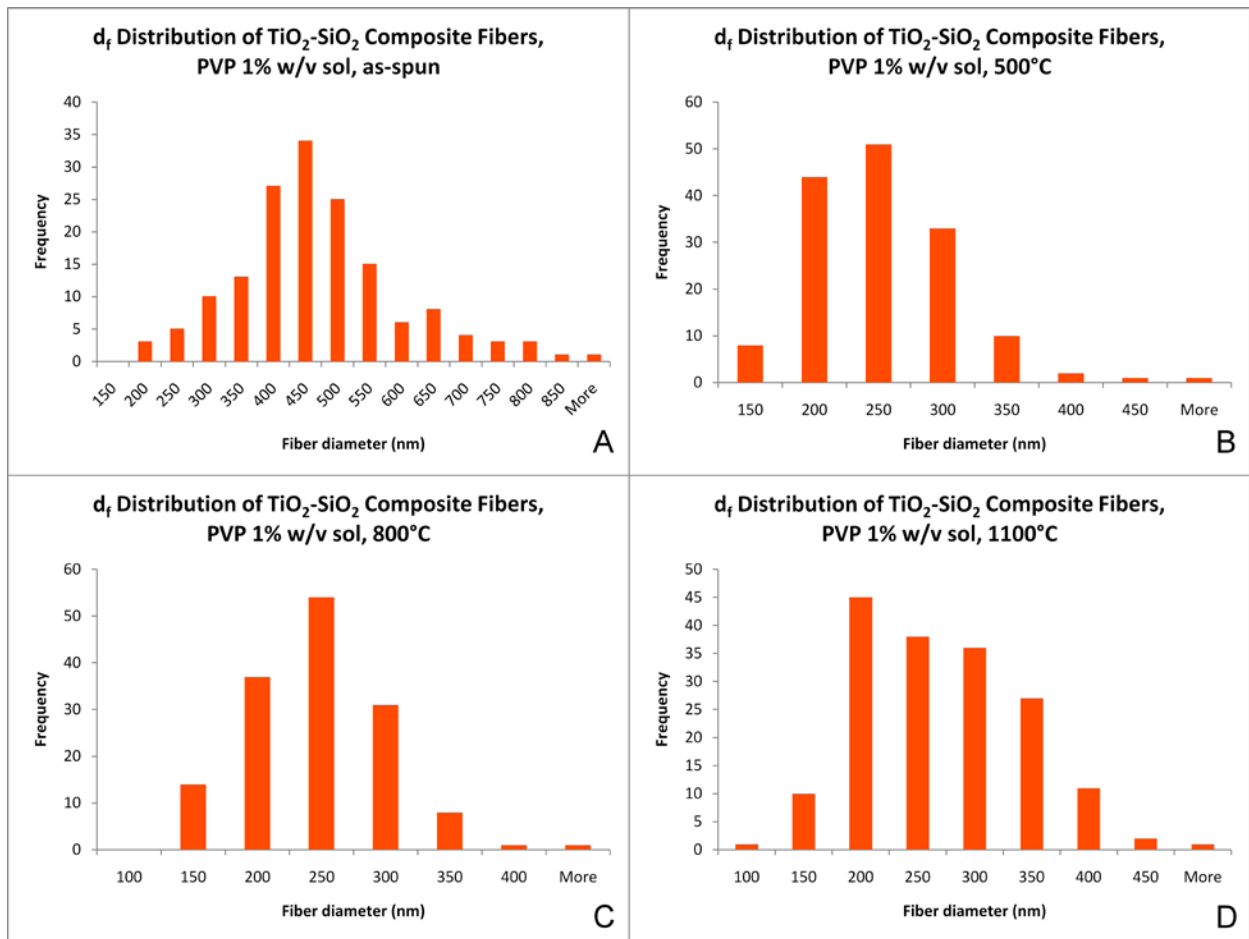


Figure 5-11. Fiber diameter distribution of electrospun $\text{TiO}_2\text{-SiO}_2$ composite fibers from PVP 1% w/v sol, depending on different heat treatment profile.

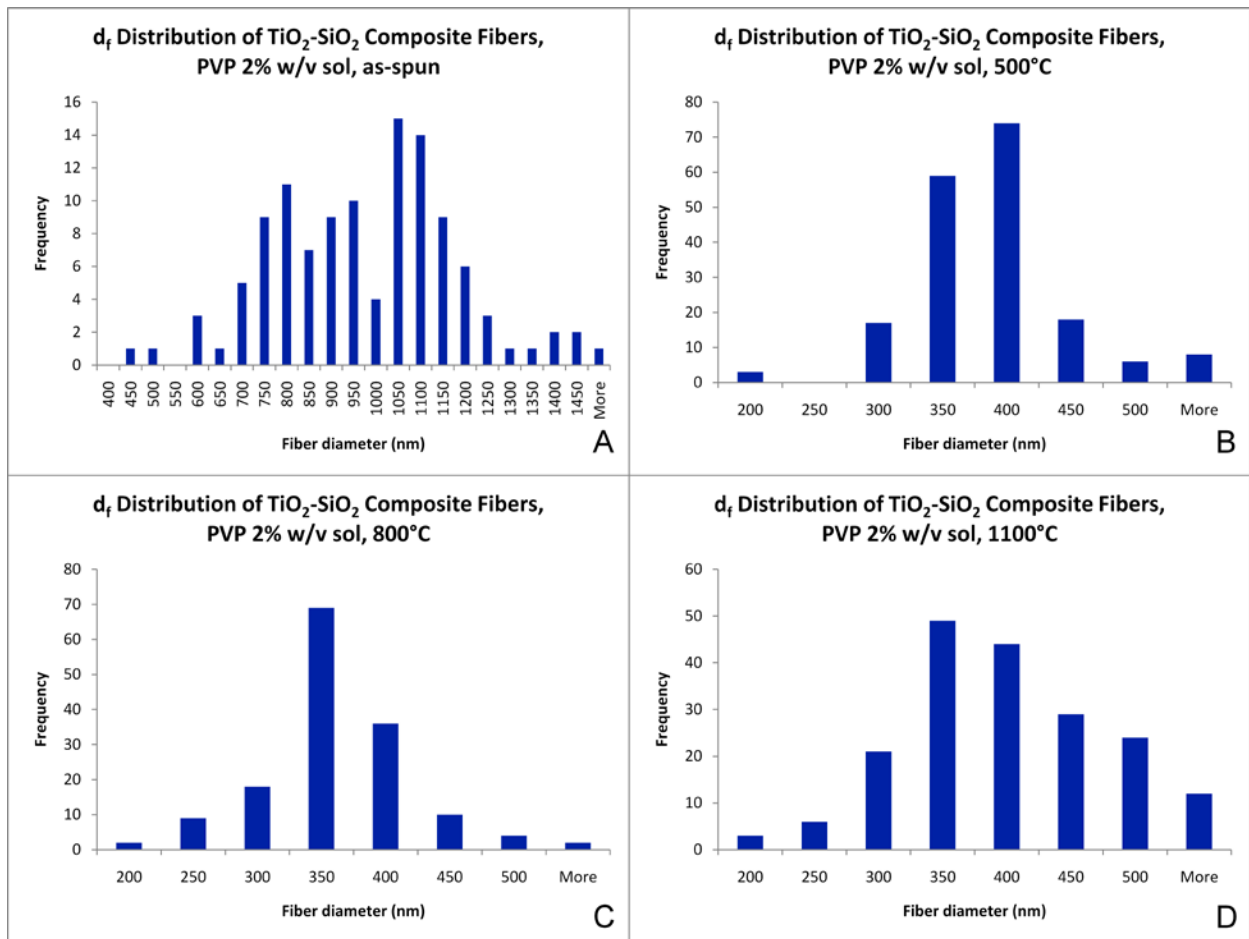


Figure 5-12. Fiber diameter distribution of electrospun $\text{TiO}_2\text{-SiO}_2$ composite fibers from PVP 2% w/v sol, depending on different heat treatment profile.

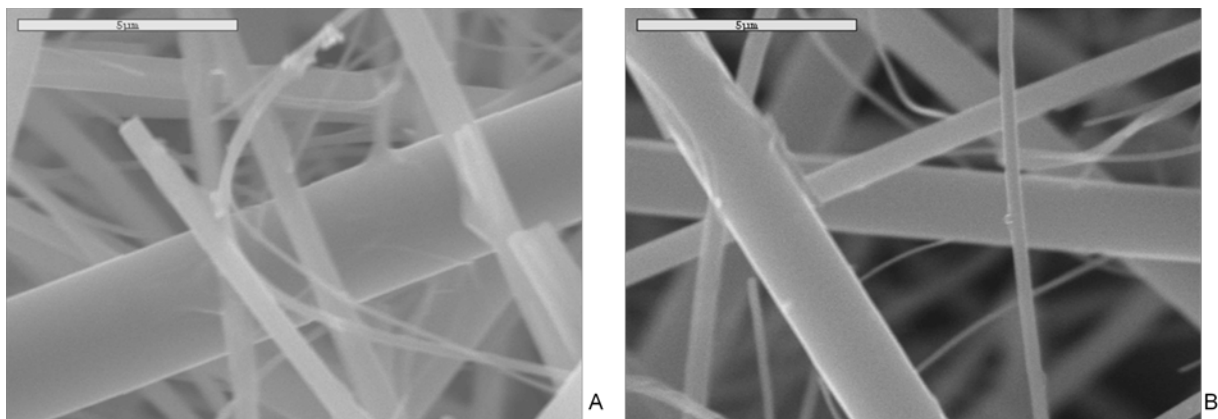


Figure 5-13. SEM images of (A) Millipore HEPA (CAT. NO.: AP1504700, Millipore, MA, USA), (B) LydAir HEPA (LydAir[®] High Alpha HEPA air filtration media-HEPA Lydair grade 4450H, Lydall Filtration, CT). Scale bars are 5 μm.

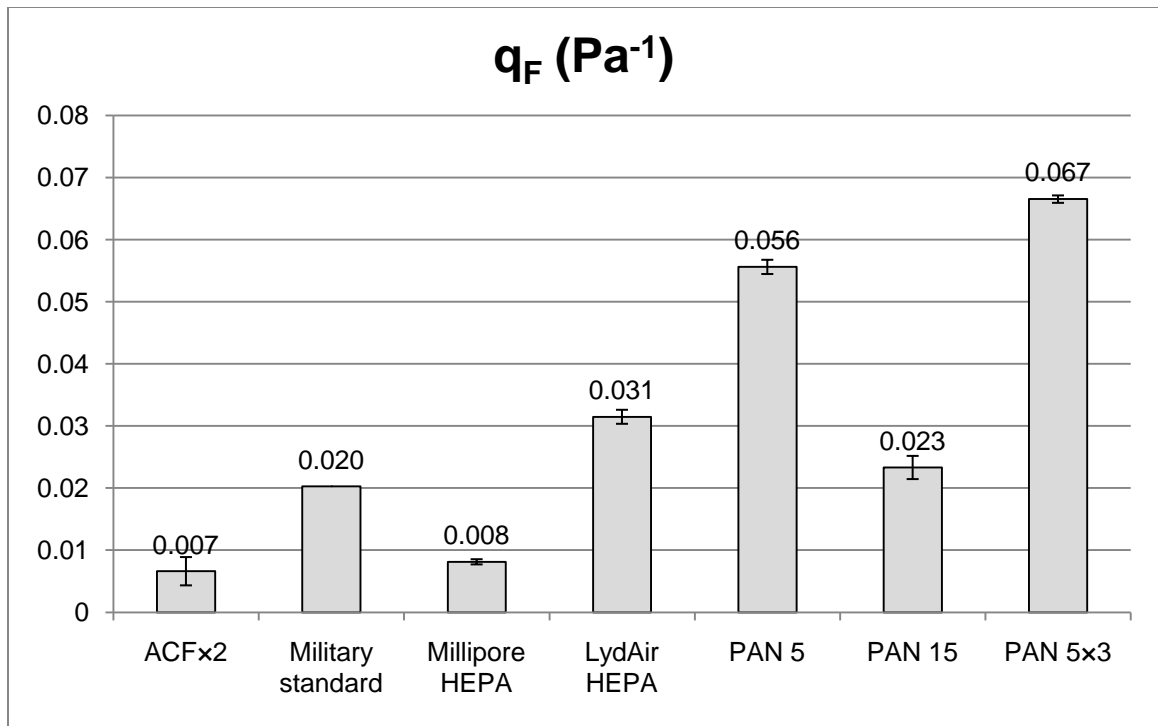


Figure 5-14. Quality factor (q_F) of filters with standard deviation calculated by data from Table 5-3.

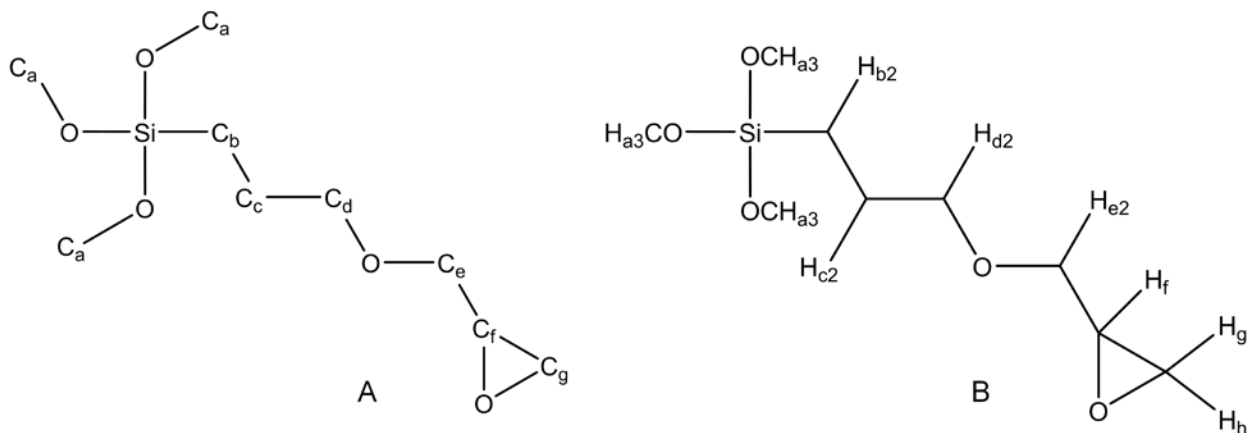


Figure 5-15. Chemical structure of GPTMS. Chemically different (A) carbon atoms and, (B) hydrogen atoms are noted by different alphabet subscripts.

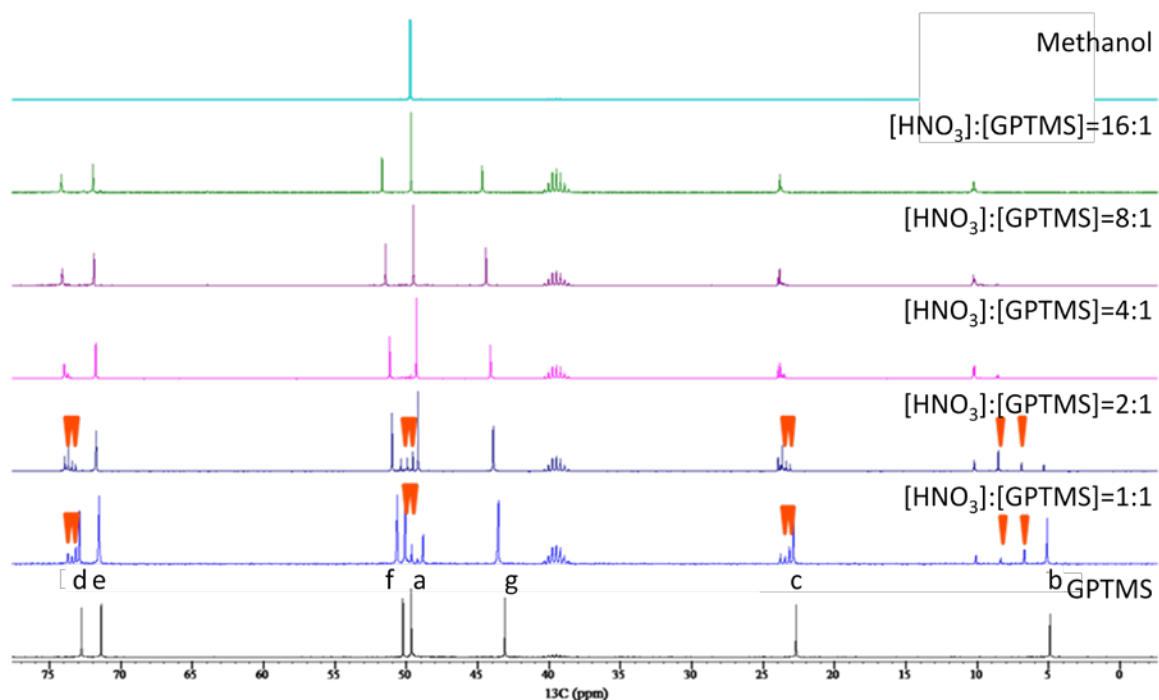


Figure 5-16. ^{13}C -NMR spectra of (from bottom to top) GPTMS, mixture of 0.005N HNO_3 and GPTMS at molar ratio of 1:1, 2:1, 4:1, 8:1, 16:1 and methanol. The wedges show the peaks from transition states. Peaks are assigned to carbons of GPTMS molecule in Figure 5-15 (A) ⁶⁹.

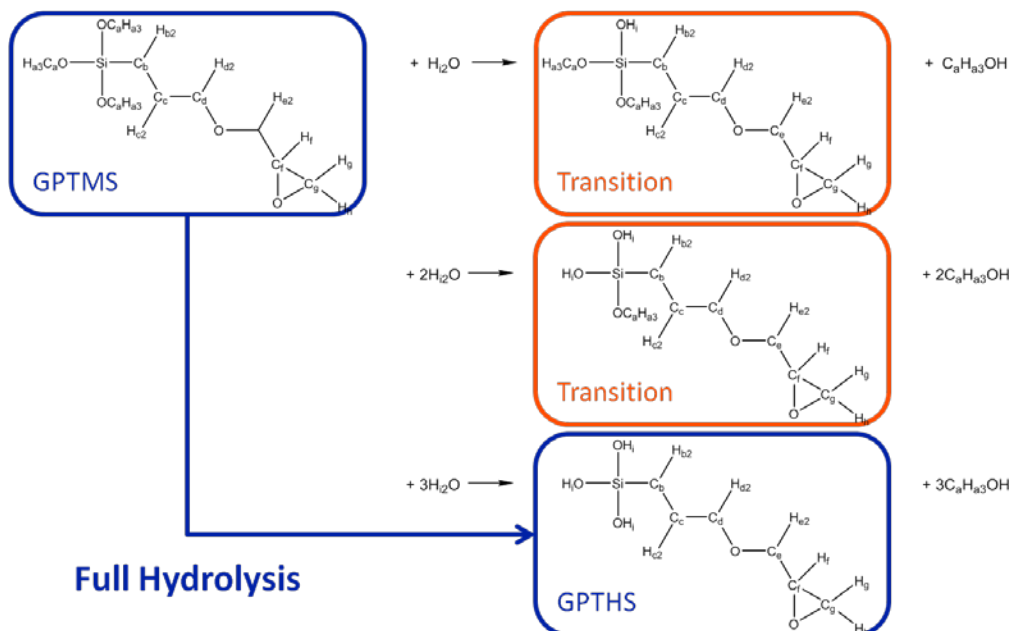


Figure 5-17. Proposed hydrolysis reaction of GPTMS in aqueous HNO_3 . Chemically different atoms are noted by different alphabetical subscripts.

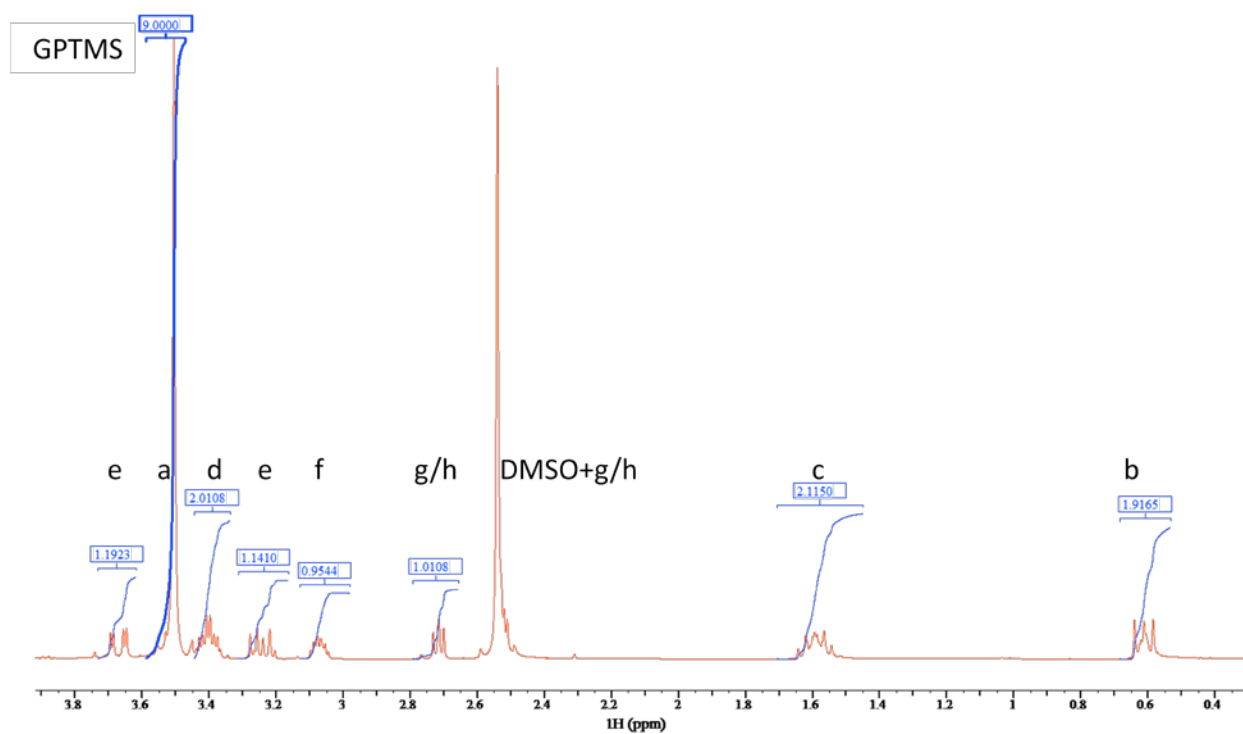


Figure 5-18. $^1\text{H-NMR}$ spectrum with peaks assigned to hydrogen atoms of GPTMS molecule in Figure 5-15 (B).

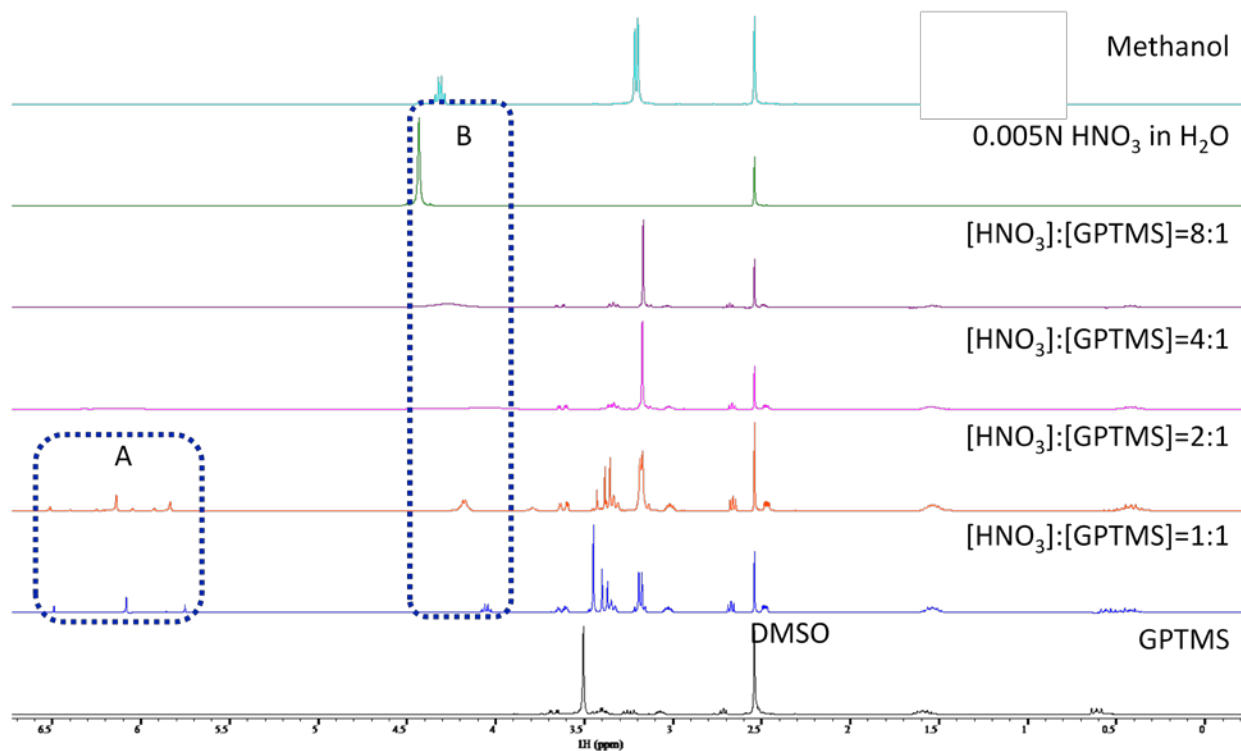


Figure 5-19. ^1H -NMR spectra of (from bottom to top) GPTMS, 0.005N HNO_3 and GPTMS at molar ratio of 1:1, 2:1, 4:1, 8:1, 0.005N HNO_3 and methanol. (A) Peaks of hydrogen atoms of hydroxyl group and, (B) overlapped peaks of water and hydrogen atom of hydroxyl group of methanol.

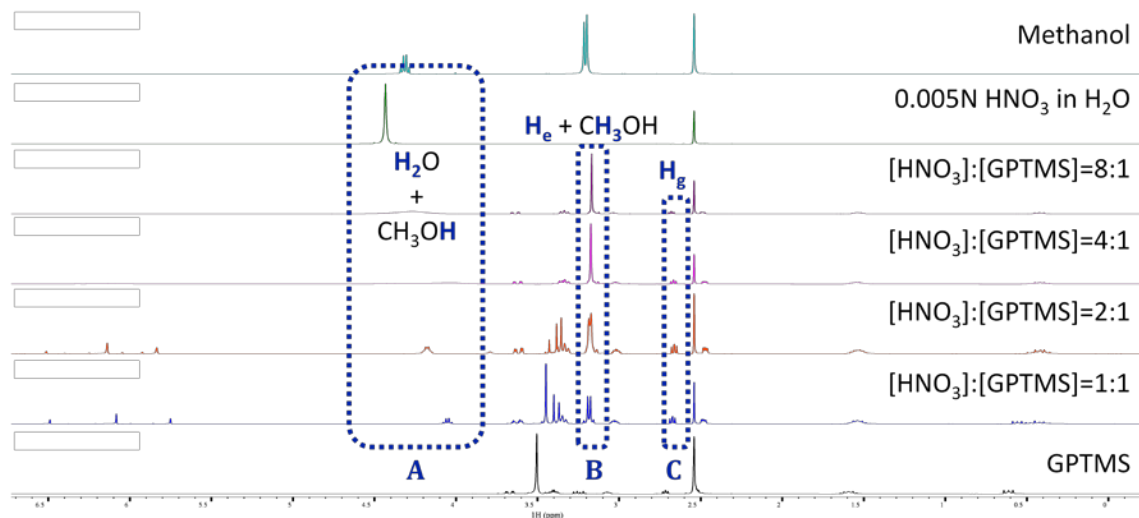


Figure 5-20. ^1H -NMR spectra of (from bottom to top) GPTMS, 0.005N HNO_3 and GPTMS at molar ratio of 1:1, 2:1, 4:1, 8:1, 0.005N HNO_3 and methanol. (A) Overlapped regime of hydrogen of water and hydroxyl group of methanol

(Figure 5-19 (B)), (B) overlapped regime of hydrogen that is bonded to carbon of methanol and H_e (Figure 5-15 (B)), (C) regime of H_g (Figure 5-15 (B)) as the reference for the integration.

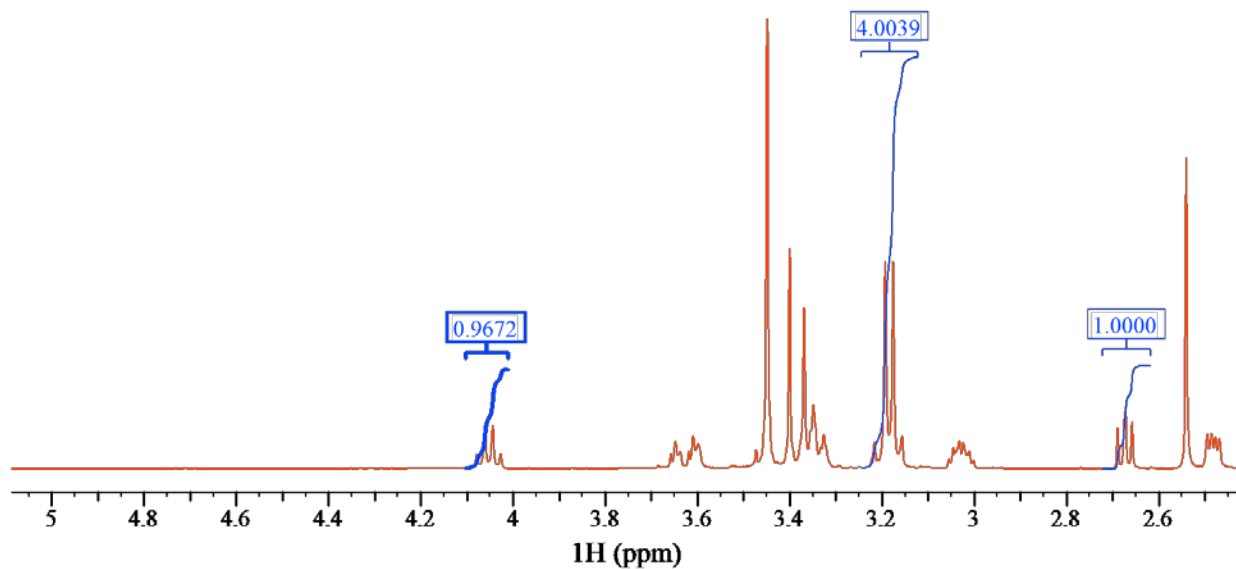


Figure 5-21. ¹H-NMR spectra of 0.005N HNO₃ and GPTMS at molar ratio of 1:1 with partial integration of block A, B and C from left to right.

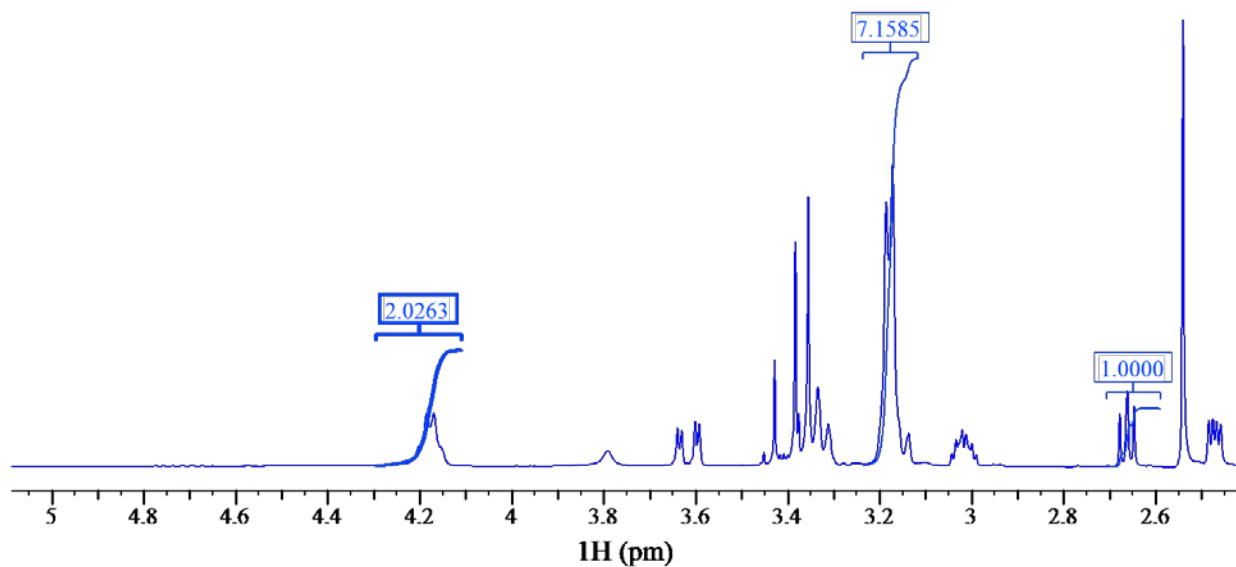


Figure 5-22. ¹H-NMR spectra of 0.005N HNO₃ and GPTMS at molar ratio of 2:1 with partial integration of block A, B and C from left to right.

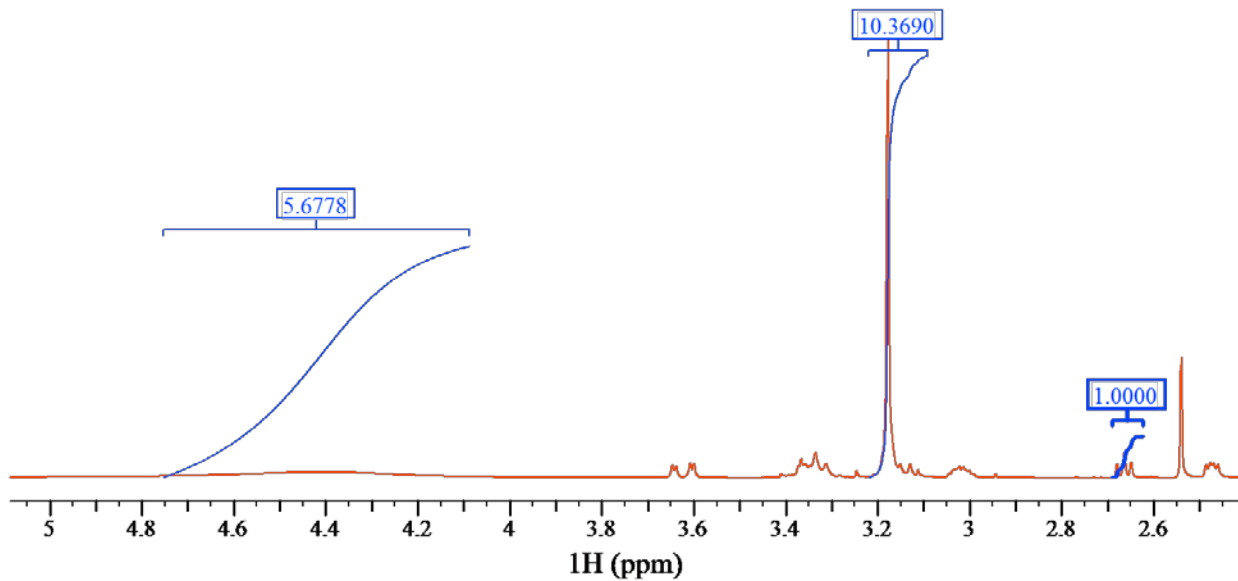


Figure 5-23. ^1H -NMR spectra of 0.005N HNO_3 and GPTMS at molar ratio of 4:1 with partial integration of block A, B and C from left to right.

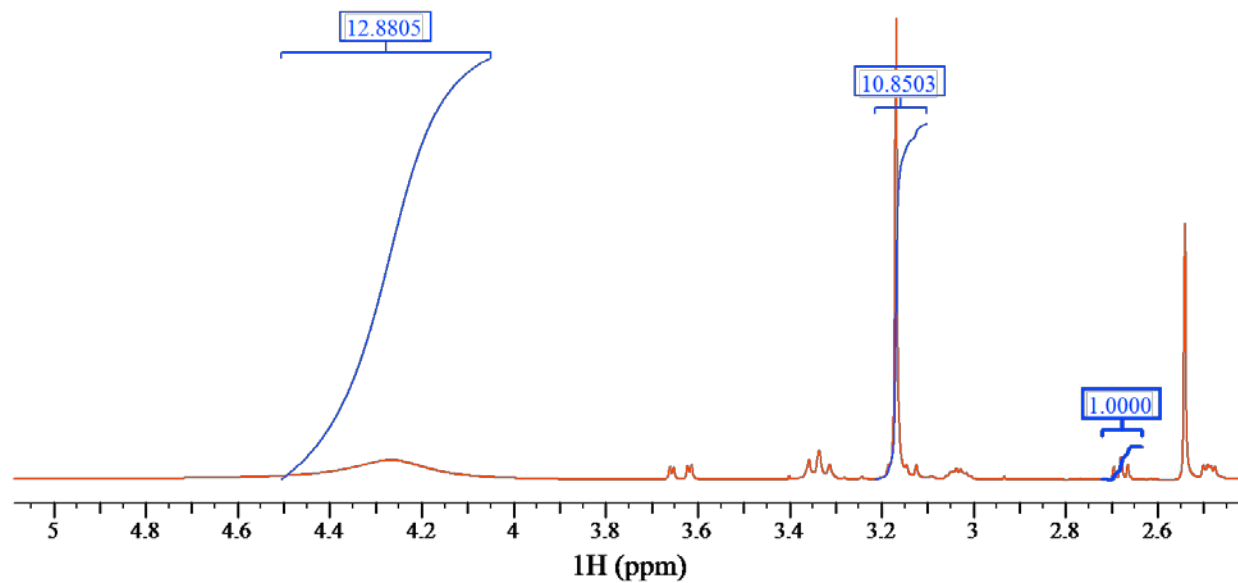


Figure 5-24. ^1H -NMR spectra of 0.005N HNO_3 and GPTMS at molar ratio of 8:1 with partial integration of block A, B and C from left to right.

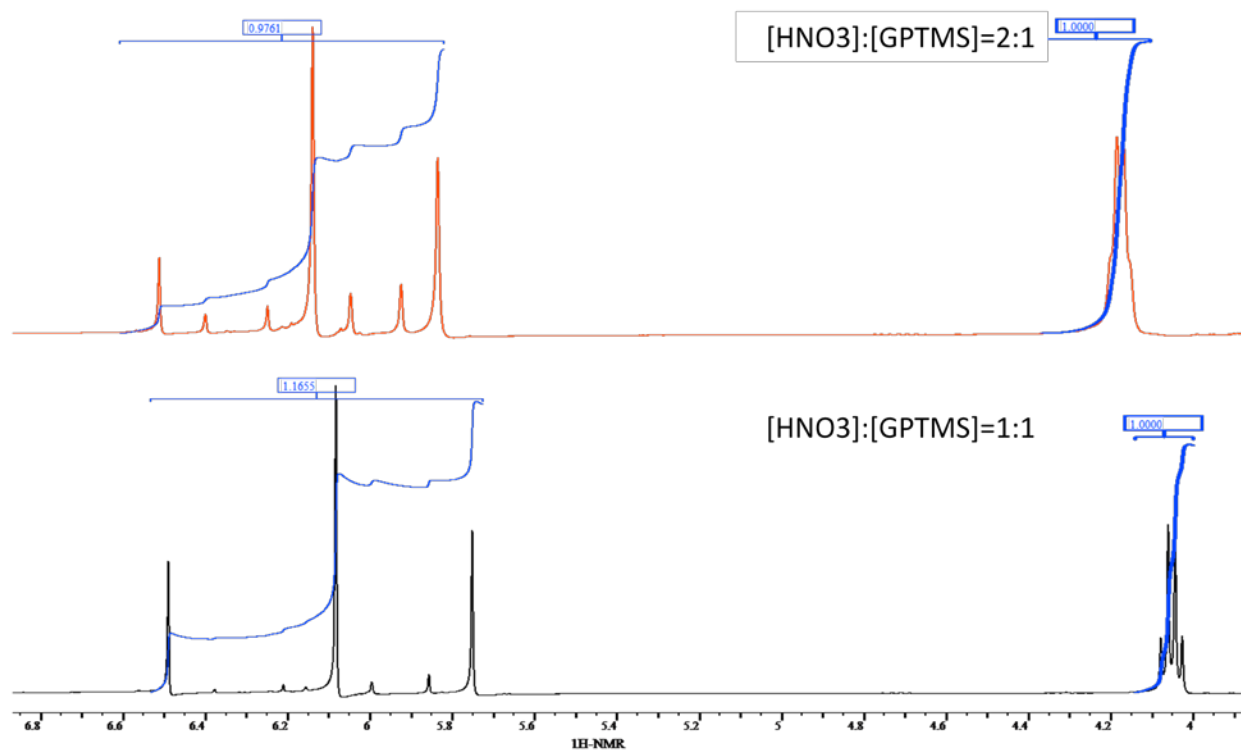


Figure 5-25. Enlarged ^1H -NMR spectra of Figure 5-19 (A).

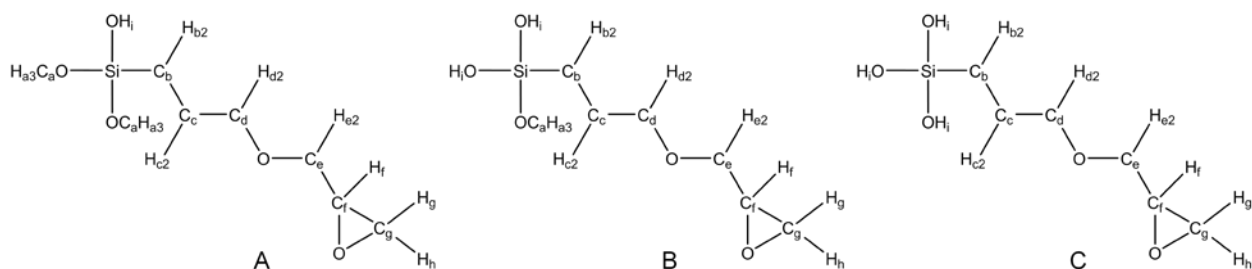


Figure 5-26. Transition state of GPTMS in the proposed hydrolysis reaction (Figure 5-17). (A) One methoxy group is hydrolyzed, (B) two methoxy groups are hydrolyzed and, (C) fully hydrolyzed GPTMS.

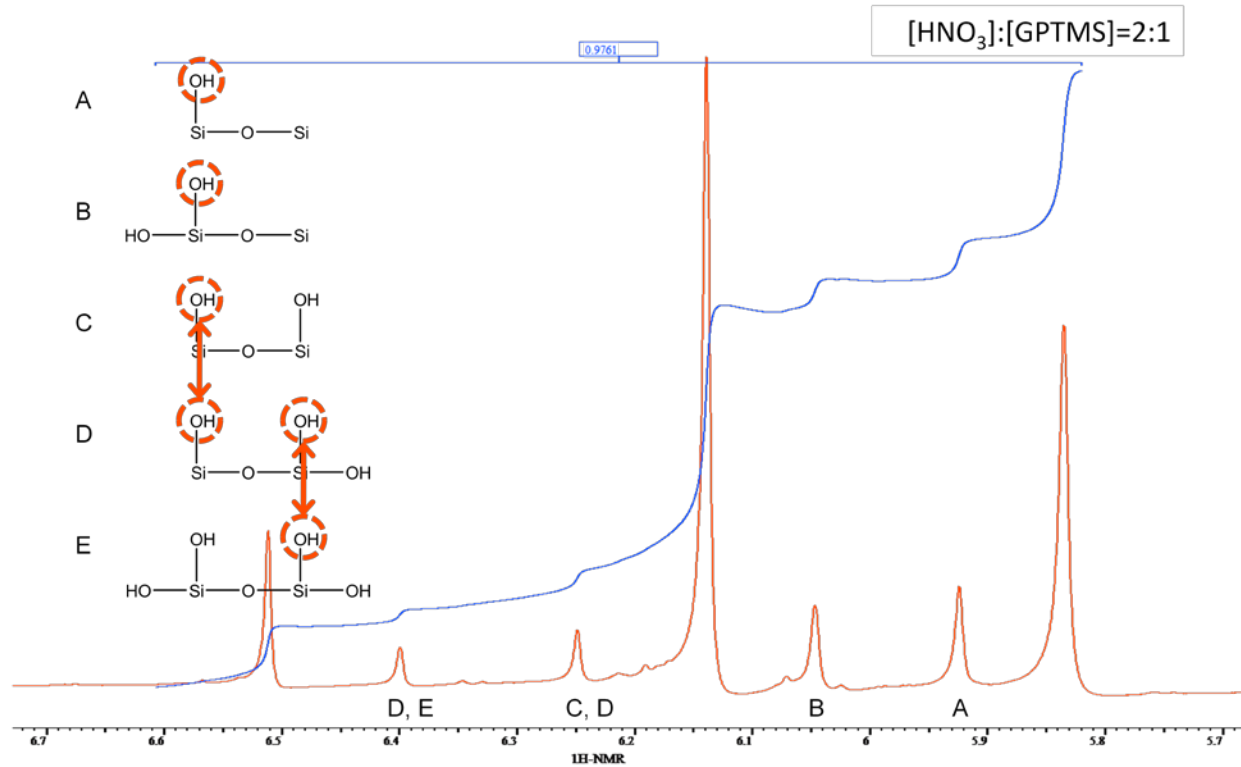


Figure 5-27. Enlarged ¹H-NMR spectrum of 0.005N HNO₃ and GPTMS at molar ratio of 2:1 in Figure 5-19 (A).

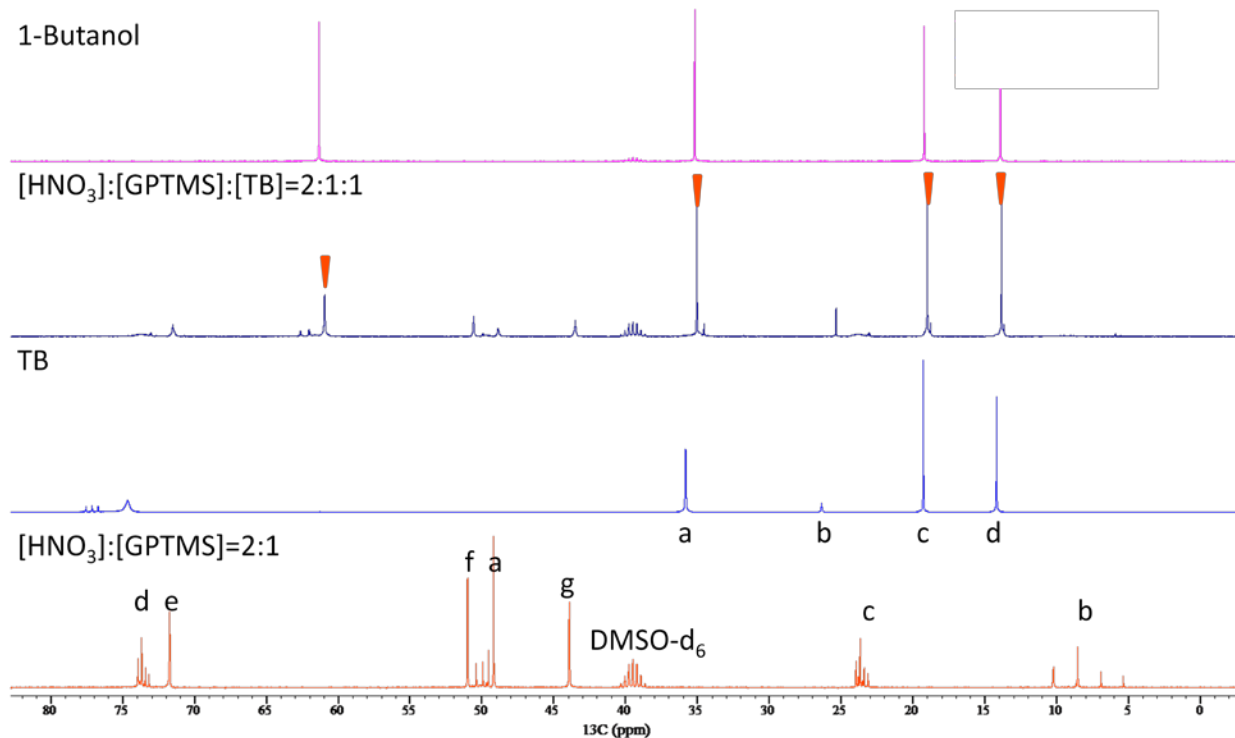


Figure 5-28. ^{13}C -NMR spectra of (from bottom to top) $[0.005\text{N HNO}_3]:[\text{GPTMS}]=2:1$, TB, $[0.005\text{N HNO}_3]:[\text{GPTMS}]:[\text{TB}]=2:1:1$ and 1-butanol. The wedges indicate the peaks of 1-butanol. Notations in peak assignment for TB and $[0.005\text{N HNO}_3]:[\text{GPTMS}]=2:1$ are based on Figure 5-29 and Figure 5-15 (A), respectively.

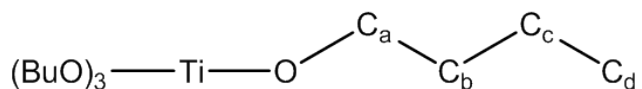


Figure 5-29. Chemical structure of TB. Chemically different carbon atoms are noted by different alphabet subscripts.

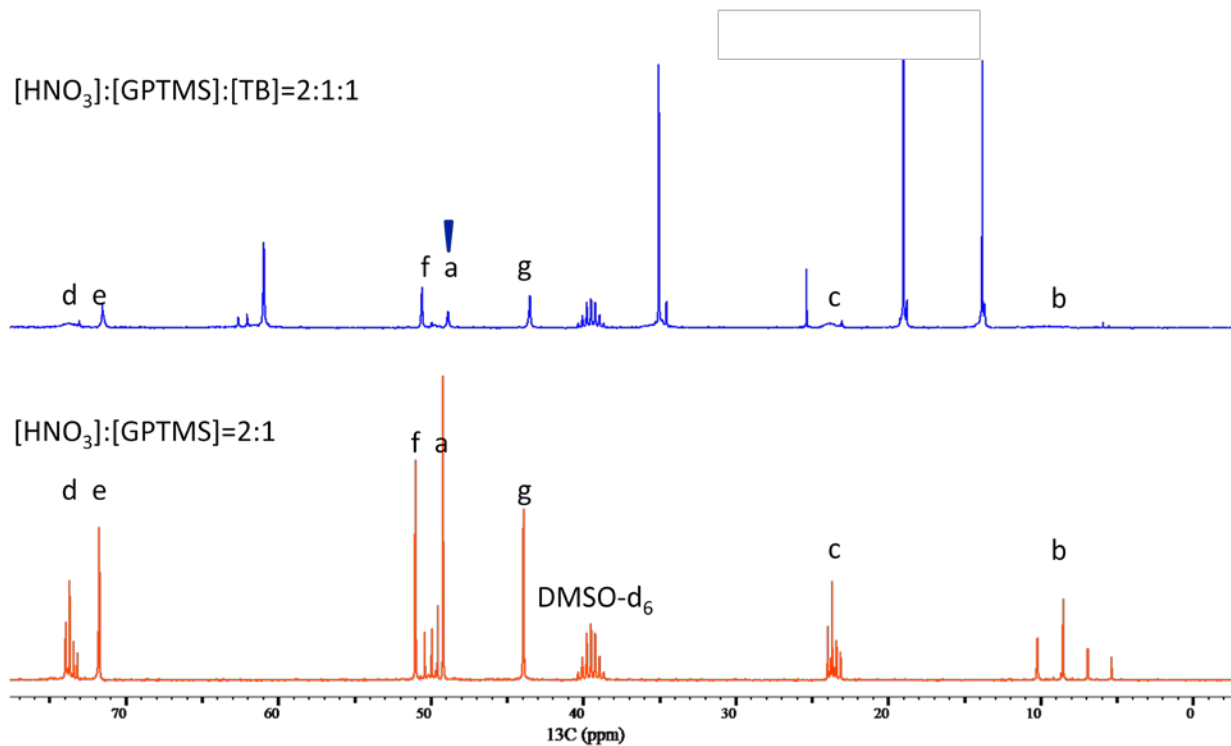


Figure 5-31. ^{13}C -NMR spectra of (from bottom to top) $[0.005\text{N HNO}_3]:[\text{GPTMS}]=2:1$ and $[0.005\text{N HNO}_3]:[\text{GPTMS}]:[\text{TB}]=2:1:1$. The wedge indicates the peak of methanol.

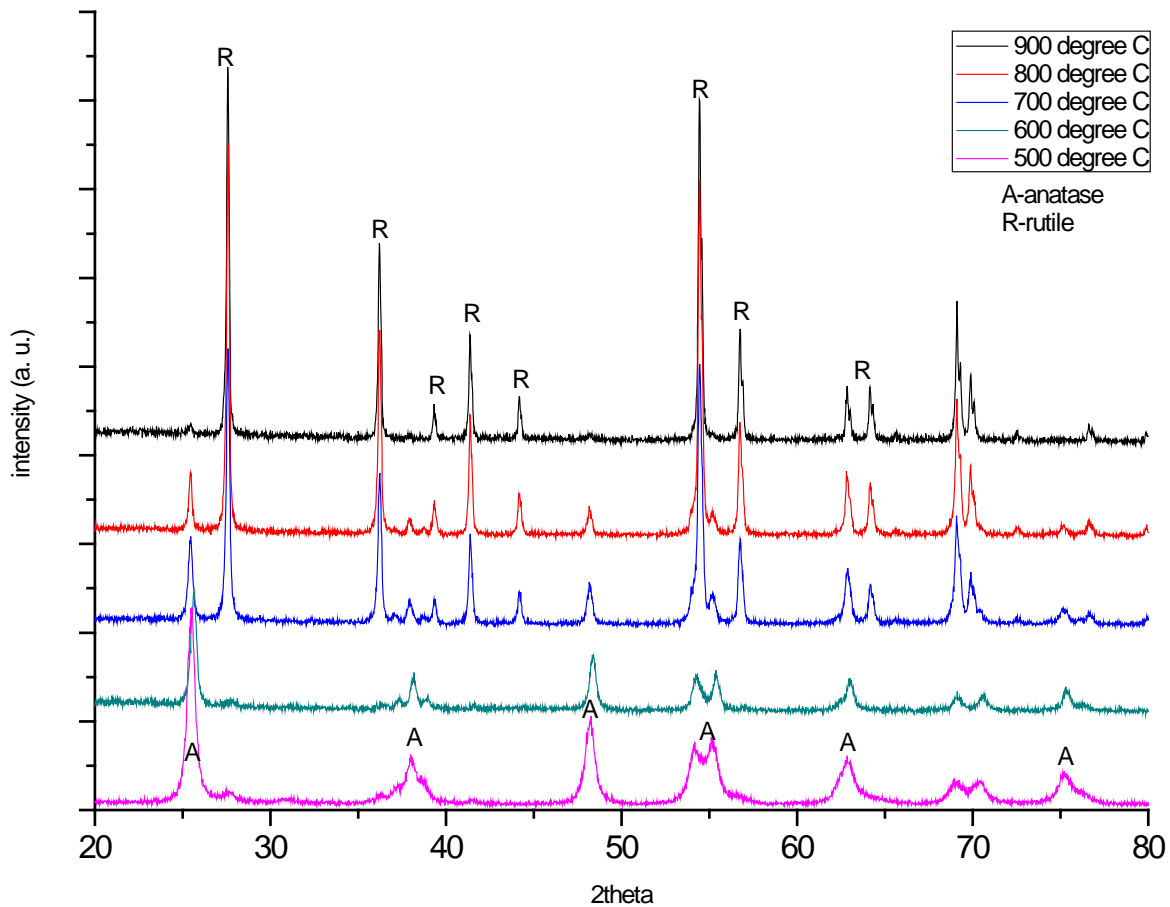


Figure 5-32. X-ray diffraction pattern of electrospun TiO₂ fibers heat-treated at various temperatures for 3 hours. Peaks notated as A and R indicate anatase and rutile phase, respectively.

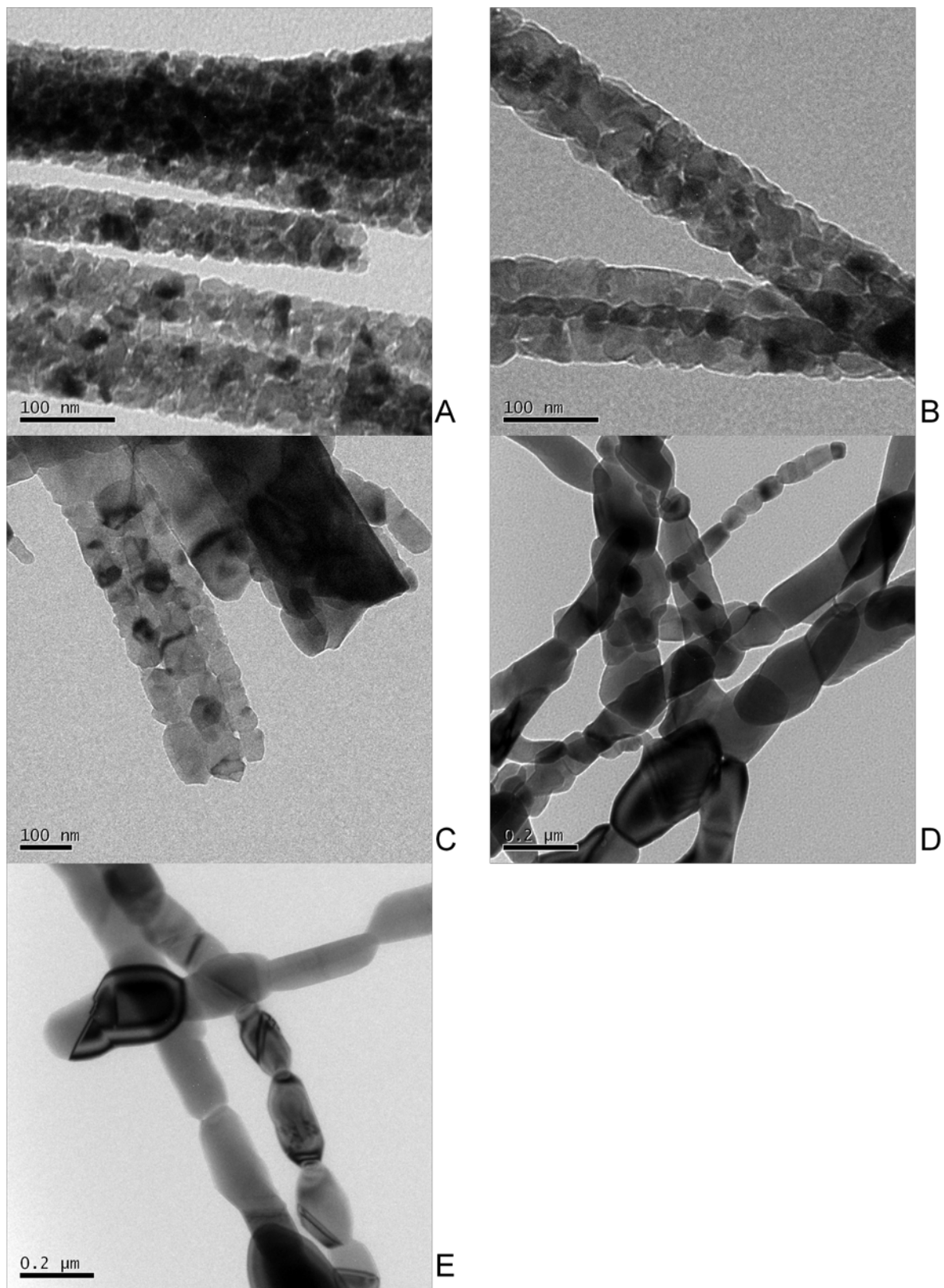


Figure 5-33. TEM images of electrospun TiO₂ fibers heat-treated at (A) 500°C, (B) 600°C, (C) 700°C, (D) 800°C, and (E) 900°C for 3 hours.

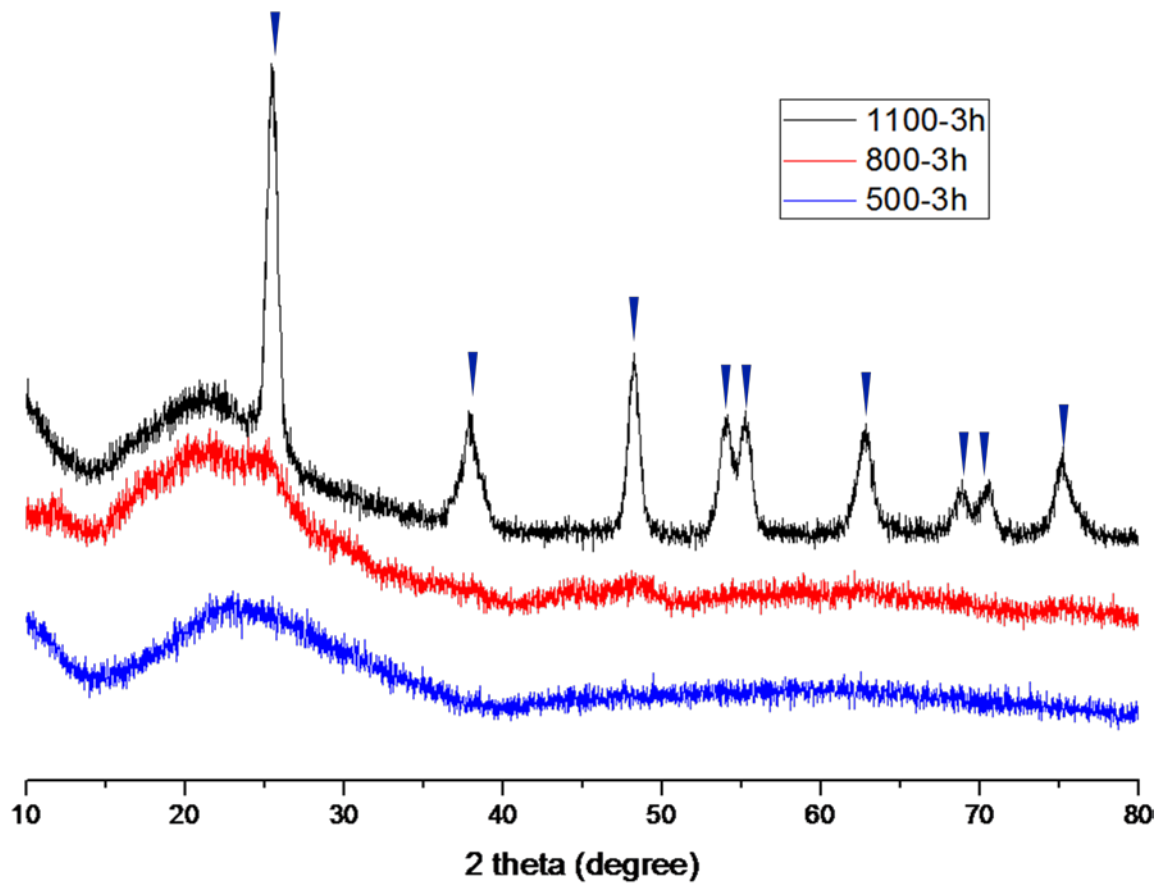


Figure 5-34. X-ray diffraction pattern of electrospun $\text{TiO}_2\text{-SiO}_2$ composite fibers heat-treated at various temperatures. Peaks marked with wedges indicate anatase phase of TiO_2 .

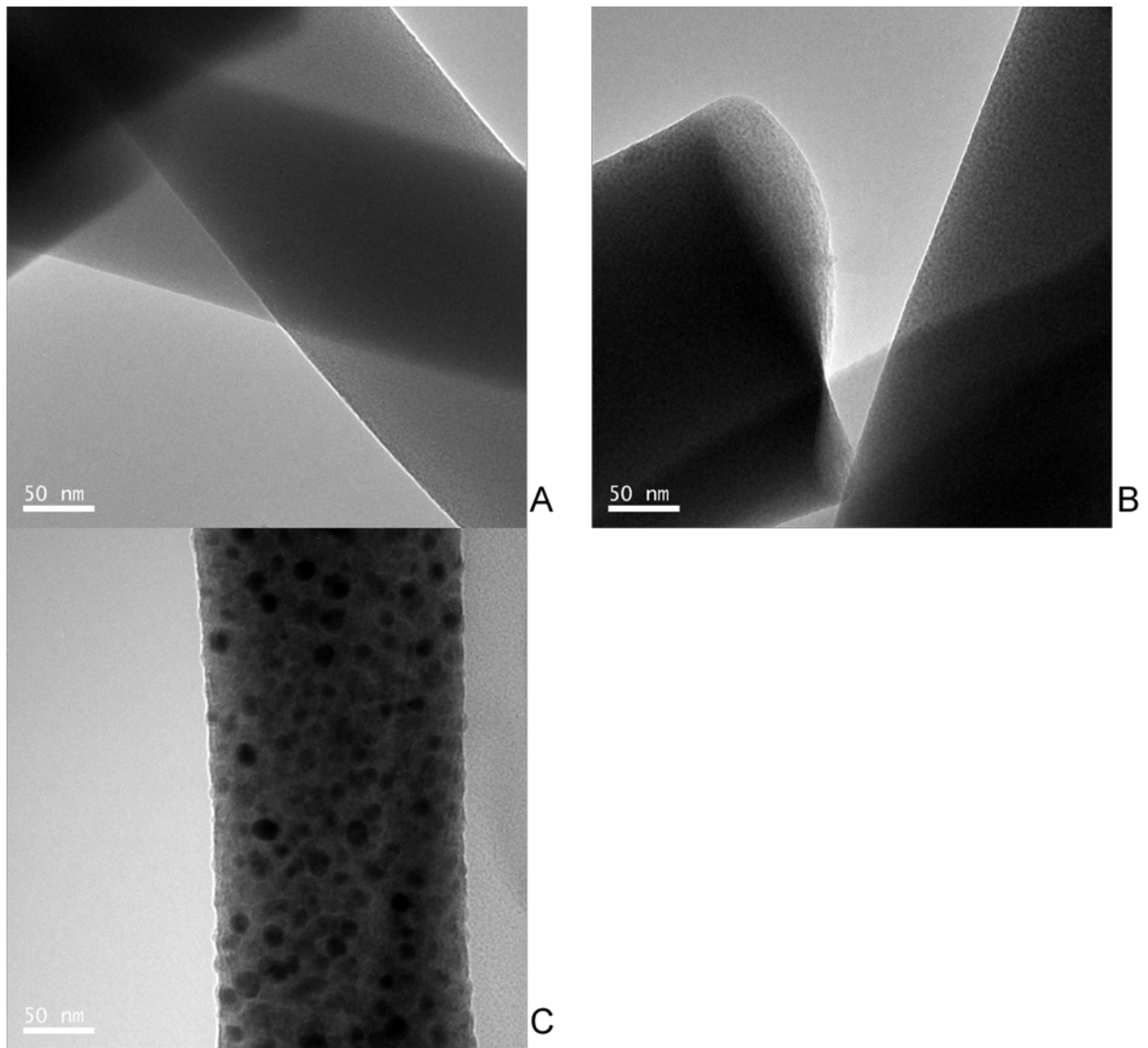


Figure 5-35. TEM images of electrospun TiO_2 – SiO_2 composite fibers from aqueous sol heat-treated at (A) 500°C, (B) 800°C, and (C) 1100°C for 3 hours.

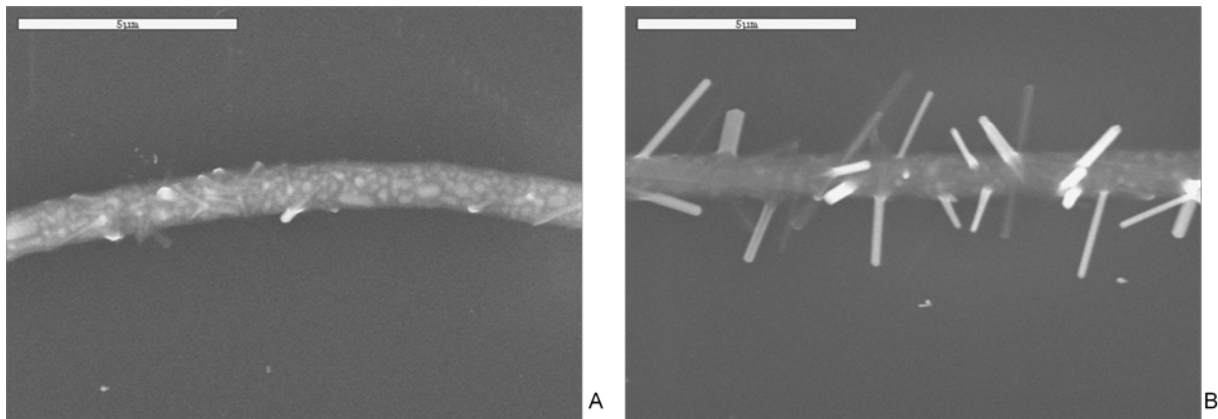


Figure 5-36. SEM images of 1100°C-heat-treated electrospun $\text{TiO}_2\text{-SiO}_2$ fibers from sol A. $[\text{TiO}_2]:[\text{SiO}_2]=1:1$. Images are from same batch of sample that show different morphologies, i.e. (A) rough surfaces of fiber and (B) spikes from the fiber.

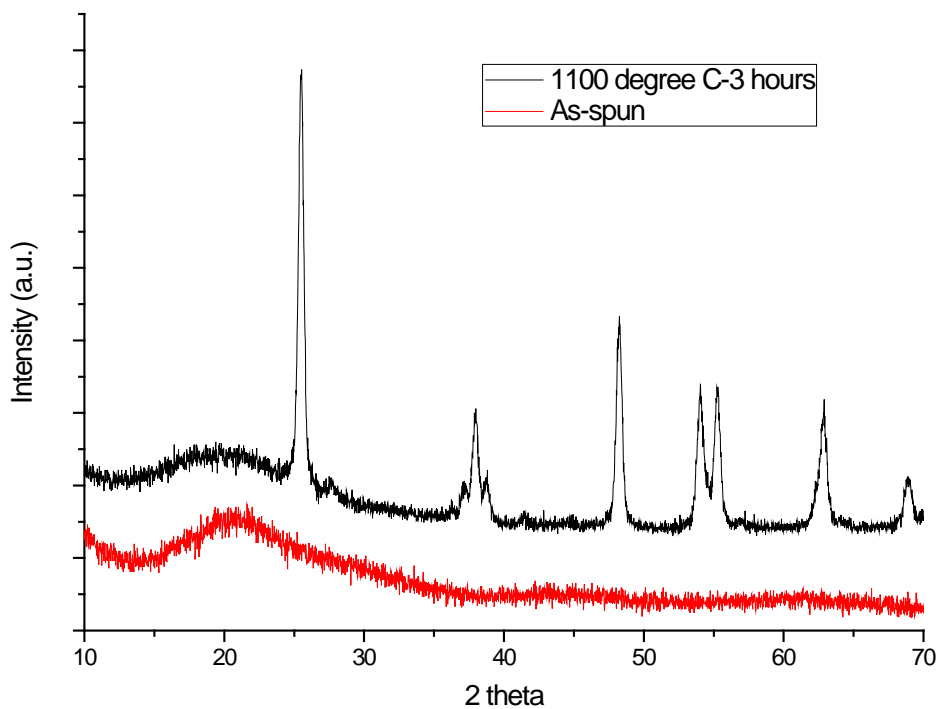


Figure 5-37. XRD result of electrospun $\text{TiO}_2\text{-SiO}_2$ composite fibers before and after heat treatment at 1100°C for 3 hours.

CHAPTER 6 CONCLUSIONS AND FUTURE WORK

Conclusions

In the filtration test, it was presented that filtration media comprising of thinner fibers have a higher quality factor (q_F), expressed as equation 1-1, than the microfiber-based high-efficiency particulate air (HEPA) filters. The mean fiber diameter (d_f) of electrospun polyacrylonitrile (PAN) fibers was 224 nm. The q_F of PAN 3x5 was 0.067 ± 0 while the HEPA filter that is adopted and currently used by the U.S. Army has a q_F of 0.031 ± 0.001 , the military standard being established at 0.020. When 3 layers of 5-minute-deposited PAN fibermats (PAN 5) were used to improve the uniformity of fiber deposition, the q_F was amplified by 69% from that of a single layer of PAN 5.

In the electrospinning process, the mean fiber diameter (d_f) of anatase TiO_2 was increased from 149 nm to 1110 nm by increasing the polyvinylpyrrolidone (PVP) concentration from 4% to 16% weight per volume (w/v, g/ml) in ethanol after heat treatment to remove of PVP and for crystallization. TiO_2 - SiO_2 composite fibers were successfully electrospun from novel aqueous sol with the extended time taken before gelation or precipitation from 4 hours of ethanol-based TiO_2 sol to 4 months. Precipitation was determined when the sol got opaque based on the visual observation by every 10 minutes while gelation was defined when the sol didn't flow down in the glass vial located upside down. The NMR study on the reaction mechanisms in the sol provided a basis upon which to optimize the composition for a stable aqueous sol. Morphologic change by the electrospun TiO_2 - SiO_2 composite material was observed going from beads to smooth fibers with increasing PVP concentration. During heat treatment, the electrospun fiber shrank in diameter by 48% for the sol with PVP 1% w/v

sol due to thermal degradation of PVP and mass transport by amorphous SiO₂ to fill in the space left from the polymer burn-out. The d_f that was achieved for TiO₂-SiO₂ composite fibers with anatase phase of TiO₂ was 243 nm. Since the mean fiber diameter of TiO₂-SiO₂ composite fibers is thicker than that of PAN fibers used in the filtration tests by 8%, the TiO₂-SiO₂ composite fiber mat would have a lower filtration efficiency and higher pressure drop than that of PAN fiber mats. Based on the geometry, the drag force of the TiO₂-SiO₂ composite fiber was calculated to be 13% higher than for the PAN fiber tested. However, the composite fiber would have a higher quality factor than the LydAir HEPA filter which has a 221%-higher drag force due to having fibers with a mean fiber diameter of 527 nm. Since filtration is a complicated phenomenon, filtration theory involves many complex empirical factors and simplifying assumptions. As a consequence, parameters like collection efficiency and pressure drop are not calculated for the whole filtration system. Nonetheless, the tendency of their changes by fiber diameter is predictable.

From the NMR study, the hydrolysis and condensation reactions between 0.005N HNO₃, 3-glycidoxypropyltrimethoxysilane (GPTMS) and titanium (IV) n-butoxide (TB) for a component of the aqueous sol system were hypothesized. Methoxy groups of GPTMS are hydrolyzed by water molecules and hydroxyl group formed by hydrolysis reaction react with TB to form Si-O-Ti bond through a condensation reaction. Reaction paths are described in Figure 5-17 and Figure 5-30.

Through the 3 hours of heat treatment process on the TiO₂ fibers, the anatase phase was formed at 500°C while the pure rutile phase was developed at 700°C and became predominant at 900°C. Grains of both phases grew as the temperature of heat

treatment was increased. This is attributed to the higher mobility of atoms towards the formation of larger grains with smaller specific surface area—i.e. grain boundary. For $\text{TiO}_2\text{-SiO}_2$ composite fibers, the anatase phase was clearly observed after heat treatment at 1100°C while formation of TiO_2 grains dispersed in the fiber was observed at 800°C . Whether the anatase grains after heat treatment at 1100°C are well-distributed in the fiber or aggregated on the surface of the fiber hasn't been clarified by TEM observation. The higher temperature required for the formation of the anatase phase is explained by the formation of Si-O-Ti bonds during the condensation reaction which then retards the formation of Ti-O-Ti bonds at temperatures lower than 1100°C . Unlike the coarse structure of anatase TiO_2 fibers, the $\text{TiO}_2\text{-SiO}_2$ composite fibers exhibited dense structures of anatase TiO_2 crystallites surrounded by an amorphous SiO_2 matrix. Because the crystallization temperature of SiO_2 to α -quartz is at 1500°C , the SiO_2 maintains its non-crystallinity at 1100°C while the increased molecular mobility allows for it to diffuse and fill the space formed during the crystallization of TiO_2 . More active grain growth, i.e. larger grain size, needle-like crystallites rooted on the fiber, was observed in electrospun $\text{TiO}_2\text{-SiO}_2$ fibers from the use of aqueous sol A with an abundance of TiO_2 . The composite fibers from the aqueous sol A have TiO_2 molar concentrations of 50% while those fibers from full aqueous sol has a TiO_2 concentration of 29% by mole.

Future Work

With regard to the mechanical stability issue, the $\text{TiO}_2\text{-SiO}_2$ composite nanofiber mats were tested by handling the samples in the lab similarly to the mechanical conditions that a filter would be expected to sustain. Superior strength by the composite fibers compared to pure anatase TiO_2 nanofiber mats was observed. The fiber mats

could be handled with tweezers or hands by holding on to a small edge. They did not fracture when doing so. This is in stark contrast to the pure polycrystalline TiO_2 nanofiber mats. Those only sustained handling, without fracturing, if they were supported by other materials at all times. Further tests on the mechanical properties—e.g. elastic modulus, toughness—of either single fiber or fibermats are desired to be done in the future (Figure 6-1).

Fiber mat comprising of TiO_2 - SiO_2 composite nanofibers is anticipated to fulfill the performance that the PAN fiber mat with 10%-thinner d_f showed as filtration media. However, in contrast to the polymeric fibers, TiO_2 -based fibers don't have smooth surfaces upon crystallization. They have cleavages, spikes, and pores depending on the composition and the heat treatment. The drag force and filtration efficiency by the filtration media with these rough microstructures cannot be the same as those by filtration media with smooth surfaces. It is a good material to conduct research on to determine how different microstructures affect filtration behavior.

With respect to the fibers, increasing the electrical conductivity and decreasing the surface tension of the electrospinning solution have not been tried yet, but these changes are expected to further reduce the fiber diameter of the TiO_2 - SiO_2 composite fibers either from full aqueous sol or sol A. For sol A, sols with lower and higher molar ratio of TB or lower PVP concentration were electrospun while fibers with mean fiber diameter less than $1 \mu\text{m}$ were not obtained from any of them. By adding additives like electrolytes and surfactants, a further decrease in fiber diameters is theoretically possible.

In regards to the chemistry in the aqueous sol, the reaction paths in sol B and the full sol, which is the mixture of sol A and B, were not discussed here due to the limitations of resources. This topic is of great interest for further research because of the unique stabilization of the metal alkoxide in conditions with an abundance of water.

Aging of aqueous sol is another subject to explore as well due to its surprisingly elongated shelf-life when in contact with an abundance of water molecules. Results from observation on aqueous sols with varying metal alkoxides and their molar ratios are listed in Table 5-7. Since the samples were not watched through for 24 hours, the shelf-life in Table 5-7 has an error of 1 or 2 hours. Moreover, the point of gelation was ambiguous because it is practically impossible to run the rheometer to measure the change of viscosity of the sample in-situ for, sometimes, over a few months. However, despite the result being from a limited number of metal alkoxides and molar ratios, clear tendencies for longer shelf-life was observed with optimized molar ratio for each metal alkoxide. Discerning the aging mechanism would be of great interest and would provide clues to improve the stability of sols containing metal alkoxide in other organic system. The chemical mechanisms of full aqueous sol could be understood in parallel as well.

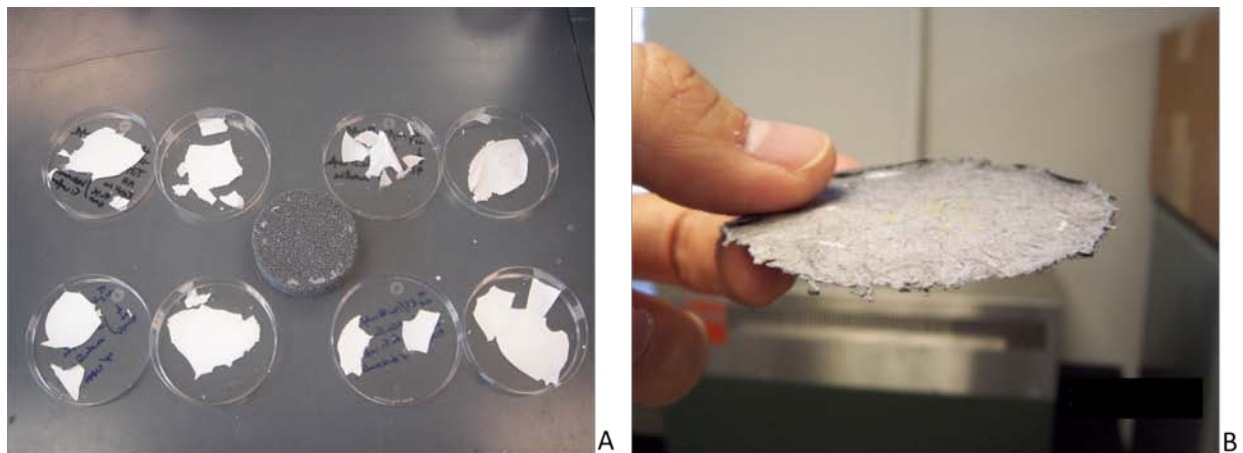


Figure 6-1. (A) Fractured anatase TiO_2 fibermats composed of fibers of $d_f=149$ nm, (B) A $\text{TiO}_2\text{-SiO}_2$ composite fibermat composed of fibers of $d_f=243$ nm from full aqueous sol after heat treatment.

LIST OF REFERENCES

1. Care, A. A. f. R. Lung Health Statistics by State. <http://www.aarc.org/> (March, 15, 2010).
2. Foundation, W. L. *Annual Report*; World Lung Foundation: New York, 2008.
3. United States. Environmental Protection Agency. Office of, R.; Development; National Center for Environmental, A. Integrated science assessment for particulate matter. <http://cfpub.epa.gov/ncea/cfm/recordisplay.cfm?deid=201805>
4. Brinker, C. J.; Scherer, G. W., *Sol-gel science : the physics and chemistry of sol-gel processing*. Academic Press: Boston, 1990; p xiv, 908.
5. Li, D.; Xia, Y. N., Fabrication of titania nanofibers by electrospinning. *Nano Letters* **2003**, 3, (4), 555-560.
6. Yang, X. G.; Shao, C. L.; Liu, Y. C.; Mu, R. X.; Guan, H. Y., Nanofibers of CeO₂ via an electrospinning technique. *Thin Solid Films* **2005**, 478, (1-2), 228-231.
7. Shao, C. L.; Guan, H. Y.; Liu, Y. C.; Gong, J.; Yu, N.; Yang, X. H., A novel method for making ZrO₂ nanofibres via an electrospinning technique. *Journal of Crystal Growth* **2004**, 267, (1-2), 380-384.
8. Larsen, G.; Velarde-Ortiz, R.; Minchow, K.; Barrero, A.; Loscertales, I. G., A method for making inorganic and hybrid (organic/inorganic) fibers and vesicles with diameters in the submicrometer and micrometer range via sol-gel chemistry and electrically forced liquid jets. *Journal of the American Chemical Society* **2003**, 125, (5), 1154-1155.
9. Sigmund, W.; Yuh, J.; Park, H.; Maneeratana, V.; Pyrgiotakis, G.; Daga, A.; Taylor, J.; Nino, J. C., Processing and structure relationships in electrospinning of ceramic fiber systems. *Journal of the American Ceramic Society* **2006**, 89, (2), 395-407.
10. Hinds, W. C., *Aerosol technology : properties, behavior, and measurement of airborne particles*. 2nd ed.; Wiley: New York, 1999; p xx, 483.
11. Allen, M. D.; Raabe, O. G., Slip Correction Measurements of Spherical Solid Aerosol-Particles in an Improved Millikan Apparatus. *Aerosol Science and Technology* **1985**, 4, (3), 269-286.
12. Allen, M. D.; Raabe, O. G., Re-evaluation of Millikan Oil Drop Data for the Motion of Small Particles in Air. *Journal of Aerosol Science* **1982**, 13, (6), 537-547.
13. Lee, K. W.; Ramamurthi, M., Filter Collection. In *Aerosol Measurement: Principles, Techniques, and Applications* Willeke, K.; Baron, P. A., Eds. Van Nostrand Reinhold: New York, 1993; p 179.

14. Yeh, H.-C.; Liu, B. Y. H., Aerosol filtration by fibrous filters--I. theoretical. *Journal of Aerosol Science* **1974**, 5, (2), 191-204.
15. Kirsch, A. A.; Fuchs, N. A., Studies on fibrous aerosol filters. 3. Diffusional deposition of aerosols in fibrous filters. *Ann Occup Hyg* **1968**, 11, (4), 299-304.
16. Wang, J.; Kim, S. C.; Pui, D. Y., Investigation of the figure of merit for filters with a single nanofiber layer on a substrate. *Journal of Aerosol Science* **2008**, 39, (4), 323-334.
17. Darcy, H., *Les Fontaines Publiques de la Ville de Dijon*. Dalmont: Paris, 1856.
18. Livage, J.; Henry, M.; Sanchez, C., Sol-gel Chemistry of Transition-metal Oxides. *Progress in Solid State Chemistry* **1988**, 18, (4), 259-341.
19. Taylor, G., Disintegration of Water Drops in Electric Field. *Proceedings of the Royal Society of London Series a-Mathematical and Physical Sciences* **1964**, 280, (1380), 383-+.
20. Fridrikh, S. V.; Yu, J. H.; Brenner, M. P.; Rutledge, G. C., Controlling the Fiber Diameter during Electrospinning. *Physical Review Letters* **2003**, 90, (14), 144502.
21. Hohman, M. M.; Shin, M.; Rutledge, G.; Brenner, M. P., Electrospinning and electrically forced jets. I. Stability theory. *Physics of Fluids* **2001**, 13, (8), 2201-2220.
22. Hohman, M. M.; Shin, M.; Rutledge, G.; Brenner, M. P., Electrospinning and electrically forced jets. II. Applications. *Physics of Fluids* **2001**, 13, (8), 2221-2236.
23. He, J. H.; Wan, Y. Q.; Yu, J. Y., Effect of concentration on electrospun polyacrylonitrile (PAN) nanofibers. *Fiber. Polym.* **2008**, 9, (2), 140-142.
24. Jarusuwannapoom, T.; Hongroijanawiwat, W.; Jitjaicham, S.; Wannatong, L.; Nithitanakul, M.; Pattamaprom, C.; Koombhongse, P.; Rangkupan, R.; Supaphol, P., Effect of solvents on electro-spinnability of polystyrene solutions and morphological appearance of resulting electrospun polystyrene fibers. *European Polymer Journal* **2005**, 41, (3), 409-421.
25. Skotak, M.; Larsen, G., Solution chemistry control to make well defined submicron continuous fibres by electrospinning: the (CH₃CH₂CH₂O)₄Ti/AcOH/poly(N-vinylpyrrolidone) system. *Journal of Materials Chemistry* **2006**, 16, (29), 3031-3039.
26. Son, W. K.; Cho, D.; Park, W. H., Direct electrospinning of ultrafine titania fibres in the absence of polymer additives and formation of pure anatase titania fibres at low temperature. *Nanotechnology* **2006**, 17, (2), 439-443.

27. Thompson, C. J.; Chase, G. G.; Yarin, A. L.; Reneker, D. H., Effects of parameters on nanofiber diameter determined from electrospinning model. *Polymer* **2007**, 48, (23), 6913-6922.
28. Burger, C.; Hsiao, B. S.; Chu, B., Nanofibrous materials and their applications. *Annual Review of Materials Research* **2006**, 36, 333-368.
29. Chen, H.-C.; Jao, W.-C.; Yang, M.-C., Characterization of gelatin nanofibers electrospun using ethanol/formic acid/water as a solvent. *Polymers for Advanced Technologies* **2009**, 20, (2), 98-103.
30. Cengiz, F.; Krucinska, I.; Gliscinska, E.; Chrzanowski, M.; Goktepe, F., Comparative Analysis of Various Electrospinning Methods of Nanofibre Formation. *Fibres & Textiles in Eastern Europe* **2009**, 17, (1), 13-19.
31. Tsai, P. P.; Chen, W.; Roth, J. R., Investigation of the Fiber, Bulk, and Surface Properties of Meltblown and Electrospun Polymeric Fabrics. *International Nonwovens Journal* **2004**, 13, (3), 17-23.
32. David, L. I. B.; Ismail, A. F., Influence of the thermastabilization process and soak time during pyrolysis process on the polyacrylonitrile carbon membranes for O-2/N-2 separation. *Journal of Membrane Science* **2003**, 213, (1-2), 285-291.
33. Fitzer, E.; Frohs, W.; Heine, M., Optimization of Stabilization and Carbonization Treatment of Pan Fibers and Structural Characterization of the Resulting Carbon-Fibers. *Carbon* **1986**, 24, (4), 387-395.
34. Hou, H. Q.; Ge, J. J.; Zeng, J.; Li, Q.; Reneker, D. H.; Greiner, A.; Cheng, S. Z. D., Electrospun polyacrylonitrile nanofibers containing a high concentration of well-aligned multiwall carbon nanotubes. *Chemistry of Materials* **2005**, 17, (5), 967-973.
35. Zhang, W. X.; Liu, J.; Wu, G., Evolution of structure and properties of PAN precursors during their conversion to carbon fibers. *Carbon* **2003**, 41, (14), 2805-2812.
36. Zhang, Q.; Welch, J.; Park, H.; Wu, C.-Y.; Sigmund, W.; Marijnissen, J. C. M., Improvement in nanofiber filtration by multiple thin layers of nanofiber mats. *Journal of Aerosol Science* In Press, Corrected Proof.
37. Muscat, J.; Swamy, V.; Harrison, N. M., First-principles calculations of the phase stability of TiO₂. *Physical Review B* **2002**, 65, (22), -.
38. Arashi, H., Raman-Spectroscopic Study of the Pressure-Induced Phase-Transition in TiO₂. *J Phys Chem Solids* **1992**, 53, (3), 355-359.
39. Mammone, J. F.; Nicol, M.; Sharma, S. K., Raman-Spectra of TiO₂-I₁, TiO₂-I₂, SnO₂, and GeO₂ at High-Pressure. *J Phys Chem Solids* **1981**, 42, (5), 379-384.

40. Mammone, J. F.; Sharma, S. K.; Nicol, M., Raman-Study of Rutile (TiO₂) at High-Pressures. *Solid State Communications* **1980**, 34, (10), 799-802.
41. Dervos, C. T.; Thirios; Novacovich, J.; Vassiliou, P.; Skafidas, P., Permittivity properties of thermally treated TiO₂. *Materials Letters* **2004**, 58, (9), 1502-1507.
42. Woan, K.; Pyrgiotakis, G.; Sigmund, W., Photocatalytic Carbon-Nanotube-TiO₂ Composites. *Advanced Materials* **2009**, 21, (21), 2233-2239.
43. Pyrgiotakis, G. Titania carbon nanotube composites for enhanced photocatalysis. <http://purl.fcla.edu/fcla/etd/UFE0013482>
44. Olofinjana, A. O.; Bell, J. M.; Jämting, A. K., Evaluation of the mechanical properties of sol-gel-deposited titania films using ultra-micro-indentation method. *Wear* **2000**, 241, (2), 174-179.
45. Soares, P.; Mikowski, A.; Lepienski, C. M.; Santos, E.; Soares, G. A.; Swinka, V.; Kuromoto, N. K., Hardness and elastic modulus of TiO₂ anodic films measured by instrumented indentation. *Journal of Biomedical Materials Research Part B-Applied Biomaterials* **2008**, 84B, (2), 524-530.
46. Cromer, D. T.; Herrington, K., The Structures of Anatase and Rutile. *Journal of the American Chemical Society* **1955**, 77, (18), 4708-4709.
47. Avci, N.; Smet, P. F.; Poelman, H.; Van de Velde, N.; De Buysser, K.; Van Driessche, I.; Poelman, D., Characterization of TiO₂ powders and thin films prepared by non-aqueous sol-gel techniques. *Journal of Sol-Gel Science and Technology* **2009**, 52, (3), 424-431.
48. Madhugiri, S.; Sun, B.; Smirniotis, P. G.; Ferraris, J. P.; Balkus, K. J., Electrospun mesoporous titanium dioxide fibers. *Microporous and Mesoporous Materials* **2004**, 69, (1-2), 77-83.
49. Nuansing, W.; Ninmuang, S.; Jarernboon, W.; Maensiri, S.; Seraphin, S., Structural characterization and morphology of electrospun TiO₂ nanofibers. *Materials Science and Engineering B-Solid State Materials for Advanced Technology* **2006**, 131, (1-3), 147-155.
50. Kanno, Y., Discussion from the Nucleation for the Crystallization Temperature of Vitreous Silica. *J. Mater. Sci. Lett.* **1990**, 9, (4), 451-453.
51. Defense, D. o., Filter Medium, Fire-Resistant, High-Efficiency. In *MIL-F-51079D*, U. S. Government Printing Office: 1998.
52. Günther, H., *NMR spectroscopy: basic principles, concepts, and applications in chemistry*. 2 ed.; John Wiley & Sons Ltd.: New York, 1995; p 581.

53. Allen, S. M.; Thomas, E. L., *The Structure of Materials*. 1st edition ed.; John Wiley & Sons, Inc.: New York, 1999; p 472.
54. Breitmaier, E.; Voelter, W., *Carbon-13 NMR spectroscopy: high-resolution methods and applications in organic chemistry and biochemistry*. 3 ed.; VCH Publishers: New York, 1987; p 515.
55. Freeman, R., *A Handbook of Nuclear Magnetic Resonance*. 2 ed.; Addison Wesley Longman Ltd.: Harlow, UK, 1997; p 344.
56. Gottlieb, H. E.; Kotlyar, V.; Nudelman, A., NMR chemical shifts of common laboratory solvents as trace impurities. *Journal of Organic Chemistry* **1997**, 62, (21), 7512-7515.
57. Cullity, B. D.; Stock, S. R., *Elements of X-Ray Diffraction*. 3 ed.; Prentice-Hall, Inc.: Upper Saddle River, NJ, 2001.
58. Klug, H. P.; Alexander, L. E., *X-ray Diffraction Procedures* John Wiley & Sons: New York, 1974; p 966.
59. Yoon, K.; Kim, K.; Wang, X.; Fang, D.; Hsiao, B. S.; Chu, B., High flux ultrafiltration membranes based on electrospun nanofibrous PAN scaffolds and chitosan coating. *Polymer* **2006**, 47, (7), 2434-2441.
60. Chrissafis, K.; Paraskevopoulos, K. M.; Papageorgiou, G. Z.; Bikiaris, D. N., Thermal and dynamic mechanical behavior of bionanocomposites: Fumed silica nanoparticles dispersed in poly(vinyl pyrrolidone), chitosan, and poly(vinyl alcohol). *Journal of Applied Polymer Science* **2008**, 110, (3), 1739-1749.
61. Shibaev, L. A.; Melenevskaya, E. Y.; Ginzburg, B. M.; Yakimanskii, A. V.; Ratnikova, O. V.; Griбанov, A. V., Thermal and tribological properties of fullerene-containing composite systems. Part 3. Features of the mechanism of thermal degradation of poly-(N-vinyl-pyrrolidone) and its compositions with fullerene C-60. *J. Macromol. Sci. Part B-Phys.* **2008**, 47, (2), 276-287.
62. Lau, C.; Mi, Y., A study of blending and complexation of poly(acrylic acid)/poly(vinyl pyrrolidone). *Polymer* **2002**, 43, (3), 823-829.
63. Lee, D. Y., Titania nanofibers prepared by electrospinning. *Journal of the Korean Physical Society* **2006**, 48, (6), 1686-1690.
64. Nakamura, T.; Ichitsubo, T.; Matsubara, E.; Muramatsu, A.; Sato, N.; Takahashi, H., On the preferential formation of anatase in amorphous titanium oxide film. *Scripta Materialia* **2005**, 53, (9), 1019-1023.

65. Fong, H.; Chun, I.; Reneker, D. H., Beaded nanofibers formed during electrospinning. *Polymer* **1999**, 40, (16), 4585-4592.
66. Li, D.; Xia, Y. N., Electrospinning of nanofibers: Reinventing the wheel? *Advanced Materials* **2004**, 16, (14), 1151-1170.
67. Kumar, A.; Jose, R.; Fujihara, K.; Wang, J.; Ramakrishna, S., Structural and optical properties of electrospun TiO₂ nanofibers. *Chemistry of Materials* **2007**, 19, (26), 6536-6542.
68. Reed, J. S., *Principles of Ceramics Processing*. 2nd edition ed.; John Wiley & Sons, Inc.: New York, 1995.
69. Umeda, J.; Moriya, M.; Sakamoto, W.; Yogo, T., Synthesis of proton conductive inorganic-organic hybrid membranes from organoalkoxysilane and hydroxyalkylphosphonic acid. *Journal of Membrane Science* **2009**, 326, (2), 701-707.
70. Yoder, C. H.; Schaeffer, J. C. D., *Introduction to Multinuclear NMR*. The Benjamin/Cummings Publishing Company, Inc.: Menlo Park, CA, 1987; p 335.
71. Keeler, J., *Understanding NMR Spectroscopy*. John Wiley & Sons Ltd.: Chichester, West Sussex, UK, 2005; p 459.
72. Samantaray, S. K.; Parida, K. M., SO₄²⁻/TiO₂-SiO₂ mixed oxide catalyst: 2. Effect of the fluoride ion and calcination temperature on esterification of acetic acid. *Applied Catalysis A: General* **2001**, 211, (2), 175-187.
73. Schmidt, H. K., Organically modified silicates and ceramics as two-phasic systems: Synthesis and processing. *Journal of Sol-Gel Science and Technology* **1997**, 8, (1-3), 557-565.
74. Falaras, P.; Xagas, A. P., Roughness and fractality of nanostructured TiO₂ films prepared via sol-gel technique. *Journal of Materials Science* **2002**, 37, (18), 3855-3860.
75. Williams, D. B.; Carter, C. B., *Transmission electron microscopy 3. Imaging*. Plenum Pr.: New York [u.a., 1996.
76. Jiang, H. G.; Ruhle, M.; Lavernia, E. J., On the applicability of the x-ray diffraction line profile analysis in extracting grain size and microstrain in nanocrystalline materials. *Journal of Materials Research* **1999**, 14, (2), 549-559.
77. Mo, S.-D.; Ching, W. Y., Electronic and optical properties of three phases of titanium dioxide: Rutile, anatase, and brookite. *Physical Review B* **1995**, 51, (19), 13023.

78. Wu, Q.; Zhao, B. Y.; Fang, C.; Hu, K. A., An enhanced polarization mechanism for the metal cations modified amorphous TiO₂ based electrorheological materials. *European Physical Journal E* **2005**, 17, (1), 63-67.
79. Izutsu, H.; Nair, P. K.; Maeda, K.; Kiyozumi, Y.; Mizukami, F., Structure and properties of TiO₂---SiO₂ prepared by sol-gel method in the presence of tartaric acid. *Materials Research Bulletin* **1997**, 32, (9), 1303-1311.
80. Choi, S. S.; Lee, S. G.; Im, S. S.; Kim, S. H.; Joo, Y. L., Silica nanofibers from electrospinning/sol-gel process. *Journal of Materials Science Letters* **2003**, 22, (12), 891-893.
81. Lee, S. W.; Kim, Y. U.; Choi, S. S.; Park, T. Y.; Joo, Y. L.; Lee, S. G., Preparation of SiO₂/TiO₂ composite fibers by sol-gel reaction and electrospinning. *Materials Letters* **2007**, 61, (3), 889-893.
82. Ren, J.; Li, Z.; Liu, S. S.; Xing, Y. L.; Xie, K. C., Silica-titania mixed oxides: Si-O-Ti connectivity, coordination of titanium, and surface acidic properties. *Catal. Lett.* **2008**, 124, (3-4), 185-194.
83. Viswanath, R. N.; Ramasamy, S., Study of TiO₂ nanocrystallites in TiO₂---SiO₂ composites. *Colloids and Surfaces A: Physicochemical and Engineering Aspects* **1998**, 133, (1-2), 49-56.

BIOGRAPHICAL SKETCH

Hyoungjun Park has worked with Dr. Sigmund in the field of sol-gel chemistry, electrospinning and other ceramics processing methods since 2006 at University of Florida. He earned his Bachelor of Science degree in materials science and engineering at Seoul National University, South Korea.